T.R.
BOLU ABANT İZZET BAYSAL UNIVERSITY
INSTITUTE OF GRADUATE STUDIES
Department of Physics

UPGRADE AND PERFORMANCE STUDIES OF A CMOS PIXEL SENSOR FOR THE FUTURE CIRCULAR COLLIDERS

DOCTOR OF PHILOSOPHY

KAAN YÜKSEL OYULMAZ

ACADEMIC SUPERVISOR
PROF. DR. HALUK DENİZLİ
ACADEMIC CO-SUPERVISOR
DR. CARLOS ANTONIO SOLANS SANCHEZ

BOLU, JULY-2022

APPROVAL OF THE THESIS

UPGRADE AND PERFORMANCE STUDIES OF A CMOS PIXEL SENSOR FOR THE FUTURE CIRCULAR COLLIDERS submitted by **Kaan Yüksel OYULMAZ** and defended before the Examining Committe Members listed below in partial fulfillment of the requirements for the degree of **Doctor of Philosophy** in **Department of Physics, Institute of Graduate Studies of Bolu Abant Izzet Baysal University on 25/07/2022** by

Examining Committee Members	**Signature**
Supervisor Prof. Dr. Haluk DENİZLİ Bolu Abant Izzet Baysal University	
Member Prof. Dr. Serkant Ali ÇETİN İstinye University	
Member Prof. Dr. İlkay TÜRK ÇAKIR Giresun University	
Member Prof. Dr. Abdulkadir ŞENOL Bolu Abant Izzet Baysal University	
Member Assoc. Prof. Ali YILMAZ Bolu Abant Izzet Baysal University	

Prof. Dr. İbrahim KÜRTÜL

Director of Institute of Graduate Studies

ETHICAL DECLARATION

In this thesis dissertation that was properly prepared according to the Thesis Writing Rules of Bolu Abant İzzet Baysal University of the Institute of Graduates Studies, I hereby declare that;

- All data, information, and documents presented in the thesis were obtained in accordance with the academic and ethical rules,
- All data, documents, assessments, and results were presented in accordance with the scientific ethical and moral rules,
- All works that were benefitted in the thesis were appropriately cited,
- No alteration was made in the data used,
- Study presented in this thesis is original,

  Otherwise, I declare that I accept the loss of all my rights in case any contradiction that may arise against me.

Based on the plagiarism report that was generated on the date of 04/08/2022 by using predetermined filtrations set by Directorate of Institute of Graduate Studies of the Turnitin programme, a plagiarism detection sofware, the similarity index detected was 14%.

Kaan Yüksel OYULMAZ

ABSTRACT

UPGRADE AND PERFORMANCE STUDIES OF A CMOS PIXEL SENSOR FOR THE FUTURE CIRCULAR COLLIDERS
PHD THESIS
KAAN YÜKSEL OYULMAZ
BOLU ABANT IZZET BAYSAL UNIVERSITY
INSTITUTE OF GRADUATE STUDIES
DEPARTMENT OF PHYSICS
(SUPERVISOR: PROF. DR., HALUK DENIZLI)
(CO-SUPERVISOR: DR. CARLOS SOLANS SANCHEZ)
BOLU, JULY 2022
xix + 132

The Future Circular Collider (FCC-hh) is a new particle collider designed to provide proton-proton collisions with a center-of-mass energy of 100 TeV and an integrated luminosity of 30 ab^{-1} for 25 years of operation. With the center-of-mass energy it has, FCC-hh is aimed to not only test the Standard Model and Beyond Standart Model theories with high precision but also try to observe unknowns of the universe such as dark energy and dark matter. Therefore, the FCC-hh detector has to be capable of measuring the particles in the environment. However, when such large center-of-mass energy is reached, difficulties arise especially in terms of technology. The most important of these, the radiation levels around the beamline, is beyond today's technologies. Another major challenge at that energy for the detector and physics studies is a large number of proton-proton collisions that lead to an increase of simultaneous events per bunch crossing known as pile-up. The observation of rare physics events may be obstructed due to the high pile-up environment. These pile-up events can be determined by silicon pixel sensors which have a high granularity structure, good time resolution and radiation hardness. The MALTA sensor is a state-of-the-art radiation hard monolithic silicon pixel sensor with a small collection electrode produced by Tower Semiconductor for 180 nm CMOS imaging technology. The MALTA pixel sensor has been started to develop from experiences with ALPIDE sensor to be used in High Luminosity Large Hadron Collider (HL-LHC) upgrades of the inner tracker of the ATLAS experiment considering the demanding radiation levels and high pile-up environment of the detector. Thanks to its improvable structure, it is also considered a candidate pixel sensor for the inner tracker of the FCC-hh detector. In this thesis, details of the development process of the MALTA pixel sensors are discussed with respect to the laboratory and test beam results. After that, the time resolution performance of the MALTA sensor is tested with Higgs self-coupling ($gg \rightarrow HH \rightarrow b\bar{b}\gamma\gamma$) physics process study including realistic detector effects and pile-up environment of the FCC-hh detector within the DELPHES simulation. Consequently, the thesis is concluded with a discussion of the possible usage of the MALTA sensor in the FCC-hh detector based on its radiation performance and time resolution.

KEYWORDS: Future Circular Collider, CMOS Sensors, Radiation Hard Pixel Sensors, Monolithic Active Pixel Sensor, DELPHES, Pile-up Environment, Pile-up Mitigation, Higgs Self-coupling

ÖZET

GELECEK DAİRESEL ÇARPIŞTIRICILARI İÇİN CMOS PİKSEL SENSÖR GELİŞTİRME VE PERFORMANS ÇALIŞMALARI
DOKTORA TEZİ
KAAN YÜKSEL OYULMAZ
BOLU ABANT İZZET BAYSAL ÜNİVERSİTESİ
LİSANSÜSTÜ EĞİTİM ENSTİTÜSÜ
FİZİK ANABİLİM DALI
(TEZ DANIŞMANI: PROF. DR. HALUK DENİZLİ)
(İKİNCİ DANIŞMAN: DR. CARLOS ANTONIO SOLANS SANCHEZ)
BOLU, TEMMUZ - 2022
xix + 132

Gelecek Dairesel Çarpıştırıcısı (GDÇ-hh), 25 yıllık çalışma için 100 TeV kütle merkezi enerjisi ve 30 ab^{-1} parlaklık ile proton-proton çarpışmaları sağlamak üzere tasarlanmış yeni bir parçacık çarpıştırıcısıdır. GDÇ-hh sahip olduğu kütle merkezi enerjisi ile sadece Standart Model ve Standart Model Ötesi teorilerini yüksek hassasiyetle test etmeyi değil, aynı zamanda karanlık enerji ve karanlık madde gibi evrenin bilinmeyenlerini de gözlemlemeye çalışmayı amaçlamaktadır. Bu nedenle, GDÇ-hh dedektörü ortamdaki parçacıkları hassas bir şekilde tespit edebilmelidir. Ancak bu kadar büyük kütle merkezi enerjisine ulaşıldığında, özellikle teknoloji açısından zorluklar ortaya çıkmaktadır. Bunlardan en önemlisi, günümüz teknolojilerinin de üzerinde olan demet hattı etrafındaki radyasyon seviyeleridir. Dedektör ve fizik çalışmaları için bu enerjideki bir diğer önemli zorluk, yığıntı olarak bilinen demet geçişi başına eşzamanlı olayların artmasına yol açan çok sayıda proton-proton çarpışmasıdır. Nadir görülen fizik olaylarının gözlemlenmesi, yüksek yığma ortamı nedeniyle engellenebilir. Bu yığılma olayları, yüksek tanecikli yapıya, iyi zaman çözünürlüğüne ve radyasyon sertliğine sahip silikon piksel sensörleri tarafından belirlenebilir. MALTA sensörü, Tower Semiconductor tarafından 180 nm CMOS imgeleme teknolojisiyle üretilen küçük bir toplama elektrotuna sahip, son teknoloji radyasyona dayanıklı monolitik silikon piksel sensörüdür. MALTA piksel sensörü, ATLAS deneyinin iç izleyicisinin Yüksek Işınlılıklı Büyük Hadron Çarpıştırıcısı (YI-BHÇ) yükseltmeleri için ALPIDE sensöründen elde edilen deneyimlerden, dedektördeki zorlu radyasyon seviyeleri ve yüksek yığıntı ortamı dikkate alınarak geliştirilmeye başlanmıştır. Geliştirmeye açık yapısı sayesinde GDÇ-hh dedektörünün iç izleyicisi için de aday bir piksel sensörü olarak kabul edilir. Bu tezde, MALTA piksel sensörlerinin geliştirme sürecinin detayları, laboratuvar ve test ışını sonuçları paylaşılarak tartışılmaktadır. Sonrasında, MALTA sensörünün zaman çözünürlüğü performansı, DELPHES simülasyonu kullanılarak gerçekçi dedektör etkileri ve GDÇ-hh dedektörünün yığıntı ortamını içeren Higgs özbağlaşım fizik süreci ($gg \rightarrow HH \rightarrow b\bar{b}\gamma\gamma$) ile test edilmiştir. Sonuç olarak, tez, MALTA sensörünün radyasyon performansı ve zaman çözünürlüğüne dayalı olarak GDÇ-hh dedektöründe olası kullanımının tartışılmasıyla sonlandırılmıştır.

ANAHTAR KELİMELER: Gelecek Dairsel Çarpıştırıcısı, CMOS Sensör, Radyasyona Dayanıklı Piksel Sensörler, Monolitik Aktif Piksel Sensör, DELPHES, Yığıntı Ortamı, Yığıntı Azaltma, Higgs Özbağlaşımı

TABLE OF CONTENTS

LIST OF FIGURES

Page

LIST OF TABLES

Page

LIST OF ABBREVIATIONS AND SYMBOLS

ALICE	**:**	A Large Ion Collider Experiment
ATLAS	**:**	A Toroidal LHC ApparatuS
BSM	**:**	Beyond Standard Model
CERN	**:**	Conseil Européen pour la Recherche Nucléaire
CMOS	**:**	Complementary Metal Oxide Semiconductor
CMS	**:**	Compact Muon Solenoid
DA	**:**	Determinictic Annealing
DESY	**:**	Deutsches Elektronen-Synchrotron
FCC	**:**	Future Circular Collider
HL-LHC	**:**	High Limunosity Large Hadron Collider
LHC	**:**	Large Hadron Collider
LHCb	**:**	Large Hadron Collider Beauty Experiment
MALTA	**:**	Monolithic pixel detector from ALICE to ATLAS
MAPS	**:**	Monolithic Active Pixel Sensor
NIEL	**:**	Non-Ionizing Energy Loss
RTS	**:**	Random Telegraph Signal
SM	**:**	Standard Model
SPS	**:**	Super Proton Synchrotron
TCAD	**:**	Technology Computer-Aided Design
TID	**:**	Total Ionizing Dose

ACKNOWLEDGEMENTS

I wish to express my deepest gratitude to my supervisor Prof. Dr. Haluk Denizli and co-supervisor Dr. Carlos Solans Sanchez for their guidance, advice, criticism, encouragements and insight throughout the research.

I would also like to thank Dr. Michele Selvaggi for his suggestions and comments during the study.

I would also like to thank the members of the CERN MALTA group for accepting me among them and for their support during my study in the laboratory and test beam measurements.

I want to to thank my close friends Sinan Öztel, Doğan Avcı and Özgün Karadeniz, with whom I had the most enlightening and funny conversations during the university education.

I offer special thanks to Ümit Hasan Gözkonan for his friendship and support.

I would like to thank my best friends Ozan Kaan Sadıklar, Eren Erdemir and Gani Çağlar Çoban who have always supported and encouraged me since high school.

I am grateful to family for their support and patience from beginning to end.

Finally, I would like to express my sincere thanks to my fiancé, Gözde Çolak, for her love, trust and invaluable support throughout this exhausting process.

This thesis is dedicated to my dear father, the late Murat Oyulmaz, who always encouraged and supported me on the path I took.

1. INTRODUCTION

Mankind has asked questions about the unknowns of the universe and sought answers. Every answer they found caused them to ask more complex questions. In the final situation reached today, the question of why matter exists has begun to be asked. The answer to this still awaits today and many theories have been put forward to answer this question. Every substance we see around us is made of particles that come together. The Standard Model, which is one of the theories that describes the particles that make up matter and explains the interactions of these particles with each other, emerged in the middle of the 20th century and has taken its final form today after experimental observations. The model clarifies the fundamental particles discovered so far and their interaction with the three fundamental forces (weak, strong and electromagnetic interactions). It has been tested many times in the experiments, and these tests have precisely met with the predictions of the theory. The elementary particles that are defined by the Standard Model are shown in the Figure 1.1.

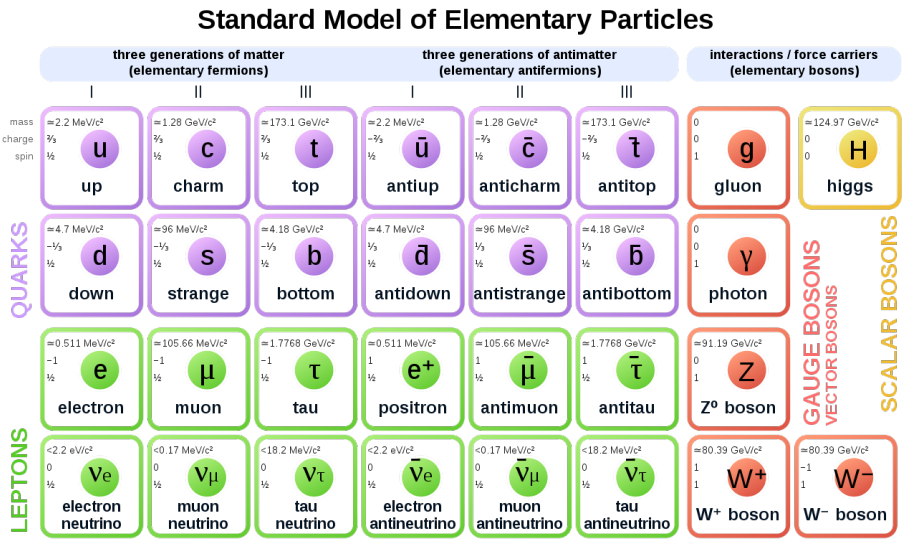

Figure 1.1. The elementary particles that are defined by the Standard Model. The figure is adopted from (1)

As can be seen in the Figure 1.1, the Standard Model divides particles into two groups as fermions and bosons. Fermions are elementary particles that obey the Pauli exclusion principle and have a spin value of 1/2. They are divided into two subgroups, leptons and quarks according to their interactions. While leptons interact

via electroweak interaction, quarks participate in strong and electroweak interactions. The other group bosons are divided into two as Gauge and scalar bosons. Gauge bosons are defined as force carriers that mediate strong, weak and electromagnetic fundamental interactions between particles and have a spin value of 1. The Higgs boson (2,3), a recently discovered scalar elementary particle with a spin value of 0, basically explains not only why fermions with mass in the model but also the photon has no mass. Additionally, it explains why the *Z* and *W* bosons have mass. However, its discovery was a challenging process. Scientists had been chasing the discovery of the Higgs boson for many years and experiments couldn't have found any clue that verifies the theory till the end of the '90s.

The European Organization for Nuclear Research (CERN) started to build the world's highest-energy hadron collider, the Large Hadron Collider (LHC), to discover the Higgs boson (2,3) and unveil the unknowns of high energy physics (4). It is a circular hadron collider with a circumference of 27 kilometers and located on the border of France and Switzerland (5). The collider accommodates different high energy physics experiments with own their distinctive detectors. Accelerated particles collide at four different points with 13 TeV center-of-mass collision energy and the detectors record collisions. In Figure 1.2, the layout of the LHC is shown and the four collision points are represented with blue stars. Whereas two of these interaction points, ATLAS (6) and CMS (7), are where the high luminosity experiments are done, the other two, ALICE (8) and LHCb (9), are the experiments for low luminosities of the LHC.

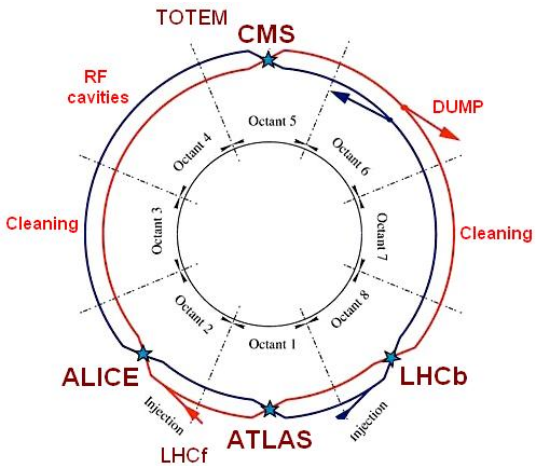

Figure 1.2. Schematic representation of the LHC layout (5).

In 2012, two high luminosity experiments of the LHC, ATLAS and CMS, made an announcement (10,11) of the discovery of Higgs boson in the mass region around 124.1 GeV at International Conference on High Energy Physics. This moment was another leap moment for humankind, denoting the big and powerful machines can be built for other problems of High Energy Physics theories such as super-symmetry and beyond Standard Model (BSM) theories/physics. As it can be seen, the big problems have demanding solutions and the LHC needs to be upgraded for other measurements and discoveries. Nowadays, it is in the upgrade process for High Luminosity LHC (HL-LHC) that will be started physics operation in 2028(12,13). However, one day it will become not enough for the physics society like its ancestors. Thanks to the visionary scientists, post-LHC accelerator studies have already started at CERN. The post-LHC accelerator study, which is known as Future Circular Collider (FCC), has been seen as a long-term goal by the European Strategy for Particle Physics (ESPP) (14). In 2013, ESPP has launched the FCC study as a worldwide international collaboration and the first conceptual design report (CDR) of FCC has been released in 2019 (15–17).

In this introductory section, after giving an overview of the FCC project referring to the first conceptual design report, the FCC-hh baseline detector for high luminosity hadron-hadron collisions will be detailed including the sub-detector components and radiation environment.

1.1 Future Circular Collider

FCC-hh, like its predecessors LHC and HL-LHC, will be a new particle collider for hadron-hadron collisions planned to build on the border of France and Switzerland for the decade of 2035. It is designed to have a center-of-mass 100 TeV with an integrated luminosity exceeding 30 ab^{-1} after 25 years of operation. The collider will be 97.75 km circum and will use the HL-LHC and upgraded SPS with superconducting magnets as an injector. Injected particles at 3.3 TeV will be accelerated inside the arcs till they reach maximum energy. The sum of arch lengths is planned to be 83.75 km and its lattice of arcs will have 213 m 90^{o} FODO cells (focusing and defocusing quadrupole lenses) and six 14 m-long dipoles between quadrupoles (18). The distance between bunches will be 25 ns and the population of each bunch is exptected to be 10^{11} particles. In order to accelerate the beam on the proper orbit of the accelerator, the magnetic field of the dipole has to be around

16 T (18–20). This is a challenging task for today's magnet technology to keep the beam on the accelerator (21). Yet, R&D programs are working on it to significant improvements (22). Some important parameters of the FCC-hh baseline sutructure are given in Table 1.1 and parameters of LHC and HL-LHC are listed for comparison.

Table 1.1. Key parameters of the FCC-hh comparing LHC and HL-LHC

Parameter	LHC and HL-LHC	FCC-hh
Energy (TeV)	14	100
Circumference (km)	26.7	97.75
Dipole field (T)	8.33	<16
Injection energy (TeV)	0.45	3.3
Peak luminosity (10^{34} cm^{-2} s^{-1})	1.0 (LHC) and 5.0 (HL-LHC)	5.0 (initial) and 30.0 (nominal)
Number of bunches *n*	2808	10 400
Bunch spacing (ns)	25	25
Bunch population N (10^{11})	1.15 (LHC) and 2.2 (HL-LHC)	1.0

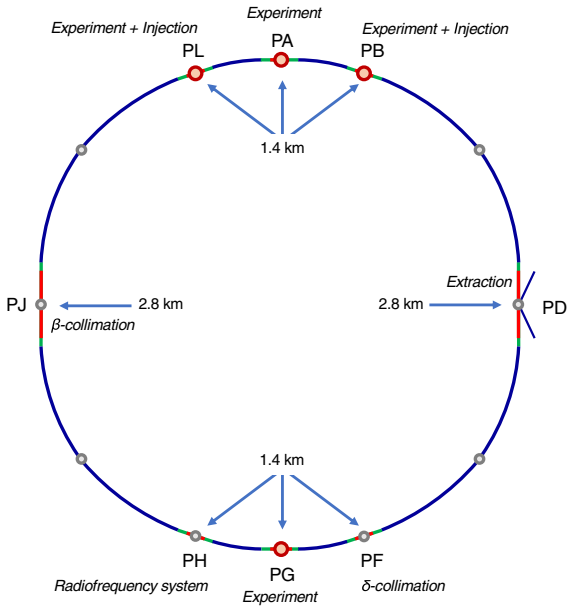

Figure 1.3. The FCC-hh collider ring layout. Taken from (17)

It is planned to be accelerated particles collide at the four collision points on the FCC-hh. In Figure 1.3, the conceptual collider ring design is illustrated with four collision points (PA, PB, PL and PG), and particle injection points (PB and PL). Two of these collision points, PA and PB, are planned to be high luminosity

experiments just as ATLAS and CMS on the collider. Other two experiments, PB and PL, will be low luminosity experimets like ALICE and LHCb. Events after collisions must be recorded by high tech equipped detectors in the experiments. The detectors are designed to be capable for 100 TeV center-of- mass energy with an integrated luminosity 30 ab^{-1}.

The FCC-hh detectors will face more challenges than their predecessors since the collision energy is 7 times larger than the current energy of LHC. The increase in the energy leads to larger cross-sections for SM processes and the higher instantaneous luminosity increases the pile-up of events in a single collision. These features of the FCC project make it a machine for precision measurements and a discovery machine. For example, more than 10^{10} Higgs bosons are expected to be produced in the experiments for 25 years operation. The amount of Higgs produced will be several thousand more than in the LHC and 200 times larger than in the HL-LHC. The statistic will not only help to precision measurements but also be useful in the separation of Higgs signal from huge backgrounds. Some simulation studies performed 100 TeV p-p collisions compared to 13 TeV for gluon-gluon fusion Higgs (23) decaying to 4 leptons and Vector-Boson Fusion (VBF) Higgs (24) decaying to jets. The results of the simulations show that detectors must cover large pseudo-rapidity to mentioned measurements. The maximum pseudo-rapidity distributions of final state particles of two channels are shown in Figure 1.4. The detector has to cover $|\eta| < 3.8$ for 13 TeV and $|\eta| < 4.8$ for 100 TeV in order to get 95% fiducial acceptance for $p_T > 3$ GeV leptons that comes gluon-gluon fusion channel. In the Figure 2.3 (b), VBF channel produced jets with $p_T > 25$ GeV have broad pseudo-rapidity distribution compared to 13 TeV. The FCC-hh detector needs to be extended $|\eta| < 6$ to reach 90% acceptance for this channel (17).

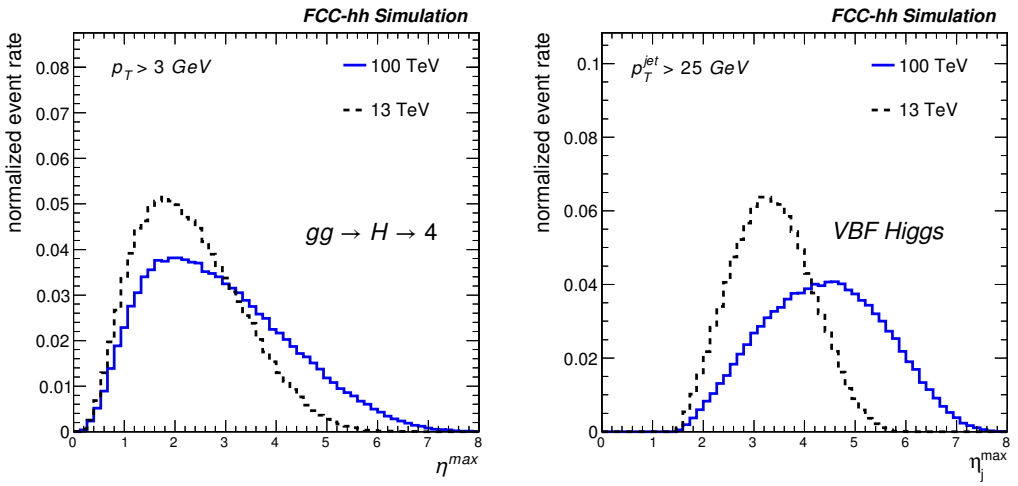

Figure 1.4. The maximum pseudo-rapidity $|\eta^{max}|$ distributions for the lepton that produced gluon-gluon fusion Higgs on the left (a) and jet for the VBF Higgs on the right (b) taken from (17).

In FCC-hh, the pair production of the Higgs that can occur through the Higgs self-interaction will be increased by a factor of 40% compared to HL-LHC and it can be measured with an accuracy 5% according to the simulations (15,17). These measurements of the Higgs boson are expected to even lead to the discovery of exotic Higgs decays. In addition to Higgs measurements, the dynamics of the electroweak symmetry breaking can be investigated at the TeV scale. Moreover, the new particles can be searched for symmetry-breaking models that are alternatives of the Standard Model. Therefore, the FCC detector must handle the challenge of all these measurements and record the events that have multi-TeV jets, very high p_T leptons and photons from heavy resonances as precise as possible. The demanding radiation environment of the LHC experiments has made way for R&D projects that aim to overcome endurance problems. Recent developments in semiconductor technology have made the pixel detectors more radiation tolerant. Unfortunately, this golden age for particle detectors is not enough for the needs of the FCC-hh. The granularity of current tracker and calorimetry will not be enough for detection of all events due to a large number of p–p collisions of an FCC-hh collision per bunch-crossing at 100 TeV energy and a pile-up of 1000 interactions per bunch-crossing, comparing to the 200 interactions expected for the HL-LHC, and the 60 interactions measured at the LHC. The projected value of pile-up events at this energy level is becoming very difficult problem and it is planned to be solved with high precision time and position measurements in its tracker and calorimeter.

1.2 Reference Detector Design

The FCC-hh reference detector is planned to have 50 m of length with 20 m of diameter. The detector will be similar in size to the ATLAS detector at the LHC. The reference detector is designed to track all particles without any loss for $|\eta| < 6$ values. However, it is still expected to evolve in the decades to come and R&D projects for its subsystems are ongoing. The reference detector design is shown in Figure 1.5. From the center of the detector, one can find tracker, electromagnetic and hadron calorimetry, respectively. The layout of the center is housed in a 4 T solenoid with a diameter of 10 m cavity. This allows coverage of $|\eta| < 2.5$ for the central part of the detector. As discussed in the previous section, the detector will be precise and a reconnaissance machine. The new physics events are expected to be in the forward region according to the simulation studies. Therefore, it should measure $|\eta| > 2.5$, meaning forward coils are required for the detector. Adding two forward magnet coils with a diameter of 5 m cavity will lead to high precision momentum measurement of $|\eta| \approx 4$ and tracking $|\eta| \approx 6$ for a given 4 T magnetic field in the total solenoid volume of 32 m length. The outer layer of the detector is the muon system that covers the entire detector. In Figure 1.6, the longitudinal cross-section of the reference detector has been shown indicating the sub-systems with different colors.

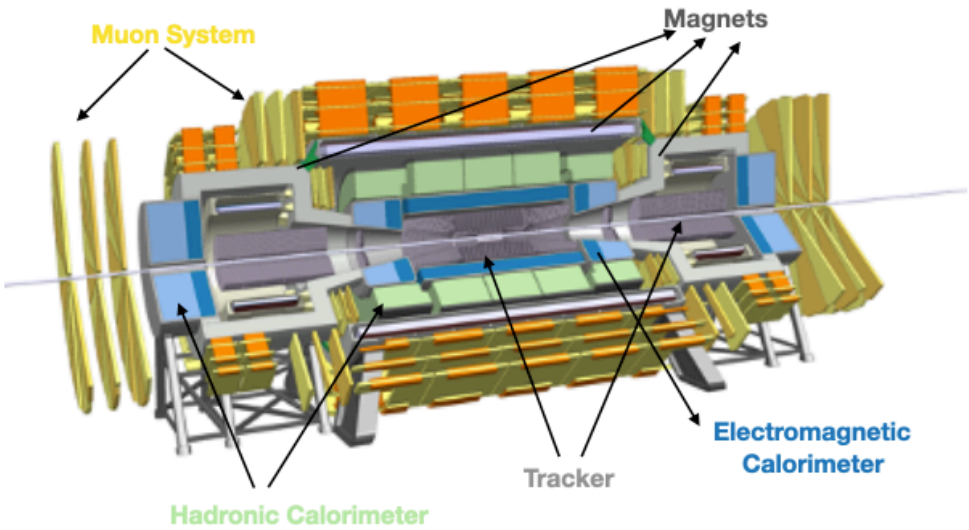

Figure 1.5. The reference FCC-hh detector layout. The figure reproduced from (17).

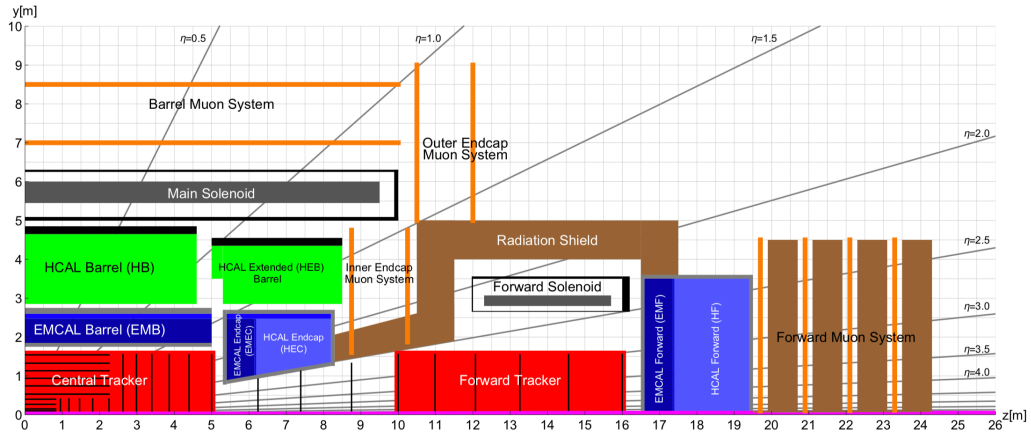

Figure 1.6. The longitudinal cross-section representation of the FCC-hh referance detector. The red, blue, green and orange colors indicate tracker, electromagnetic calorimeter, hadronic calorimeter and muon system, respectively. The figure reproduced from (17).

1.2.1 Tracker

When the number of pile-up events is considered at 100 TeV center-of-mass energy, vertexing and *b*, *c*, *τ*–tagging performance have to be efficient as never before. Hence, the tracker of the FCC detector must have adequate momentum resolution ($\Delta p_T/p_T$) to detect not only high p_T particles but also low ones. The Phase-II trackers of ATLAS and CMS experiments have 10% at p_T = 1 TeV efficiency. The planned momentum resolution for the FCC-hh tracker is 20% at p_T = 10 TeV with less than 1% occupancy at the luminous region. The momentum resolution of tracker can be evaluated by the Gluckstern formula (25);

$$\Delta p_T/p_T \approx \frac{\sigma_{R\Phi} p_T}{0.3BL^2} \mathrm{f}(N) \qquad (1.1)$$

where p_T [GeV] is transverse momentum of particle, $\sigma_{R\Phi}$ [m] is granularity of tracker, B [T] represents magnetic field inside the detector, L [m] is the tracker lever-arm length and $f(N) = \sqrt{\frac{720}{N+4}}$ is the factor that corrects of the layout geometry for N equidistant tracker planes.

In order to reach the expected momentum resolution at 4 T magnetic field with a tracker lever-arm of L = 1.55 m, two important parameters play a key role in the momentum resolution. The first one is the granularity in R-Φ plane. If it is small enough like $\sigma_{R\Phi}$ = 9 μm, the tracker performs better efficient tagging with good

momentum resolution (26). Another important factor is the number of layers, *f(N),* in the tracker of the detector and it can be found as 12 layers for given L, B, $\sigma_{R\Phi}$ and p_T using the Eq. 1.1 for the planned momentum resolution. At first glance, a large number of layers can be seen logical for good tracking efficiency. However, the ideal detector allows low multiple scattering inside and has large number of layer. Thus, the layers of the tracker have to be thin and have low amount of services. The industrially produced silicon CMOS sensors that require less cooling power can be thinned down to 50 μm and have low cost, are perfect candidate for the detector tracker. The amount of track hits in each layer arises a track reconstruction problem. More layers (N) also lead to more material budget that increases uncertainties from the multiple-scattering. The layers are planned to be placed in the reference tracker dividing into three regions. Two geometry options, tilted or flat, are in the considerations in the placement of tracker elements and referance tracker layout of the FCC-hh detector has been shown in the Figure 1.7 for these geometry options. The tilted option is under consideration for the FCC-hh reference dectector tracker.

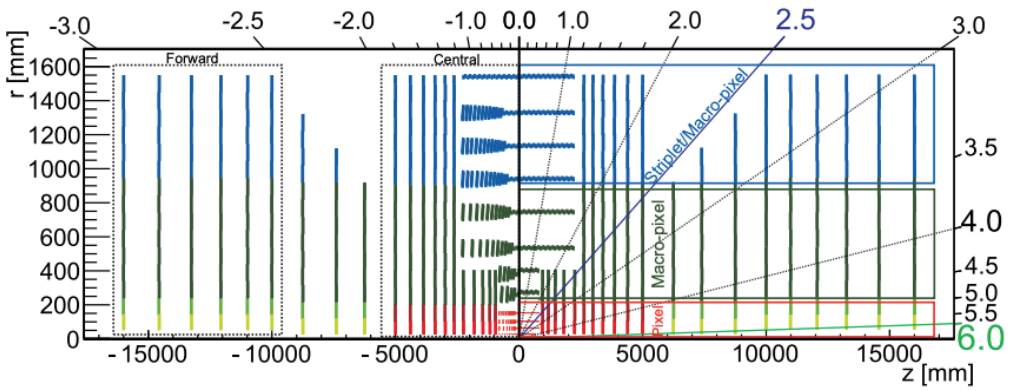

Figure 1.7. The layout of FCC-hh reference detector tracker for "*tilted*" (left) and "*flat*" geometry options representing regions (pixel, macro pixel and strip barrels) (17).

According to the simulation studies (25,26), the tilted geometry shows that less material cost (X/X_0) for the transition region $|\eta| > 2.0$ and $|\eta| < 4.0$ reducing the probability of hadronic interactions. The simulation results of study are shown in Figure 1.8 reffering the material budget as units in radiation lenght (X/X_0) and nuclear interaction lenght (λ/λ_0) if track has 10 hits. The red, orange and green colors represent the end-cap (EC), barrel (BRL) and beam-pipe (BP), respectively. Two different scenarios are tested for the tilted and flat geometries seperately. While the

BP, BRL and EC are considered together in the first scenario, BP and BRL are taken into account for the second case. Both scenarios show that the material budgets perform better for the tilted layout.

The tracker has four-pixel barrels in the innermost region (r < 200 mm). In order to have good seeding, the pixel size is 25–33.3 μm × 50 μm and the number of readout channels is 5.5×10^9 in that region. The intermediate region (200 < r < 900 mm) of the tracker has 4 macro-pixel barrel layers. The size of macro-pixels is 33.3 μm × 400 μm and have 1×10^{10} channels. Those will hold an occupancy limit of tracker around 1%. Lastly, 4 barrels consisting of an array of 33.3 μm × 2–50 mm strip or macro-pixels layers will be placed in the outermost region (900 < r < 1600 mm). This layer will have 5×10^8 readout channels and the total readout channel size of the tracker is 16×10^9. The tracker design aim for the particles that come from pile-up events can be subtracted from the primary vertex for high p_T particles since the Gaussian profile (σ) of colliding bunches is around 75 mm. If the position measurements are supported by precise time measurements for each track, the remnants of the pile-up vertices can be mitigated from the actual vertex. The HL-LHC can cope with the fake tracks from 140 pile-up events at 25 ps time resolution at $|\eta| = 4.0$. On the other hand, it seems 5−10 ps per track is crucial for the FCC-hh detector to reduce that pile-up effect sufficiently at $|\eta| < 3.5$.

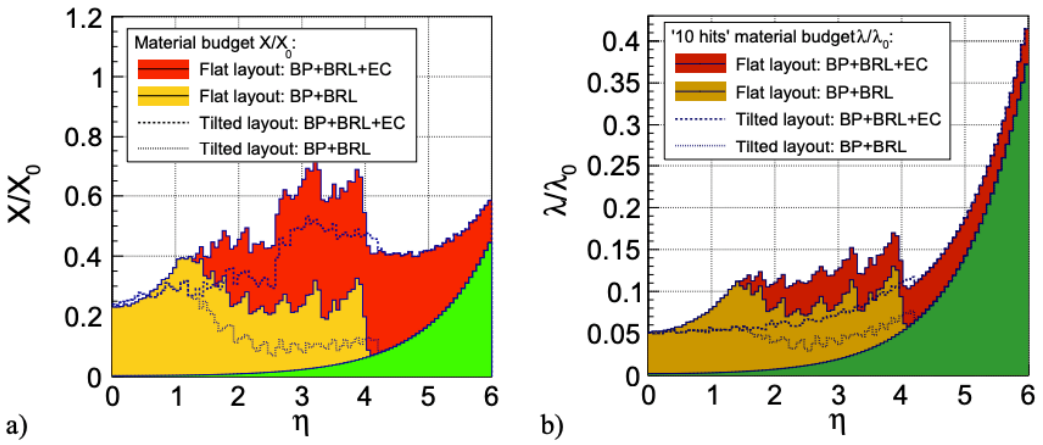

Figure 1.8. Simulations results of two different geometries, tilted (dashed lines) and flat (straight lines with colors), layout in terms of material budget in units radiation length (X/X_0) on the left (a) and material budget of nuclear interaction length (λ/λ_0) for 10 hits required track on the right (b) (17).

In nut shell, the tracker is the detector's most demanding subsystem considering granularity and pile-up events. In addition to these factors, the tracker of the detector environment should be resistant to radiation environment. Due to the pile-up events, the particle flow will be immense amount around the beam line and forward trackers. This reveals another challenge for the tracker system of the detector in terms of not only ionizing but also non-ionizing radiation. The expected radiation amount is higher than the current limits of LHC and HL-LHC. Fortunately, advances in technology and ongoing R&D have promising examples for future tracker systems. In this thesis study, the development process of one of these, MALTA, will be discussed in the next sections in detail. Moreover, the radiation environment of the detector will be discussed in a later section, showing the simulation results.

1.2.2 Calorimetry

The calorimeter of the FCC-hh baseline detector is the part of the detector where the energy of the particles is measured with good resolution. The calorimeter consists of electromagnetic (ECAL) and hadronic (HCAL) calorimeter. The ECAL and HCAL must require some energy resolution over the energy range, separately. Both of them have three sections; barrel, endcap and forward. Properties of each section differs from each other, leading to different the energy resolution, granularity and maximum radiation dose. Generally, the energy resolution of a calorimeter depends on three terms and can be shown as follows;

$$\frac{\sigma_E}{E} \approx \frac{a}{\sqrt{E}} \oplus \frac{b}{E} \oplus c \tag{1.2}$$

where a is the stochastic term due to the shower fluctuations and sampling, b is the noise term that comes from the electronic noise of readout systems and pile-up. Lastly, constant term c represents the other effects such as differences in the calibration of the cell-to-cell, shower leakage, etc. Those terms can have different contribution to the resolution in the sections of the ECAL and HCAL.

The design of ECAL is based on the liquid argon (LAr) technology because of the radiation hardness and stability experiences shown in the ATLAS experiment. The Si/Pb or Si/W is the technology to overcome high radiation levels which is around 1 MeV neutron equivalent (n_{eq}) fluence of $10^{16}/cm^2$. The absorber

directly affects the Molière radius (R_M), resulting in smaller cluster sizes if has a large atomic number (Z). The LAr and Si/Pb combination reach R_M = 5.7 cm. In fact, this can be improved with the Si/W option but the combination of LAr and Si/Pb option was considered in the conceptual design of calorimeter. In the of ECAL barrel (EMB), the straight 50° inclined 2 mm steel-plated lead absorbers are assumed unlike the accordion geometry of the ATLAS detector. EMB consists of 8 layers. The layers will be placed between a 5 cm thick aluminium cryostat at the front and 10 cm at the rear. The LAr gap sizes are 1.15 mm at the inner radius but it increases 3.09 mm at the outer radius of EMB. As a result of that, it causes the alteration of the sampling fraction in the radial direction and needs to be calibrated (constant term of c in the Eq. 1.2) for each layer separately. The cross-sectional view of the electromagnetic barrel is shown in Figure 1.9.

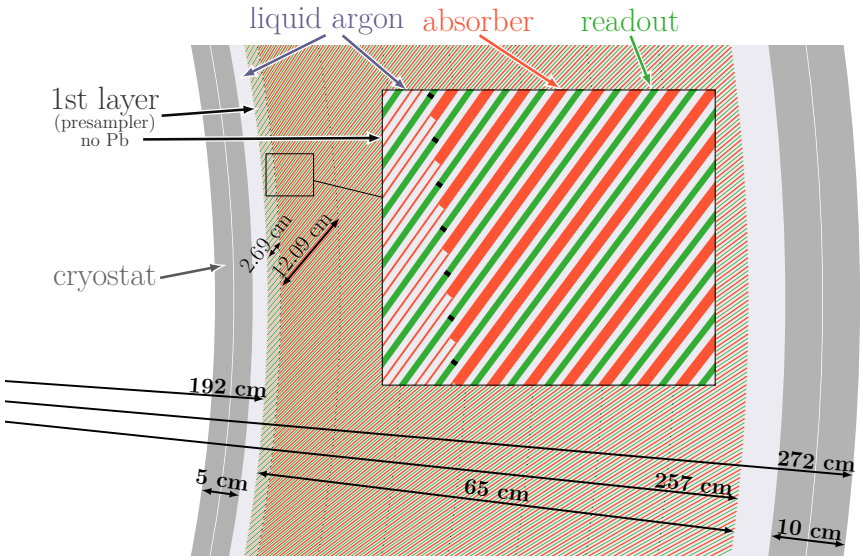

Figure 1.9. The cross-sectional view of electromagnetic barrel of FCC-hh baseline detector (27).

The size of 20 × 20 mm cells are considered to reach the $\eta-\varphi$ granularity of $\Delta\eta \times \Delta\varphi = 0.01 \times 0.009$. The energy resolution and linearity of EMB were simulated in GEANT4 (28) for single electrons and photons according to the design (27). In the simulation, no pile-up environment, $<\mu>$, was taken into account but the electronic noise included. The expected electronic noise level per cluster is determined as 0.3 GeV for desired granularity and geometry. The simulated energy resolution (a) and linerity plots (b) for η = 0 are shown in Figure 1.10. As a result of the full simulation, the stochastic and constant terms of the energy resolution

formula (Eq. 1.2) are determined as $a = 8.2\%\sqrt{GeV}$ and $c = 0.15$ for single electrons. The obtained results of the single photons (red) are similar to the results of the single electrons (blue) and both are shown in Figure 1.10 (a). The upstream material correction and the response scaling factors are included to study for both particles. One of these factors, upstream material correction, is extracted simulating electrons because the low-energetic photons result in extra overestimation of energy deposition. This behaviour can be seen clearly in Figure 1.10 (b). On the other hand, the response scaling factor is evaluated from the response of 100 GeV photons. The ratio of 1/0.96 is applied as energy-independent factor to the scale cluster energy. This compensates the deposited energy outside of the reconstructed cluster (27).

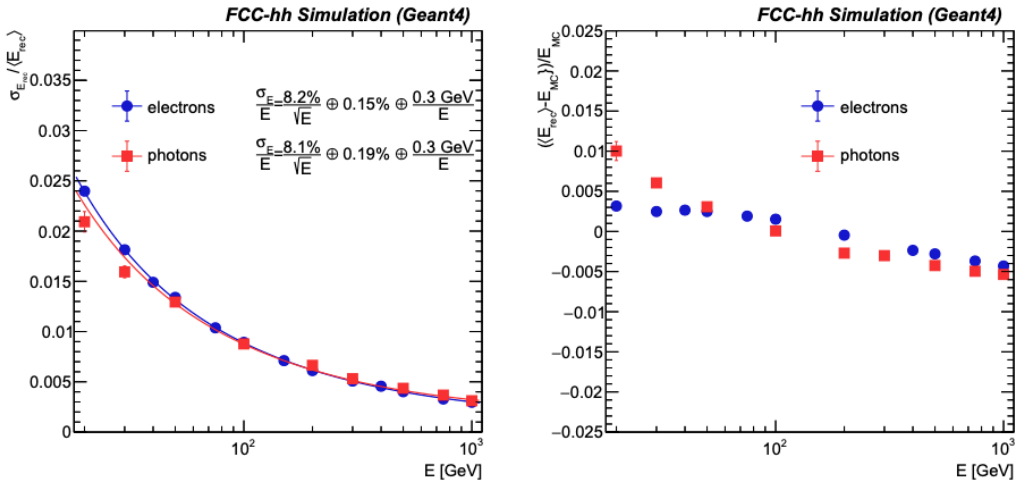

Figure 1.10. The obtained simulation results of energy resolution (a) and linerity response (b) of EMB for single electrons (blue) and photons (red) at $\eta = 0$ (27).

However, the energy resolution parameters become large, especially noise term (b) when pile-up events are taken into account. Another simulation shows that the noise terms of pile-up environments $<\mu> = 200$ and $<\mu> = 1000$ reaches to $b = 0.65$ and 1.31 GeV, respectively (27). Dependency of the energy resolution of electrons for different pile-up environment are shown in the Figure 1.11 (a). In order to determine effect on the mass of Higgs, another simulation was done with Phytia8 (29) and the Higgs mass, which decays to two photons, reconstructed with the photons have clusters with energy $E_\gamma > 30$ GeV without any particle identification and isolation cut. The reconstructed mass width increases (σ_m/m) from 1.32% to 1.9% and 2.29% for $<\mu> = 200$ and $<\mu> = 1000$, respectively. These results were obtained for the optimized cluster size of $\Delta\eta \times \Delta\varphi = 0.03 \times 0.08$. The Higgs mass peaks for different

pile-up environments are shown in the Figure 1.11 (b). One can say that wide mass peaks show the importance of the pile-up substraction for <μ> = 200 and <μ> = 1000.

The hadronic calorimeter (HCAL) of the FCC-hh detector consists of a central (HB) and two extended barrels (HEB). In this part of the detector, radiation levels are as not high as EMB. Therefore, scintillating tiles are decided for the calorimeter design because of cost and performance. The design is based on the ATLAS Tile Calorimeter (30). The Tile Calorimeter (TileCal) module is combination of stainless steel, lead and plastic scintillator planes. The design of hadronic calorimeter consists of 128 TileCal module perpendicular to the beam axis. Inside of the each TileCal module, central and two extended barrels have 10 and 8 longitudinal layers, respectively. The layers contain two scintillating tiles that are covered reflective material and read out by silicon photomultipliers (SiPM) through wavelength shifting (WLS) fibers. Between two scintillating tiles, there are two 0.5 cm thick stainless-steel plates and a 0.4 cm thick lead plate in the middle of them. The planned design and cross-section of a TileCal module is shown in Figure 2.11, pointing out scintillating tiles, lead and steel planes with green, red and white colours, respectively. As it shown in Figure 1.12 (a), tiles lengths enlarge with the radius and layer from 6.9 cm to 13.3 cm. Similarly, the height of the tiles increases from 10 cm to 25 cm.

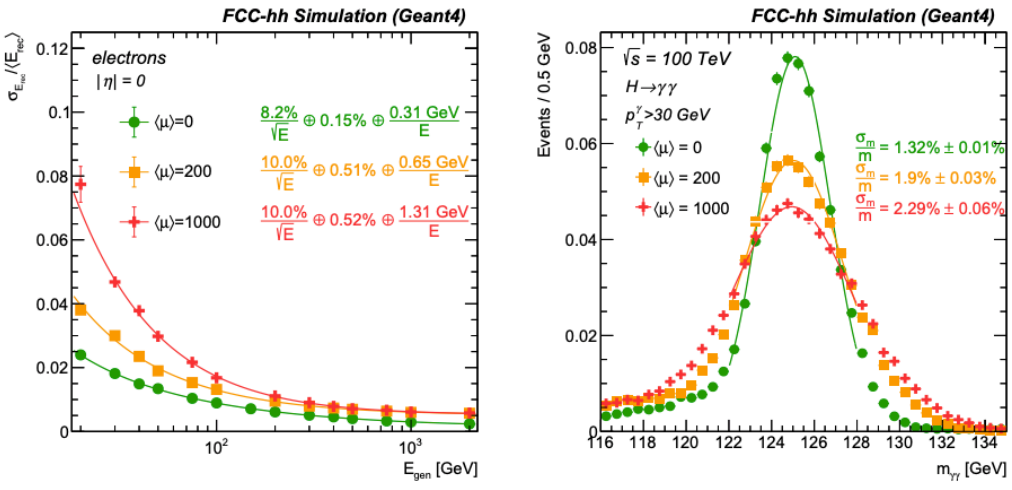

Figure 1.11. (a) The energy resolutions of single electrons as a function of photon energy at $\eta = 0$ are represented for different pile-up environments indicating noise terms. (b) Pile-up environment effects on invariant mass of Higgs distribution are shown for mass width (σ_m/m) (27).

In TileCal, it is aimed to achieve the η−φ granularity of Δη × Δφ = 0.025 × 0.025 up to |η| = 1.81, including the HB and HEB. The performance of the design has been simulated to see effect of the scintillator/lead/steel mixture. In simulations, the scintillator/steel mixture of the ATLAS detector, 1/4.7, were considered for an effective calorimeter depth of 9 λ. This mixture results in stochastic term a = 43%$\sqrt{\text{GeV}}$ and constant term c = 4%. However, the mixture of scintillator/lead/steel 1/1.3/3.3 results in lower constant term and improves the resolution for 8.3 λ at η = 0 because of uniter e/h ratio and improved lineartiy (27). Another simulation was performed to obtain single pion resolution from combination of electromagnetic and hadronic barrel at η = 0.36 which corresponds the 10.5 λ as total effective depth. Since EMB and HB have different e/h ratios, simple hadronic calibration (benchmark method) must be applied for the correction (27). The simulation results of the pion resolutions are shown in the Figure 1.12 (b) with red and blue color markers for the applied 0 T and 4 T magnetic fields, respectively. Due to energy loss in the cryostat walls, constant term increases from 1.7% to 2.2% and stochastic terms goes up from 44% to 48% once magnetic field applied. In short, the simulation results show that the constant term can be below the target c = 3%.

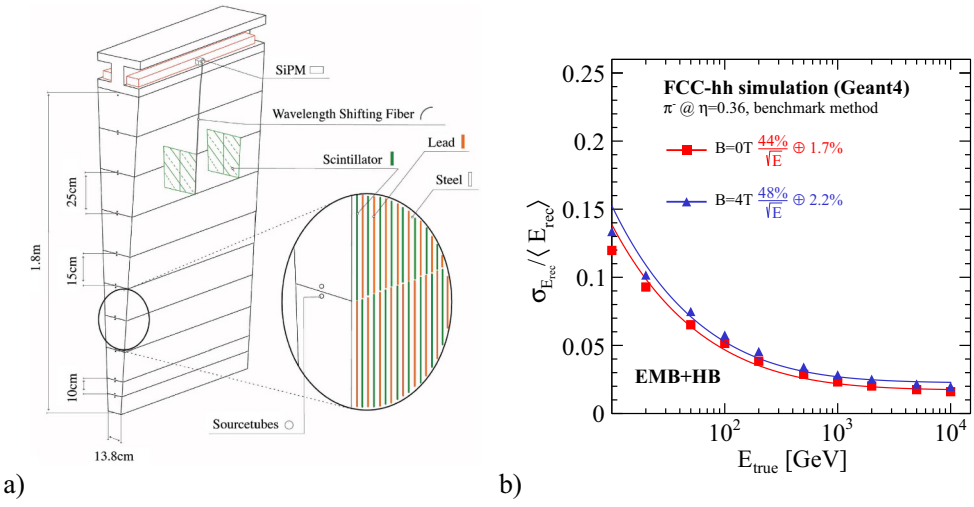

a) b)

Figure 1.12. (a) The design and cross-section of a TileCal module of HCAL barrel. (b) Obtained energy resolution distributions of single pion with benchmark method for EMB and HB (27).

Pile-up environment is also simulated for EMB and HB. In the study, the topological cluster algorithm (31) is used in the reconstruction of single pions and jets considering electronic noise, requiring R < 0.4 value. In Figure 1.13 (a), energy

resolution distributions of single pions for the pile-up environment of $<\mu> = 0$ and $<\mu> = 200$ are shown with green and orange colours, respectively. When the simulation results are compared the previous results that use simple hadronic calibration, large stochastic term is obtained for the pile-up environment of $<\mu> = 0$ because of electronic noise. In the pile-up of $<\mu> = 200$, effects on the stochastic term becomes immense due to the lack of cluster calibrations and non-optimized thresholds. This obviously reveals an important calorimeter requirement in the reconstruction clusters and algorithms to cope with pile-up environment. Jet momentum resolution is obtained with magnetic field B = 0 T at the pile-up of $<\mu> = 0$ but including electronic noise. In the simulation, anti-kt jet cone algorithm (32) were used in reconstruction process of the jets after the topological cluster algorithm. Obtained jet momentum resolution is shown in Figure 1.13 (b). In the presence of a magnetic field T = 4 T, 15% of the charged particles cannot reach the calorimeter if the jet has p_T < 100 GeV. On the other hand, jets with p_T > 1 TeV will not be affected by a magnetic field, which can help in the discovery of heavy narrow resonances such as Z' in large pile-up environments (27).

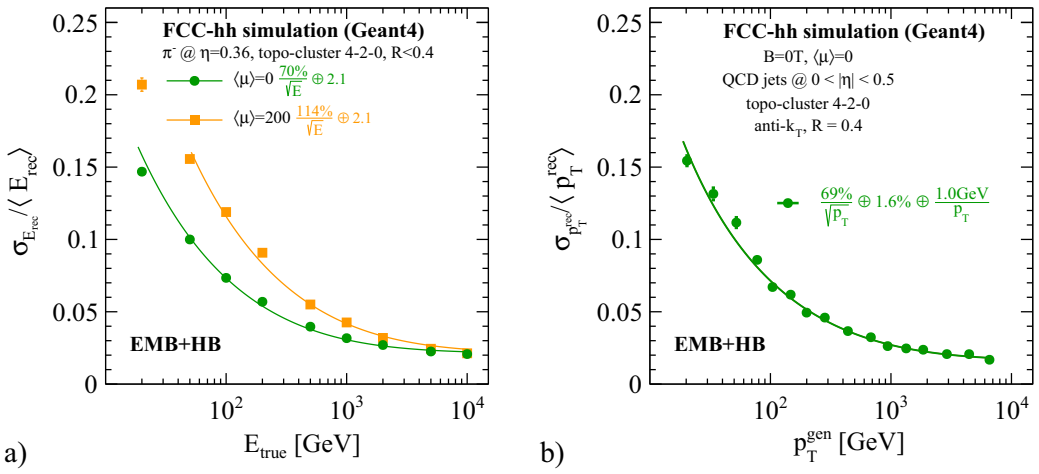

Figure 1.13. (a) Single pion energy resolution distribution that obtained by topo-cluster algorithm (R < 0.4) for the pile-up of $<\mu> = 0$ and $<\mu> = 200$ including electronic noise. (b) The energy resolution distribution of reconstructed anti-kt cone algorithm with R < 0.4 after topo-cluster method at the absence of pile-up events and magnetic field (27).

The layout design of the endcap of the calorimeter is also inspired by the ATLAS experiment. The endcap of the electromagnetic calorimeter (EMEC) will be placed in the same cavity as the endcap of the hadronic calorimeter (HEC). Both will share the same cryostat and LAr technology will be used as an active medium to overcome the radiation load in the endcap. The detector volume will cover the region $1.5 < |\eta| < 2.5$. In the EMEC part, 1.5 mm lead discs as absorbers are used and there is a readout PCBs placed with a gap between absorber discs. Two 0.5 mm thick LAr will be filled into the gap of the two absorbers and PCB. On the other hand, the HEC part uses the 40 mm thick copper discs and 1.2 mm read-out PCB between two discs. Between two absorbers and PCB, two LAr gaps with a size of 1.5 mm thick will be placed. There will be no angular orientation in the placement of absorbers and PCB layers for both parts of the calorimeter. The cross-section of the calorimeter endcap is shown in Figure 1.14 indicating EMEC and HEC with green and red colours, respectively.

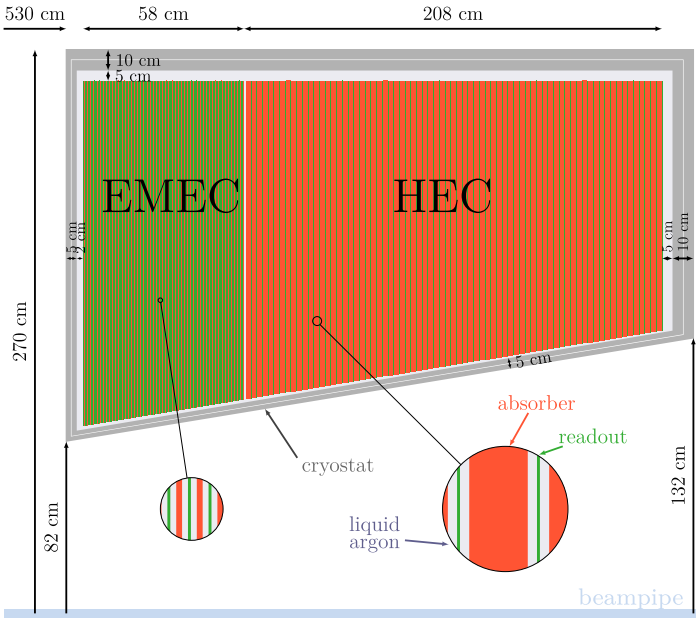

Figure 1.14. Cross-section of endcap calorimeter of FCC-hh baseline detector (27).

The forward calorimeters will be the most challenging part of the detector in terms of radiation dose exposure. The expected ionization dose is up to 5000 MGy and 1 MeV neutron equivalent fluence is 5×10^{18} cm^{-2}. This amount of radiation fluence is 15 times larger than the fluence that will be experienced in the forward calorimeter of HL-LHC. Thus, the LAr with an active material is again an option to cope with the radiation environment. It is designed to cover the large

region between $|\eta| > 2.5$ and $|\eta| < 6$. Similar to the endcap part of the calorimeter, the forward electromagnetic (EMF) and hadronic calorimeters (HF) will share the same cryostat cavity. The absorber material will be copper for the EMF and HF. In the EMF, the LAr gap is planned to be 0.1 mm between the thickness of 0.9 mm absorbers. For the hadronic part, the thickness of the absorber discs is 40 mm and the LAr gap is kept at 0.1 mm. The reason for such a thin LAr gap design lies in the prevention of ion build-up at large energy densities. The cross-section view of the forward calorimeter is shown in Figure 1.15 indicating EMF and HF with yellowish and red colours, respectively.

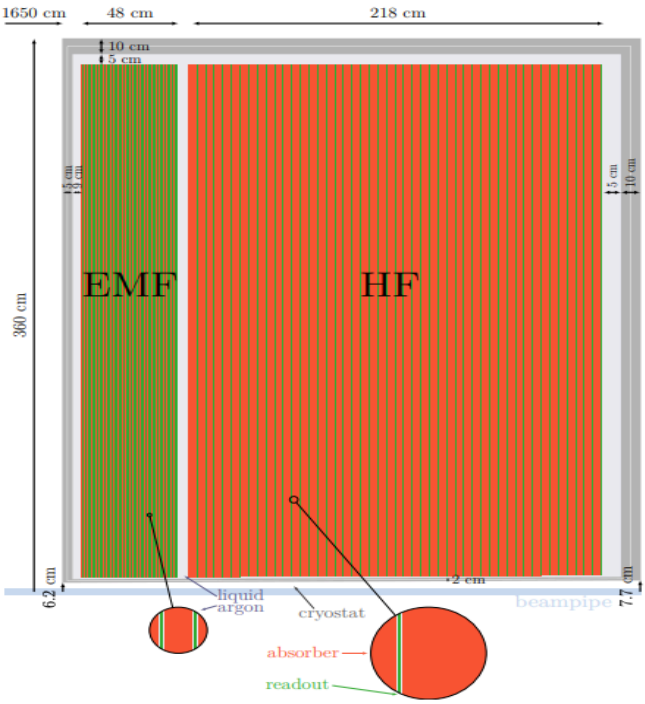

Figure 1.15. Cross-section of forward calorimeter of FCC-hh baseline detector (27).

Similar to the simulation studies of electromagnetic and hadronic calorimeters, energy resolution simulations were also performed to evaluate stochastic and constant terms for the endcap and forward calorimeters of the FCC-hh baseline detector. In Table 1.2, the simulation results of the stochastic and constant terms of the energy resolution are listed detailing granularities, radiation fluence and dose, technology and number of layers for given electromagnetic and hadronic calorimeter unit.

Table 1.2. The electromagnetic and hadronic calorimeter units for acceptance, energy resolution, granularities, radiation fluence and dose, techonology and number of layers (17).

Unit	η_{min}	η_{max}	a ($\%\sqrt{GeV}$)	c (%)	Δη	Δφ	Fluence (cm^{-2})	Dose (MGy)	Material	Layer (N)
EMB	0	1.5	10	0.7	0.01	0.009	5×10^{15}	0.2	LAr/Pb/PCB	8
EMC	1.5	2.5	10	0.7	0.01	0.009	3×10^{16}	4	LAr/Pb/PCB	8
EMF	2.5	4	10	0.7	0.025	0.025	5×10^{18}	5000	LAr/Cu/PCB	6
	4	6	30	1	0.025	0.025	5×10^{18}	5000	LAr/Cu/PCB	6
HB	0	1.26	50	3	0.025	0.025	3×10^{14}	0.006	Sci/Pb/Fe	10
HEB	0.94	1.181	50	3	0.025	0.025	3×10^{14}	0.006	Sci/Pb/Fe	8
HEC	1.5	2.5	60	3	0.025	0.025	2×10^{16}	1	LAr/Cu/PCB	6
HF	2.5	4	60	3	0.025	0.025	5×10^{18}	1000	LAr/Cu/PCB	6
	4	6	100	10	0.05	0.05	5×10^{18}	1000	LAr/Cu/PCB	6

1.2.3 Muon System

The muon detector is located outside of the calorimeter of the FCC-hh baseline detector. In this part of the detector, the aim is to provide excellent muon identification with high momentum resolution. Its design is based on the experience with the ATLAS experiment. The muon system of the FCC-hh detector will use recently developed small diameter Monitored Drift Tube chambers (sMDT) for ATLAS upgrades (33). The sMDT layers that are prepared to be installed in the ATLAS experiment during the upgrade are shown in Figure 1.16 (a) as an example (34,35). The sMDT has a small diameter of 15 mm and thin aluminium walls with a thickness of 0.4 and are expected to fill with 93% Ar and 7% CO_2 gas mixture at 3 bar pressure. In the $|\eta| < 1.5$ region, four 2.8 m long four of sMDT tubes will be used in the plane. In front of the planes, resistive pad chambers (RPC) will be placed to provide a trigger and the two planes will be separated by a 1.4 m gap as shown in Figure 2.15(b). The RPC planes, which have 1 mm gas gap, will be filled with 94.7%, 5% and 0.3% $C_2F_4H_2$/Isobutane/SF_6 gas mixture respectively (36). The gas mixture provides a much faster response but it is highly flammable and not environmentally friendly. The structure of RPC is illustrated in Figure 1.16 (c).

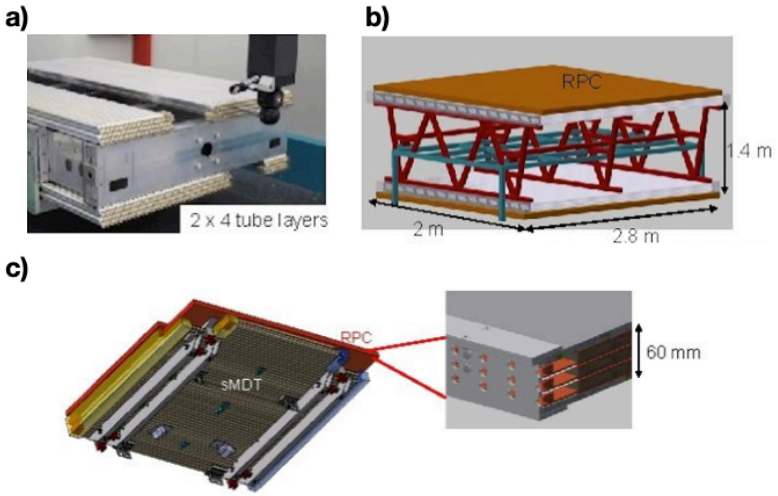

Figure 1.16. (a) The sMDT layers that will be used in ATLAS. (b) Illusturation of sMDT and RPC planes. (c) The structure of RPC plane. The figures are taken from (33,34,37).

The placement of the planes will be parallel to the beam axis in $|\eta| < 1.5$. However, orientation of the planes will be perpendicular to the beam line in region of $|\eta| > 1.5$ and $|\eta| < 2.1$. The region between $|\eta| > 2.1$ and $|\eta| < 2.5$ still under investigation because of the shielding part of the forward solenoid (see Figure 1.6). In order to reach same resolution values as in $|\eta| < 1.5$, the length of the tubes are decreased from 2.8 m to 2.1 m and 0.4 m for the $1.5 < |\eta| < 1.9$ and $1.9 < |\eta| < 2.1$ regions, respectively. This layout reaches ~40 μm spatial and ~60 μrad angular resolution. These resolution values are sufficient for the requirements of the detector, but they can be enhanced with different layouts (37).

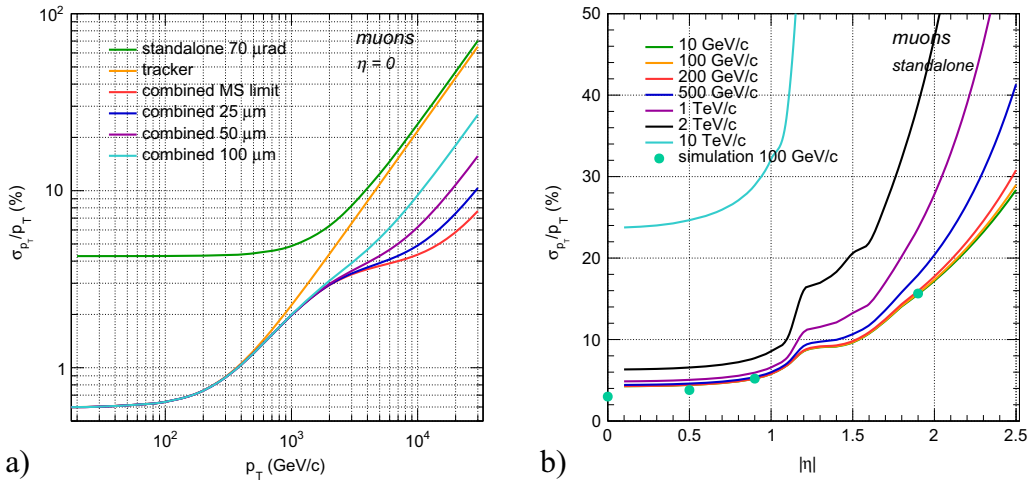

Figure 1.17. (a) Muon momentum resolution, σ_{p_T}/p_T (%), performances of muon detector, tracker and combinations of them at $\eta = 0$. (b) Muon momentum resolution distributions as a function of rapidity for different muon momentums (17).

The muon momentum resolution, σ_{p_T}/p_T (%), performance of the designed muon system has been investigated in a detail. As a result of performance study, muon momentum resolution was obtained by considering a stand-alone muon system, muon momentum resolution of tracker and a combination of these two. While the stand-alone muon resolution performance was obtained by calculating the angular difference between the track angle in the muon system and the radial line connection to the beam axis, tracker performance was determined by only the tracker system of the detector. Lastly, a combination of two methods has been performed assuming different levels of position resolution such as 25 μm, 50 μm, 100 μm in the muon system. In addition, muon resolution performance should consider the multiple scattering in the calorimeters. The momentum resolution results are obtained with the muons at $\eta = 0$ and all of methods are represented using different colour lines in Figure 1.17 (a) as function of muon p_T. As seen, the combined results of the multiple-scattering limit (red line on the figure) and the 50 μm position resolution (magenta line on the figure) in the muon detector can reach 4% and 6% muon momentum resolution for muon momenta 10 TeV, respectively. The results show that the layout design of muon system reaches expected muon momentum resolution. Another momentum resolution study is performed by simulating different muon momemtum with respect to the rapidity. In the study, only stand-alone performance of the muon detector is taken into account to obtain muon momentum resolution and the results are shown in the Figure 1.17 (b). Due to multiple scattering, muon momentum resolution is limited to 28% for the muons below 1 TeV at $|\eta| = 2.5$. Beyond the $|\eta| > 2.5$, dipole magnets have to be used in the forward region to get a muon trigger like in the LHCb and ALICE experiments. Otherwise, the detector provides only muon identification not a muon trigger. The GEANT4 simulation results have been also represented with a dot in Figure 1.17 (b). In this simulation, the FCC-hh baseline detector is simulated, including all detector effects. It is seen that the same muon momentum, 100 GeV, overlaps with standalone simulation results.

From the operational point of view, muon detector needs to handle the muon flux with sufficient momentum resolution. Therefore, it is important to know the differential cross-sections of the muons that decay from *c*, *b*, *W*, *Z*, and *t* to calculate the expected muon flux from each decay in the muon detector. In Figure 1.18 (a), the differential cross-sections distribution of the muons that decays from *c*, *b*, *W*, *Z*,

and t are evaluated with respect to the rapidity including 5 GeV cutoff on the p_T, separately. Since the expected energy loss in the calorimeters is around 3-4 GeV and muons with p_T above 6 GeV can only be recognized in the muon detector, 5 GeV cutoff on the p_T is required (17). As it can be seen in the Figure, the muons that come from c and b decays have larger cross-sections (≈100 μb) compared to the others. The overall differential cross-section is $\sigma_\mu \approx 200$ μb for muons with $p_T > 5$ GeV and the muon flux over a given area (J_μ) can be evaluated with the equation below;

$$J_\mu = \frac{\mathcal{L} \times \sigma_\mu}{\pi r^2} \tag{2.3}$$

where $\mathcal{L}$ is the luminosity, σ_μ is the muon cross-section and r is the radius. One can calculate the expected muon flux at $r = 650$ cm for the peak luminosity as 20 Hz/cm^2 using the equation. In the region $|\eta| < 2.5$, the muon rates were obtained as a function of the p_T threshold considering two groups which muons from decays of b, c, W, Z, t and the ones that only come from W, Z, t decays. The obtained muon rates of these two groups are shown as a function of p_T threshold in Figure 1.18 (b). As is seen, the rate is below 100 kHz for the muons from W, Z, t at any threshold level. On the other hand, the overall rate is above 20 MHz for the p_T threshold of 10 GeV due to the domination of the muon decays of b and c. It is hard to find a p_T threshold below 10 GeV for that combination as shown in Figure 1.18 (b). They can be only discriminated at the first trigger level with the help of jets because muons from c and b decays that are not produced alone. High energy photons and charged particles contributes to the background and reaches 1.25 kHz/cm^2 in $|\eta| < 1.5$ area. While this amount increases to 25 kHz/cm^2 in the region of $1.5 < |\eta| < 1.9$, it can be even range from 25 to 250 kHz/cm^2 in the $|\eta| > 1.9$. As a result, the muon detector is needed to be operated at the counting rate of up to 30 kHz/cm^2 with low background occupancy. The design of the muon system decreases the background occupancy from 30% to 4% thanks to the sMDT and RPC layout. Similar to the other subsections of the detector, some studies are still underway to improve the detector's muon system (17).

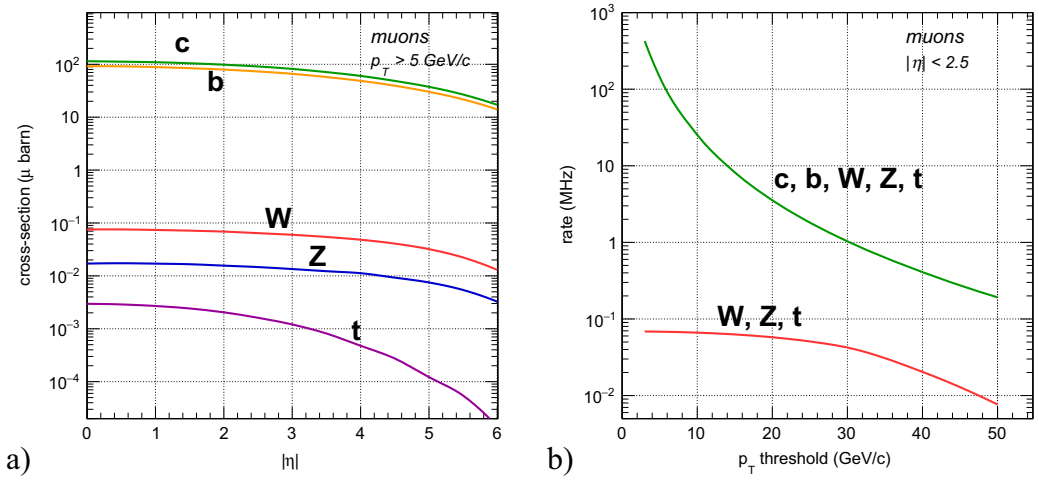

Figure 1.18. (a) Differential cross-section distribution [μb] of muons decays from c, b, W, Z and t with respect to the rapidity. (b) Rate [MHz] distribution of muons from decay of two groups as a function of p_T threshold inside $|\eta| < 2.5$ region. The plots are taken from (17).

1.3 Radiation Environment inside the Detector

Determining radiation levels in the detectors subsystems is important in terms of using more radiation-resistant devices and prolonging the life of the detector. Total ionizing dose and 1 MeV neutron equivalent flux are key numbers for the detector elements and electronics in long-term usage. As mentioned in the subsystems of the FCC-hh detector, expected radiation levels differ from the inner tracker to the calorimeter. In the next chapters of the thesis, the radiation hard CMOS sensor will be detailed giving the motivation of novel technology that can be candidates for future colliders such as FCC-hh. Therefore, total ionizing radiation dose and 1 MeV neutron equivalent fluence for a given radius of the FCC-hh reference detector were simulated in FLUKA (38), and these simulation results can help to determine new technology requirements. In Figure 1.19, obtained simulation results of 1 MeV neutron equivalent fluence (a) and total ionizing dose (b) are shown for 30 ab^{-1} of integrated luminosity (17).

The 1 MeV neutron equivalent fluence value has an important role for the silicon sensors and readout electronics. It is going to be detailed in the following chapter of the thesis, but in short, heavy particles such as protons or neutrons create cavities in the detectors lattice due to interactions at high energies. These cavities are the displacement of the silicon nuclei and it is generally an irreversible process. Hence, it causes serious damage to the detector components. As seen in Figure 1.19 (a), this value is high in the beamline ($r < 2.5$ cm), especially the inner part of the

forward calorimeters. The 1 MeV neutron equivalent fluence is $6\times10^{17}/cm^2$ at a radius of 2.5 cm and z < 500 cm in which the first silicon layer of the tracking system stands. The radiation levels jump to an extreme value which is 5×10^{18} 1 MeV n_{eq}/cm^2 in the forward part of the calorimeters. These numbers are high the current silicon technologies and R&D projects are still ongoing to cope with these values. On the other hand, the radiation values drop 10^{16} 1 MeV n_{eq}/cm^2 at radii > 40 cm and even to $10^{14}/cm^2$ in the region between the barrel and endcap region of the calorimeter. The current technologies can already handle with these radiation fluences.

The total ionizing dose (TID), Single Event Upset (SEU), Single Event Latch-up (SEL) and Single Event Transient (SET) effects are another key factor in the long-term damage of the readout electronics and detector components. These will be briefly discussed later in the thesis, but it is clear that the dose exposure is proportional to the damage to the detector components and electronics. As it shown in Figure 1.19 (b), the total ionizing dose is evaluated around 300 MGy in the first silicon layer of tracker system by FLUKA. According to the simulation results, the dose rises to 5000 MGy in the forward calorimeter regions, which explains why one should prefer LAr technology to overcome such a radiation load. In the hadronic calorimeter barrel region where is 300 cm < r < 500 cm and z < 1000 cm, the radiation amount is between 6 kGy and 8 kGy. These values also enable organic scintillators in use since the total ionizing dose is below 10 kGy (17). In Table 1.3, the average radiation 1 MeV neutron equivalent fluences and total ionizing doses are compared at r = 2.5 for LHC, HL-LHC and FCC-hh (FLUKA simulation). As can be expected, radiation levels are very high at the FCC-hh for both cases. While current technology can handle the expected radiation levels for the HL-LHC, this seems difficult with current technologies for the FCC-hh especially at the tracker of the detector.

Table 1.3. The average radiation 1 MeV neutron equivalent fluence and total ionizing dose comparison at r = 2.5 for LHC, HL-LHC and FCC-hh (17).

Radiation Dose	LHC	HL-LHC	FCC-hh
1 MeV neutron equivalent [$10^{16}/cm^2$]	0.4	3.9	60
Total ionizing dose [MGy]	1.3	13	300

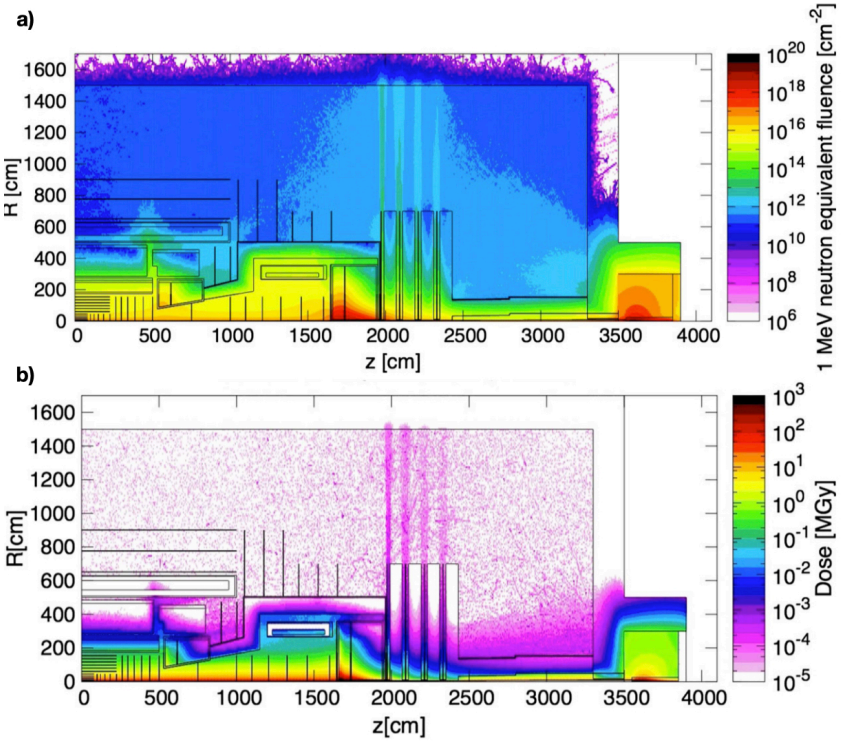

Figure 1.19. (a) 1 MeV neutron equivalent fluence [cm^{-2}] and (b) total ionizing radiation dose [MGy] of the FCC-hh reference detector at 30 ab^{-1} of integrated luminosity. Figures are adopted from (17).

2. SILICON PIXEL SENSORS

Semiconductor detectors have been improved to detect light, nuclear radiation and particles for 50 years. Today, they are used in a wide variety of fields in technology, science and even in particle colliders for high energy physics experiments. These semiconductor detectors are often used in the detector systems of particle colliders to monitor particles formed after collisions. Pixel silicon sensors are used in the inner tracker of the detectors system where particle tracks are constructed in good resolution at high energy experiments. In addition to the inner tracker, different types of semiconductors can be seen in the detector subsystems such as silicon photomultiplier tube (SiPM) in the hadronic calorimeter. As discussed in the previous section of the thesis, particle colliders have harsh radiation environments, which affects not only the efficiency of the track reconstruction but also the lifetime of silicon detectors and the relatively operation of the detector. Therefore, silicon sensors must be resistant to the radiation environment of the detector. In silicon sensors, the radiation damage can be reduced by making modifications on the sensors or their readout systems with the help of the nanometer imaging technology.

In this chapter of the thesis, the working principles of silicon semiconductors will be explained briefly. Then, the section will be followed by the usage of semiconductors as particle detectors and radiation damage in the silicon sensors. Among the silicon pixel sensors, monolithic CMOS pixel sensors will be discussed as subsection of this chapter.

2.1 Semiconductors

In the lattice structure, energy bands are created by electrons made up of interacting with neighbours. The energy bands are full of valence electrons and separated by the energy bandgap. The highest energy band level is considered as the conduction band and the lowest one is defined as the valance band. The energy difference between the conduction band and valance band classifies the material as an insulator, conductor or semiconductor depending on the material. The band gaps between conduction and valence band of the insulator, conductor and semiconductor are illustrated in the Figure 2.1. In the insulators, such as glass, the bandgap is wide and a few of the electrons in the valance band can up the

conduction band at room temperature. In the conductors, however, the bandgap is almost overlapped, allowing the valence electrons to exit the conduction band at even low temperatures. This feature makes the material electrically conductive. On the other hand, in the semiconductors, the bandgap is close enough to excite valence electrons to the conduction band when the enough energy is applied. For instance, the required energy is 1.12 eV in silicon, which excites the valance electrons and breaks the covalent bond between atoms. Once the valance electron is stimulated, it moves to the conduction band and leaves a vacancy known as a hole in the valance band. The hole behaves like a positively charged particle and it can move in the material. The excited electron and created hole are called charge carriers, which are responsible for charge transport. As a result of the charge transport, semiconductor material becomes electrically conductive.

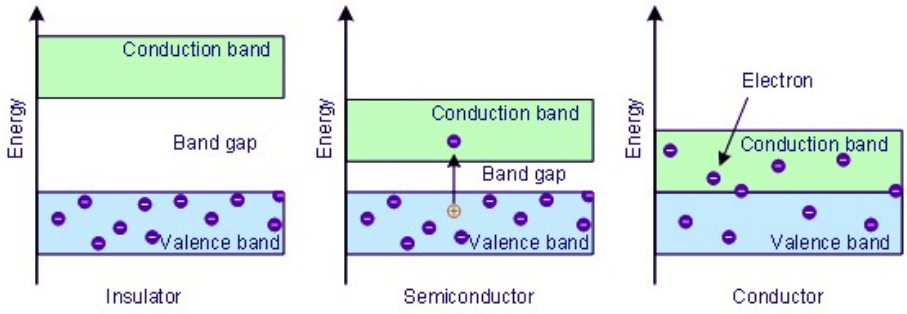

Figure 2.1. The energy band diagrams of the insulator, semiconductor and conductor materials.

The concentration of charge carriers in the semiconductor can be represented as:

$$n = \int N(E) \times F(E) dE \tag{2.1}$$

where the density of states is shown as $N(E)$ and the Fermi-Dirac distribution fuction at energy E is represended with $F(E)$. The Fermi-Dirac distribution function gives the probability of occupancy of energy levels of charge carriers and is represented with following equation:

$$F(E) = \frac{1}{1 + e^{(E-E_f)/k_B T}} \tag{2.2}$$

where E_f is Fermi energy, k_B is Boltzmann constant and lastly T is temperature. The semiconductors can be divided into two types as intrinsic and extrinsic semiconductors. The intrinsic semiconductors are pure semiconductors, while extrinsic semiconductors are modified adding impurities. Considering the pure silicon, its Fermi energy level is in place between conduction band and valance band. Therefore, it is actually poor in electrical conduction and only a limited number of electrons reach the conduction band in room temperature. Unlike intrinsic semiconductors, extrinsic semiconductors have additional charge carriers that are doped deliberately with chemical methods. If a semiconductor is doped with electrons, it is called an n-type intrinsic semiconductor, but if it is doped with holes it is named p-type. For example, a phosphorus-doped silicon becomes an n-type semiconductor because it contains an extra valence electron after bonding with silicon atoms. This process can be reverted to obtain a p-type semiconductor using a boron element. When silicon atoms are bonded with boron, a hole occurs in the valence band. Bonding illusturation of intrinsic and extrinsic silicon semiconductors is shown in Figure 2.2. As a result of doping process, Fermi energy of silicon shifts towards the conduction band and becomes more conductive depending on the dopant level.

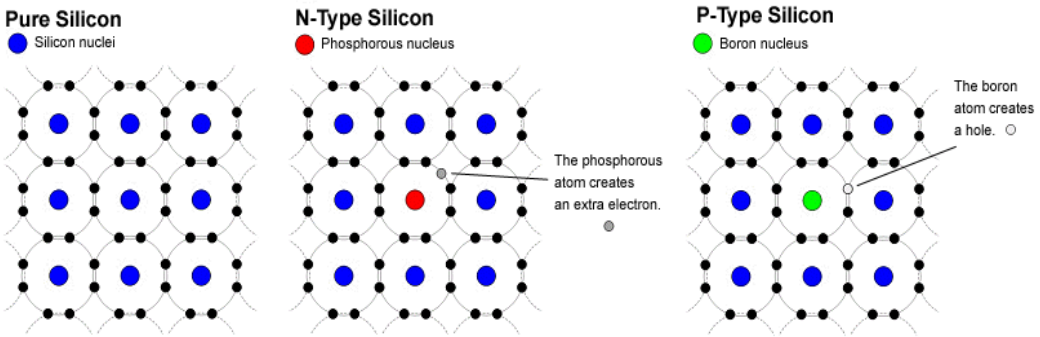

Figure 2.2. From left the right, illustration of silicon bonds within pure, n-type and p-type silicon crystal, respectively.

In extrinsic semiconductors, the charge carrier ratio of n-type (donor) or p-type (acceptor) impurities is expected to be higher than the intrinsic semiconductors. This ratio in the silicon semiconductor affects directly either

current generated or noise because of the charge carriers. Therefore, the ratio should be in a kind of equilibrium to create a semiconductor considering these factors. This equilibrium can be obtained with a p-n junction which is the combination of p-type and n-type extrinsic silicon semiconductors.

2.2 Semiconductor As a Particle Detector

The particle detector basically measures its interaction with the material. Depending on the particle type, the detector type differs but in principle detectors detect the secondary particles that are produced by the deposition of their energy after interactions within the material. For example, high energy photons can be detected with scintillation which produces secondary photons after interaction with the LAr scintillation material. In the end, these secondary photons can be detected by PMTs. Similarly, charged hadrons can be detected by silicon detectors. In semiconductor detectors, the mechanism simply works with valence electrons and holes, which generate an electrical signal when the particle passes through it. The valance electrons are excited if the incident particle energy is enough to break bonds between atoms. Once the valance electron is stimulated, it moves to the conduction band and leaves a vacancy known as a hole in the valance band. The hole behaves like a positively charged particle and it can move in the material. The excited electron and created hole are called charge carriers, which are responsible for charge transport. The movement of the charge carriers generates a current within the semiconductor detector. As a result, an incoming particle is detected by the semiconductor detector. However, the number of charge carriers in the semiconductor depends on energy loss in the material (stopping power) per unit length and it is described with The Bethe-Bloch formula as follows;

$$-\langle\frac{dE}{dx}\rangle = Kz^2\frac{Z}{A}\frac{1}{\beta^2}\left(\frac{1}{2}ln\frac{2m_ec^2\beta^2\gamma^2T_{max}}{I^2}\right)-\beta^2-\left(\frac{\delta(\beta\gamma)}{2}\right) \quad (2.3)$$

where $-\langle\frac{dE}{dx}\rangle$ is the mean energy loss of particle in material with a unit of $\frac{MeV}{g/cm^2}$. The explanations of the symbols used in Eq. 2.3 are explaned in the Appendix. The Bethe-Bloch formula defines the mean particle energy loss per unit length in the range $0.1 \leq \beta\gamma \leq 1000$. As an example, the distribution of it for positive muon in copper is represented in the Figure 2.3 for the given $\beta\gamma$ and muon energy.

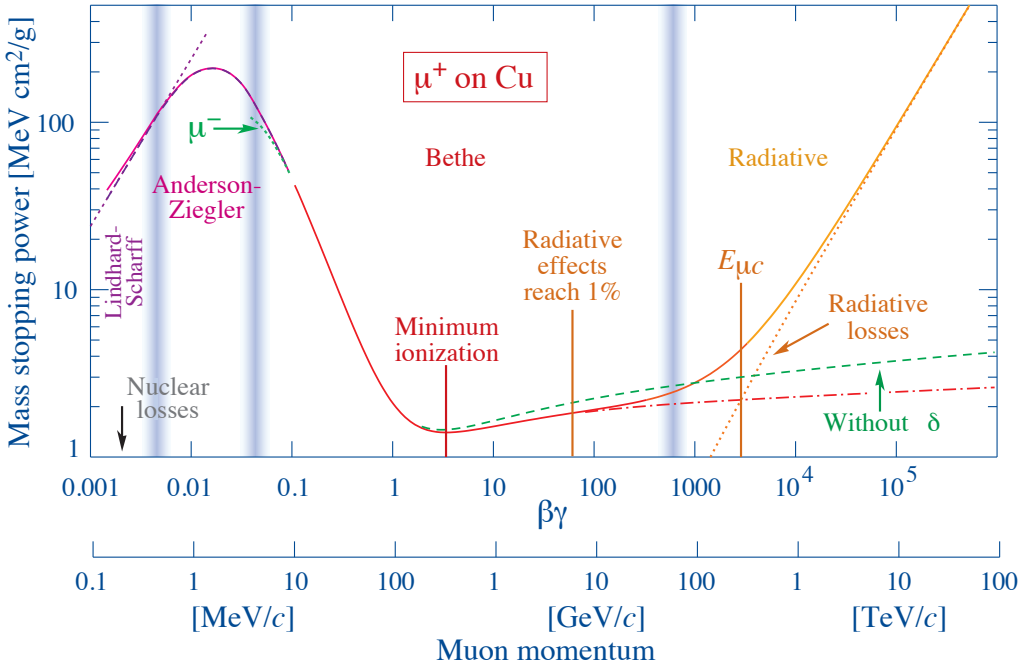

Figure 2.3. The distribution of mass stopping power of copper for positive muon is represented as a function of the given $\beta\gamma$ and muon energy. It is shown in 4 regions for a given range with a solid line. The boundaries of the Bethe-Bloch formula are defined as range $0.1 \leq \beta\gamma \leq 1000$. The graph is taken from (39).

Although the mean energy loss does not directly depend on changes in thickness of material according to the Bethe-Bloch formula, the thickness of the material affects the mean energy loss inside the material and it can be evaluated via the Straggling function derived from Bethe-Bloch formula for a given material thickness at constant particle energy. As shown in Figure 2.4 (a), the Straggling functions for different thicknesses of silicon are obtained with a 500 MeV pion particle. It can be clearly seen that most probably value of values shift from thin to thick, respectively. Also, the distribution behaves like Landau distribution due to the number of interactions within the material. Therefore, the energy loss of a particle cannot be considered as a uniform process for given particle energy and sensor. However, it can be predicted that average electron-hole production for the most probable value of energy deposition. The energy deposition of 3 GeV electrons on silicon which has a 25 μm depth is obtained with GEANT4 simulation and a similar Landau distribution is obtained like in Figure 2.4 (b). The most probable value of Landau distribution obtained from simulation is around 6.27 keV as indicated in Figure 2.4. Using this value, the average number of electron-hole pairs produced in the silicon detector can be calculated by dividing 3.6 eV which is

the required energy for electron-hole pairs production in silicon. As a result, about 1700 electron-hole pairs are produced in silicon with a depth of 25 µm for 3 GeV electrons.

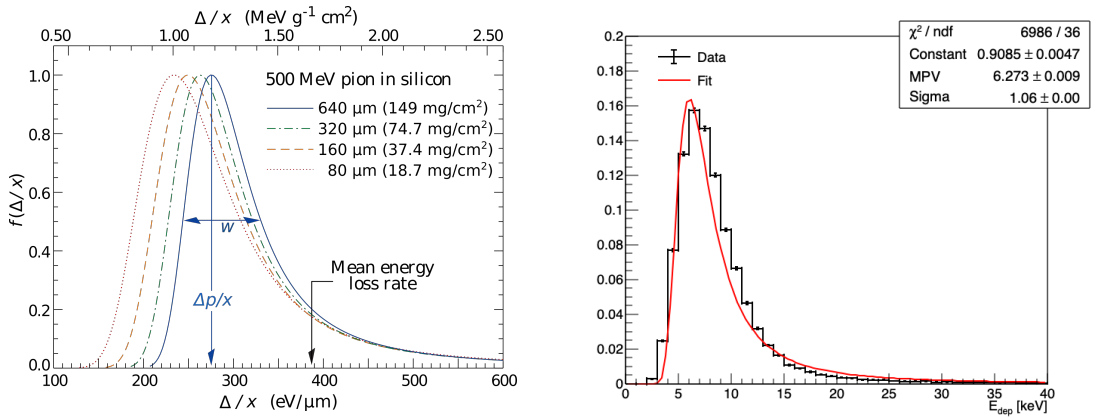

Figure 2.4. (a) The Straggling function plots of various silicon thicknesses are shown for 500 MeV pions. The plot is adopted from (39). (b) The simulation result of energy deposition distribution on silicon with a 25 µm depth for 3 GeV electrons, and applied Landau fit to the distribution are represented with black and red colours, respectively.

In a nutshell, the generated electron-hole pairs can be small or large depending on the energy of particle, thickness of the material, semiconductor material used etc. Apart from these factors, impurity concentration also plays a key role for semiconductor particle detector. All of these factors should be taken into account to design an accurate semiconductor particle detector.

2.3 The p-n Junction

As mentioned, pure silicon is not a perfect semiconductor due to the Fermi energy level at room temperature. Nevertheless, the p-type and n-type extrinsic silicon semiconductors which are rich in terms of acceptor and donor respectively can be used as particle detectors. The p-n junction is the combination of p-type and n-type extrinsic silicon semiconductors as a single body (40). Without applying an external voltage to p-n junction, the electrons start to move towards the p-type region and holes move to the n-type region. The movements of charge carriers create a current inside known as diffusion current. In the middle of the junction, the depletion region is formed by the recombination of the electrons and holes. Due to the exchange of the charge carriers across the depletion region, an electric field

occurs from n-region of the form to p-region. However, there is no electrical flow till the depletion region is in equilibrium. Once the equilibrium is reached, the free charge carriers in the depletion region can move within the p-n junction. One can explain working principle of the p-n junction with mathematical relations starting from the space charge neutrality condition;

$$N_A x_p = N_D x_n \tag{2.4}$$

where concentration of acceptors and donors are represented with N_A and N_B, the depletion region boundaries of the p-side and n-side are shown with x_p and x_n in the equation. From here, charge density distribution of the regions can be written assuming there is only contribution to the net charge, q, in depletion region is ionized charge carriers;

$$\rho(x) = \begin{cases} -qN_A & -x_p < x < 0 \\ qN_D & 0 < x < x_n \end{cases} \tag{2.5}$$

where p-n junction is located at x = 0. The electric field, E, generated inside the depletion region can be calculated by the first Maxwell equation:

$$\frac{dE}{dx} = \frac{\rho(x)}{\varepsilon} \tag{2.6}$$

If charge density is written to the equation and integral of it is taken, the following electric field equations is obtained;

$$E(x) = \begin{cases} \dfrac{-qN_A}{\varepsilon}(x + x_p) & -x_p < x < 0 \\ \dfrac{+qN_D}{\varepsilon}(x - x_n) & 0 < x < x_n \end{cases} \tag{2.7}$$

which is the mathematical representation of the naturally generated electric field inside the depletion region. The second integration of the first Maxwell equation gives the built-in potential generated in the depletion region. It can be written as it follows;

$$V_{built-in} = \frac{q}{2\varepsilon}\left(N_A x_p^2 + N_D x_n^2\right) \tag{2.8}$$

Using the following relation;

$$W \equiv x_p + x_n \tag{2.9}$$

one can also obtain the depletion region width from Eq. 3.9;

$$W = \sqrt{\frac{2\varepsilon}{q}\left(\frac{N_A + N_D}{N_A N_D}\right) V_{built-in}} \tag{2.10}$$

The p-n junction is depicted representing space charge distributions in the depletion region on the top Figure 2.5. The charge density, electric field and built-in voltage distributions that are obtained with the previously explained equations are shown also in the Figure 2.5.

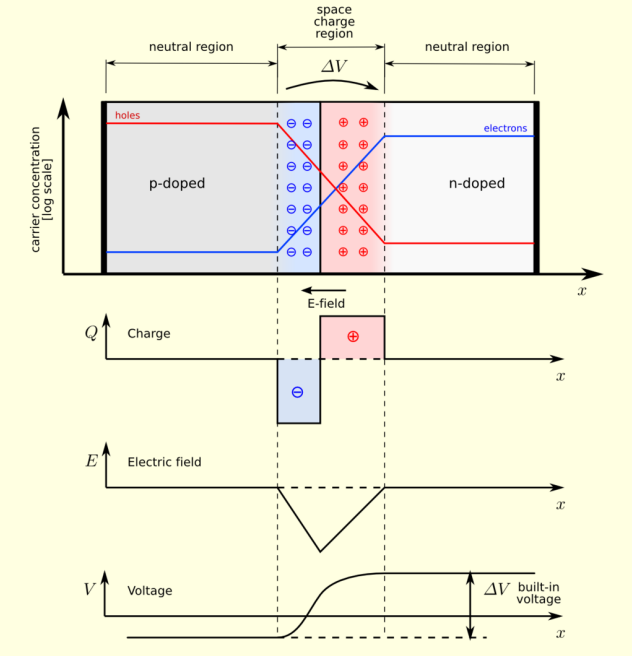

Figure 2.5. From ordering top the bottom, the schematic representation of the p-n junction indicating depletion region, distributions of the charge density, electric field and built-in voltage inside the depletion region. The illustration is taken from (41).

In the depletion region, electron and hole pairs are created when a particle passes through it. Free charge carriers move in the region but produced signal is very slow inside the detector due to the low electrical field inside the p-n junction. Applying an external electric field helps to produce faster signals within the detector. In addition to fast signal production, it directly affects the amplitude of

produced signal inside the detector since more electron and hole pairs are produced in the large width. The depletion region width can be rewritten including externally applied voltage as it follows:

$$W = \sqrt{\frac{2\varepsilon}{e}\left(\frac{N_A+N_D}{N_A N_D}\right)(V_{built-in} + V_{external})} \tag{2.11}$$

As seen in the Eq. 2.11, it depends on two parameters. The first one is the concentration of the donors and acceptors. Hence, high doping levels are generally applied to semiconductor p or n regions to extend the depletion width. Another is the external voltage that increases the width of the depletion region when a reverse bias is applied to the p-n form. These parameters should be well considered in the design of the detector because increment of the doping levels increases the resistivity of the in silicon, which can be depleted at low external voltages.

2.4 Complementary Metal-Oxide Semiconductor (CMOS)

Field-Effect Transistors (FET) are semiconductor electronic devices control current flow by using the electric field (42). It has three terminals as the source, gate and drain. The application of voltage to the gate terminal allows current flow between the other two terminals. Different types of FETs such as Junction Gate Field Effect Transistors (JFETs), Insulated Gate Field Effect Transistors (IGFETs), etc. are currently used in electronic devices. Metal Oxide Semiconductor Field-Effect Transistors (MOSFET) are one of those. It consists of two p-n junctions within the structure and it is controlled by applying low voltage to one of the terminals that allows to current flow. Thanks to this feature, it is used as a bit switch in microelectronic devices. There are two types of MOSFETs based on doping impurities, NMOS and PMOS. The cross-section of NMOS and PMOS transistors are shown in the Figure 2.6. An NMOS transistor is built on a p-type silicon substrate which has three regions known as source and drain that are made of n-type material. In PMOS transistor, the doping polarity of the source, drain and substrate are reversed. As shown in Figure 2.6, drain and source regions are separated by thin insulating oxide layer known as gate oxide. The metal contacts are connected separately to the source, drain and gate oxide regions of the transistors. Current flows from drain to source in NMOS transistor whereas in PMOS it flows from source to drain.

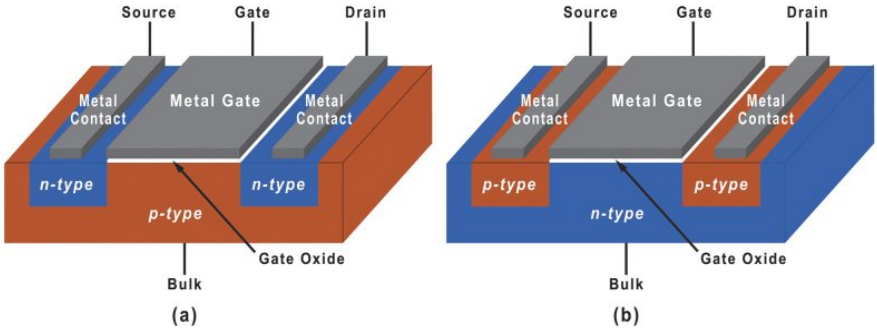

Figure 2.6. Simplified cross section of NMOS (a) and PMOS (b) transistors. The figure is taken from (43).

The simplified working principle of the MOSFET device is explained for NMOS transistor considering Figure 2.6 (a). Assuming the voltage of source terminal as the referenece potential, the gate-source voltage is taken as V_{GS} and drain-source voltage is denoted as V_{DS}. One can let the current flow between drain and source applying voltages to gate. If applied V_{GS} voltage below zero, there is no current flow observed between source and drain as holes populates region under gate. The holes can be repelled increasing V_{GS} voltage to above zero, which creates a depletion region under the gate attracting electrons. Further increase in V_{GS} pulls electrons from the electron-rich source and drain regions to the region below the gate, where it forms a non-permanent electron layer known as inversion layer. As it is understood, large enough V_{GS} voltage behaves like a switch between source to drain. The inversion layer connects the two terminals and allows the flow of electrons from the source to drain when the V_{DS} voltage above zero is applied. These features form the basis of microelectronic applications.

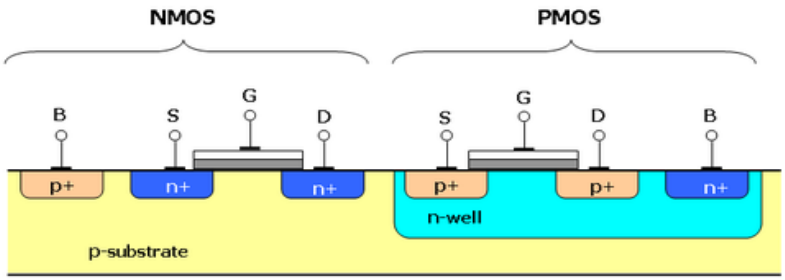

Figure 2.7. Cross section of CMOS device. The figure is adopted from (44).

The Complementary Metal-Oxide Semiconductor (CMOS) forms the basis of microelectronic applications. The CMOS technology consists of embedded

NMOS and PMOS transistors on the same substrate. The main substrate is generally made of p-type silicon and an NMOS transistor is placed on one side of it. An electrically isolated PMOS transistor can be embedded in an n-type silicon by growing an n-well in the p-type bulk. In Figure 2.7, the simplified illustration of the CMOS device is shown. This allows building complex integrated circuits within the silicon wafers, where many NMOS and PMOS transistors can be added as blocks. Therefore, it is good candidate for use in semiconductor particle detector applications considering complicated and expensive bump bonding processes.

2.5 Monolithic Active Pixel Sensors (MAPS)

A typical Monolithic Active Pixel Sensor (MAPS) consists of a p-n junction and the readout electronics within the same silicon chip (45,46). It uses CMOS technology in the readout electronics. A simplified cross-section of the MAPS is shown in Figure 2.8.

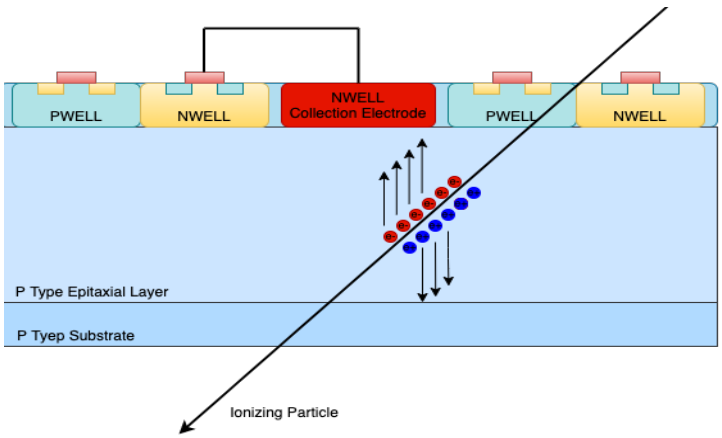

Figure 2.8. Simplified cross section of CMOS particle detector

As can be seen, it is divided into three regions with the n-type collector electrode and reading electronics at the top, the p-type epitaxial layer in the middle and the p-substrate in the bottom. The junction between the collecting electrode and the p-type epitaxial layer is the p-n junction and applying an external potential to the p-n junction creates an additional electric field inside, which extends in the depth of the sensor. Once an ionizing particle passes through the p-n junction, it generates electron-hole pairs in that region. The generated electrons drift or diffuse to collection electrode. As discussed earlier, the number of generated electron-hole pairs depends on the incident particle energy, the thickness of the semiconductor,

depletion width of the junction, applied potential, etc. Therefore, produced signal can be low and is needed to be amplified by charge amplifiers to be used in the CMOS. Besides, the amplified signal is needed to be discriminated and digitized with the integrated circuits. The amplification, discrimination and digitization processes are done on the top of the MAPS, where the complex integrated circuits are formed. Depending on the requirements of the experiment or the radiation environment, the pixel design of MAPS changes. The main changes can be seen in the collection electrode sizes. It is divided into design with small collector electrode and design with large collector electrode. Both designs have advantages and disadvantages. In the following subsections both will be discussed briefly.

2.5.1 Small Collection Electrode MAPS

In the small collection electrode design, the collection electrode is next to the reading electronics and is relatively small in comparison. Due to its size, a small depletion zone forms and a large area of the epitaxial layer remains undepleted. Generated electrons are collected by drift and the signal is sent to the amplifiers within the chip. The Figure 2.9 shows a cross-section of the MAPS small collection electrode design. Main advantage of the small collection electrode design is the low signal-noise ratio and power consumption. With the small electrode design, low capacitance and therefore low noise and faster rise time is achieved. The sensor capacitance is in the order of a few fF and this affects significantly power consumption on amplifier part of the chip. On the other hand, the main challenge is that the design does not allow the full depletion under deep p-well which hosts the readout electronics. One can overcome the problem by extending the depletion region to apply high negative voltage p-type substrate. However, the breakdown voltage of the CMOS transistor junctions is limited and applied voltage cannot be too high. Otherwise, a phenomenon known as punch through occurs in the device. One way to circumvent this problem is to use high-resistance materials in the substrate. This will allow more charge to be collected by the electrode remaining at the lower capacitance increasing the radiation tolerance of the sensor. In addition to using high-resistance materials, the design can be modified with adding low dose n-type implant to overcome with depletion deficiency. In the following chapters, it will be discussed briefly.

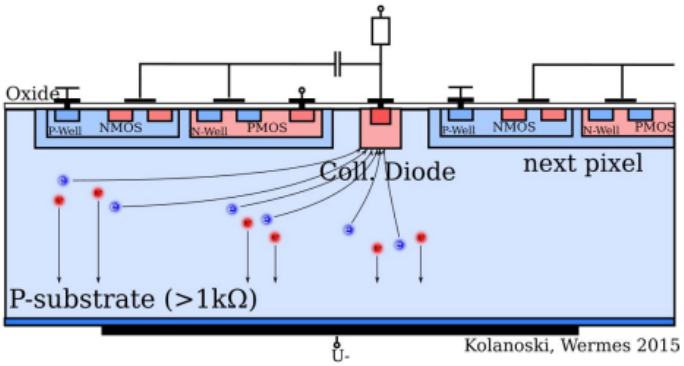

Figure 2.9. Simplified cross section of small collection electrode MAPS. The illustration is taken from (45).

In short, the low noise high granularity pixels can be designed with small collection electrode approach. Thus, the design provides high position and good timing resolution, which makes them good candidates for detecting particle tracks.

2.5.2 Large Collection Electrode MAPS

In the large collection electrode design, the deep n-well collection electrode houses the reading system inside and occupies at least 50% of the pixel area. As a result of its size, it creates a uniform large depletion region within the pixel geometry. The generated electrons are collected by drift and the generated signal is sent to the readout system as done in small collection electrode MAPS. The simplified cross-section of the MAPS large collection electrode design is shown in the Figure 2.10.

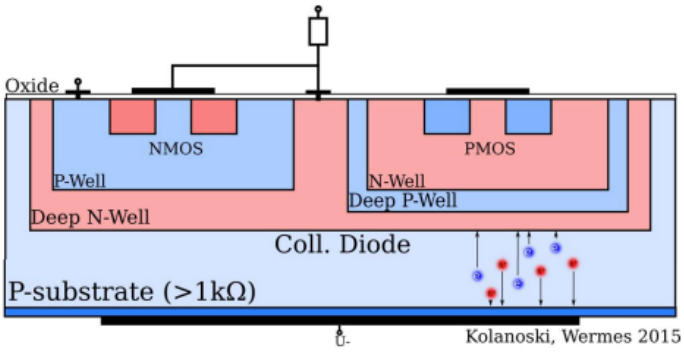

Figure 2.10. Simplified cross section of large collection electrode MAPS. The illustration is taken from (45).

Unlike the small electrode design, a high reverse voltage can be applied to the collection electrode as the readout electronics are embedded in it. This results in a large depletion area inside the pixel that provides fast charge collection and

radiation hardness. Yet, the design has some disadvantages. First of all, the capacitance of the pixel is high due to the intertwining of the readout electronics wells inside the collecting electrode. As seen in Figure 2.10, the NMOS transistor is capacitively coupled to a deep n-well collection electrode. Any logic trigger in the NMOS transistor can lead to generating a fake signal or crosstalk at the collection electrode because of this coupling. Hence, the readout part of the pixel should be designed wisely considering fake signals and crosstalk probability. Second, the large electrode also increases the pixel-to-pixel capacitance within the pixels, resulting in high noise. The capacitance of the pixel is relatively high including readout electronics and it reaches around 100 fF depending on design. Therefore, the usage of thick high-resistance substrates as the sensitive layer is required to reduce the noise effect. Despite the disadvantages of the design, the well-designed large collection of electrodes can be used for detecting particle tracks in radiation hard environments.

2.6 Radiation Damage in Silicon Sensors

The interaction of particles with semiconductor detectors not only results in the generation of electron-hole pairs but is also responsible for damage inside the reading electronics or silicon bulk. The sources of the radiation damage are divided into two groups which are Non-Ionizing Energy Loss (NIEL) and Total Ionizing Dose (TID). Each damage affects the detector differently, for example, TID affects the transistors of the readout system, while NIEL causes defects in the silicon lattice. The source of radiation damage and the effects of radiation damage will be discussed in the following subsections.

2.6.1 Non-Ionizing Energy Loss Effects

The interaction of heavy particles such as protons and neutrons with the silicon can lead to the displacement of the silicon nucleus lattice if the energy is large enough. As a result of the displacements of the silicon nucleus, vacancies and interstitials occur in the lattice. The interstitial is the movement of the silicon nucleus to the non-lattice position. The extent of the damage may seem small, but displacement of one atom can cause the displacement of many atoms, eventually creating a region of disordered silicon atoms known as the cluster defect. The energy of the interacting particle plays a key role in this defect. The minimum

energy required to move the silicon atoms out of the lattice position is 25 eV. Thereby, a proton or a neutron must have an energy of at least 190 eV considering their similar masses. For low mass particles such as electrons, this energy is higher and is around 250 keV. To compare the effects of different particles and energies, 1 MeV neutrons are used as reference particle and therefore the unit of the displacement damage is denoted with neutron equivalent fluence, 1 MeV n_{eq}/cm^2.

Three different defects occur in the silicon lattice due to the displacement of silicon atoms by NIEL. Each one has a different impact on the detection or the operation of the silicon sensor. One of these defects is the creation of new carrier generation centers within the bulk. They are responsible for generating free charge carriers within the space charge region, which ultimately increases the leakage current. Therefore, the amount of radiation exposure increases leakage current within the sensor. The leakage current also depends on temperature. Irradiated sensors should be operated at temperatures as low as $-20^{\circ}C$ or below to reduce leakage current and thermal runaways. In addition, the front end of the sensor needs to be well-designed to prevent the noise rate caused by leakage current.

Another defect is the formation of additional acceptor or donor levels which causes type-inversion. Since the total doping concentration of the sensor is altered by high radiation fluences, the n-type silicon turns into p-type at $\sim 10^{12}$ 1 MeV n_{eq}/cm^2 for low doping concentrations. Hence, this directly affects the depletion region of the sensor and results in an increase in the depletion voltage that must be applied to deplete the sensor. However, the applied voltage may not be sufficient to deplete the sensor in the case of high fluence situations. To overcome this, a p- or n-type collection electrode is placed inside the highly n-doped silicon, allowing depletion of the sensor even if type-inversion occurs.

The last one is the charge traps that occurred within the bulk. The charge carriers generated inside the sensor are collected by the collecting electrode as mentioned earlier. Some of them cannot be collected by the collection electrode and be trapped due to displaced atoms in the lattice. Displaced atoms create a shallow bandgaps and charge carriers are trapped in these band gaps for a limited duration. As a result of this event, the amount of the collected charge decreases because the charges are generally collected by drift. Since the drift depends on the mean lifetime of the charge carriers, the drift paths should be kept short. Thereby, even if the charge carriers are trapped for a limited time, they are collected by the collecting

electrode. Moreover, the threshold of the readout should be tuned after irradiation to cope with low signal amplitude and leakage current.

2.6.2 Total Ionizing Dose Effects

As mentioned in the working principle of semiconductor detectors, charge carriers are generated inside the bulk as a result of ionization when high energy charged particle passes through the detector. After that, generated charges drift or diffuse through the collection electrode and the readout process starts within the front-end of the device. However, these charge carriers can be also generated inside the front-end electronics. The front end consists of MOS transistors where the channels of the transistors is typically separated by an insulating layer, SiO_2, as discussed in the previous subsections. The total ionizing dose is responsible for the generation of charge carriers within the insulating layer of MOS transistors that cause damage to the readout electronics. It is measured by Gray (Gy) in the SI unit system and 1 Gy is the absorption of 1 Joule of energy per kg of matter. However, sometimes can be represented in rad (Radiation Absorbed Dose) in literature and 1 Gy is equal to 100 rad.

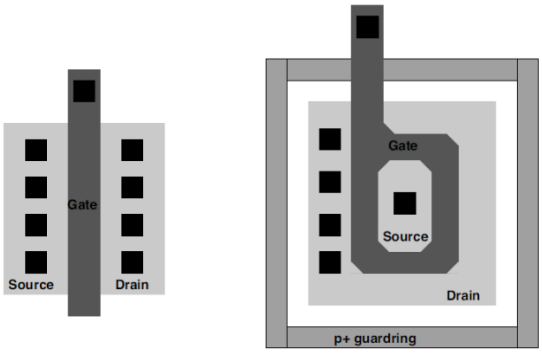

Figure 2.11. STI (left) and ELT (right) layout of the MOS transistors

The generated charge carriers in the SiO_2 have a large mean lifetime compared to the silicon bulk. Besides, the mobility of electrons is higher than the holes. Therefore, holes are trapped and form positive charges in the insulating layer. As a result, a leakage current between the source and the drain of a transistor increases and the electrical behaviour of the device changes turning the logic state. In order to make more tolerant transistors to the TID effect, a thin layer of insulation must be considered as the number of trapped holes is reduced. Moreover, the design of the isolation layer has importance. Shallow trench isolations (STI) design is more

vulnerable to TID. However, Enclosed Layout Transistor (ELT) is a more radiation tolerant transistor design for the TID. In this design, current from source to drain flows under the circular gate suppressing leakage current. The design also has a p^+ guard ring to isolate two different areas of silicon. Both layouts of the transistors are shown in Figure 2.11.

Ionizing radiation can also cause instantaneous effects known as Single Event Effects (SEE) by triggering several mechanisms in the readout electronics. Single Event Upset (SEU), Single Event Latch-up (SEL), and Single Event Transient (SET) are the most likely. A Single Event Upset (SEU) is a change of state in a sensitive node by the ionized carriers. The sensitive node is a logic element of the device and is referred to as a bit. The bit flip can variously effect like corruption of data, misconfiguration of devices. Single Event Latch-up (SEL) occurs in the thyristor structure of MOSFET which consists of parasitic p-n-p and n-p-n structures. The thyristor structure is designed to work in harmony, the p-n-p structure is activated while the n-p-n is disabled. However, the high energy charged particle can create a path between the power supply of rails of thyristor elements and disrupts the working harmony between elements. The device can become inoperable due to overcurrent if the issue is not recognized. Transient voltage disturbance on the transistor structure can also cause the Single Event Transient (SET) effect in the case of high energetic particle interaction in the transistors. As a consequence of the SET, data or system timing requirements are affected like in SEU.

3. THE TOWER SEMICONDUCTOR MALTA SENSORS

The ATLAS experiment is planning a major renovation of the detector components to prepare for the High Luminosity LHC era. This includes an increase in the detector coverage planned for the discovery of new physics. However, as expected, the increment of the luminosity becomes demanding for the detector components in terms of the radiation hardness. The Inner Tracker (ITk) detector of the ATLAS experiment must fulfil the requirements of the harsh radiation environment in the HL-LHC (47). Hence, the ATLAS collaboration launched a dedicated research and development projects on the radiation hard pixel detectors. One of them, MALTA, is radiation-resistant CMOS monolithic pixel sensor which was designed to be used in the outermost layer of ITk (1.5×10^{15} 1 MeV n_{eq}/cm^2 and 60 MRad for NIEL and TID, respectively). MALTA is a small collection electrode MAPS developed in Tower Semiconductor 180 nm CMOS imaging technology. The MALTA sensor spin-off the R&D of the ALICE Inner Tracking System (ITS) upgrade (48) that uses the ALPIDE sensor and therefore, the MALTA name stands for Monolithic pixel detector from ALICE to ATLAS. The MALTA sensor is still under R&D process and continues to develop from simulations, laboratory measurements and test beam results.

In this section of the thesis, the properties of the MALTA sensors will be detailed introducing pixel design, pixel front-end design and pixel matrix. The development process of MALTA sensors also will be given in the subsection of the section.

3.1 MALTA Sensor

The pixel of the MALTA sensor is designed with a small collection electrode to achieve a small sensor capacitance and low power consumption. Its predecessor, the ALPIDE sensor (49), was produced with a standard Tower Semiconductor 180 nm process (50) is shown in Figure 4.1. In the standard process, a high-resistivity p-type 25-30 μm thick epitaxial layer which has a resistivity of above 1 kΩ·cm is used to enlarge the depletion around the collection electrode. Pixel can be operated by applying a reverse bias of up to 6 V to the p-type substrate of the sensor. The bias voltage applied is limited due to the punch-through that

occurs around 8 V as the NMOS transistors in the readout electronics see the same reverse voltage.

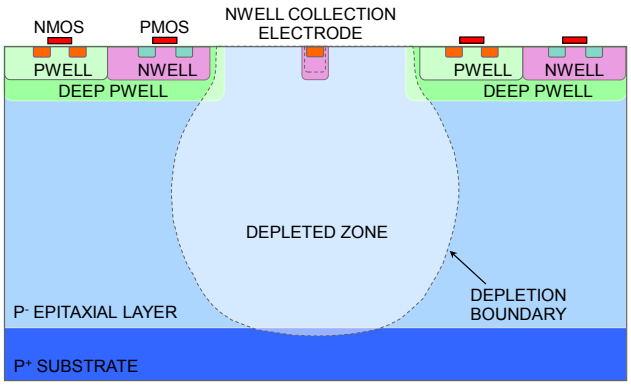

Figure 3.1. Cross-section of the small collection electrode ALPIDE pixel which is 180 nm Tower Semiconductor standard process (51).

As it can be seen in the Figure 3.1, the depletion region is limited and the pixel edges stay undepleted. The charges which are generated outside of the depleted area can be collected by diffusion if the NIEL of the environment is below 10^{13} 1 MeV n_{eq}/cm^2. This is the required radiation tolerance for ITS of the ALICE experiment (48,49). Exceeding the radiation limit prevents the diffusion process for the undepleted region resulting in poor tracking performance. Therefore, the standard process of the ALPIDE pixel has to be modified in the pixel design process of MALTA.

3.1.1 Pixel Design

The standard Tower Semiconductor manufacturing process was modified with an additional low-dose n-type implant below the wells containing readout circuitry to achieve full lateral depletion. With this modification, the radiation hardness of the MALTA pixel is aimed to meet HL-LHC limits (47). The cross-section of the MALTA pixel with modified process is shown in Figure 3.2. In the modified process, the thick p^- epitaxial layer (25-30 µm) and the low dose n^-type implant are fully depleted at low reverse bias voltages that also can be increased up to 20 V without punch-through. Biasing such bias voltages allows the increases the strength of electric field lines and that results in faster charge collection. Since the collection electrodes in the pixel matrix are isolated, the capacitance of the pixel does not change due to modification and it stays ~2 fF. This reduces the input

capacitance and leads to low power consumption which is the order of 1 µW/pixel and 70 mW/cm^2.

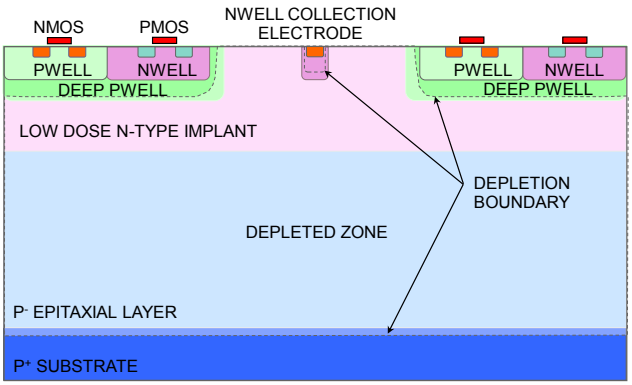

Figure 3.2. Cross-section of the small collection electrode MALTA pixel which is 180 nm Tower Semiconductor modified process (51).

3.1.2 Pixel Matrix

In order to test the modified process, the Investigator (52) chip which contains 8 × 8 pixels was produced in Tower Semiconductor 180 nm CMOS imaging technology. Obtained test beam results and laboratory measurements of Investigator chip were promising enough to produce large MALTA prototype. The large prototype of the MALTA chip matrix consists of 512 × 512 pixels with 36.4 µm pitch size and the total detection area of pixel matrix is 2 × 2 cm^2. The pixel matrix of the sensor is divided into 8 different sectors. Each sector has different pixel flavours and pre-amplifier designs in the front-end as indicated in Figure 3.3.

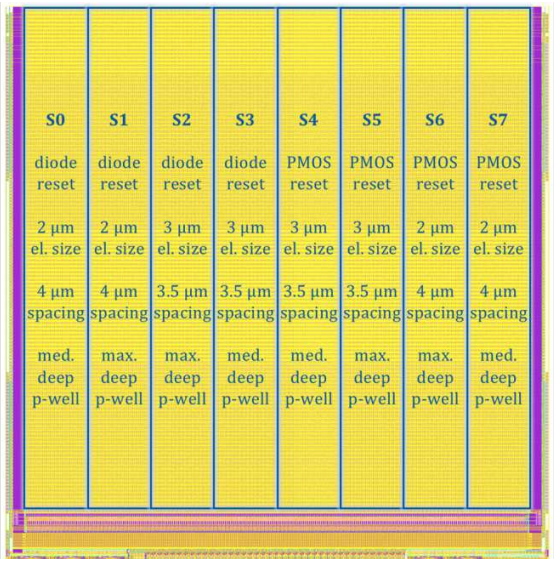

Figure 3.3. Representation of the MALTA pixel matrix indicating the pixel flavours of 8 different sectors (51)

There are three different strategies used in the design of the pixel flavours. The first one is the size of octagonal collection electrode which varies from 2 to 3 μm. Another one is the separation between the collection electrode and the deep p-well containers of the readout electronics. Two different separation options, 3 and 4 μm, are used in the pixel flavour designs. The last difference is the deep p-well coverage that is required for n-wells of the PMOS elements. Medium and maximum deep p-well options are considered in the design of the pixel flavours. In the medium deep p-well option, the p-well is removed from areas with NMOS transistors, while in the maximum deep p-well arrangement, all transistors are covered with a deep p-well. In Table 3.1, the pixel properties of the MALTA sector are listed with respect to the electrode reset, electrode spacing, electrode size and deep p-well extension.

Table 3.1. The pixel flavours of 8 different sectors

Sector	Reset	Electrode Size	Electrode Spacing	Deep p-well Extension
S0	Diode	2 μm	4.0 μm	Medium
S1	Diode	2 μm	4.0 μm	Maximum
S2	Diode	3 μm	3.5 μm	Maximum
S3	Diode	3 μm	3.5 μm	Medium
S4	PMOS	3 μm	3.5 μm	Medium
S5	PMOS	3 μm	3.5 μm	Maximum
S6	PMOS	2 μm	4.0 μm	Maximum
S7	PMOS	2 μm	4.0 μm	Medium

3.1.3 Analogue Front-End

The front-end of the MALTA sensor contains analogue and digital circuities. The analogue part consists of a fast charge amplifier, a signal shape amplifier and a simple discriminator circuits, while the digital part possesses the logic circuits to readout that pixel. The spacing between the collection electrode and the front-end circuitry can be 3.5 or 4 μm depending on the sectors as listed in Table 3.1. To avoid crosstalk between pixel readings, these two, analogue and digital zones, are separated and protected by metals. The layout of a pixel is shown in Figure 3.4, representing analogue and digital circuits with blue and red colours respectively.

The collection electrode is the input node of the front-end and is connected to a continuously active reset circuit. The reset circuit transmits the collected charge

as an input signal to an amplifier. Two different reset mechanisms are used in the MALTA sectors separately. In Figure 3.5, diode and PMOS reset circuits are shown. Both have their pros and cons. For example, the implementation of the diode reset circuit is simple and has a low capacitance that cannot be reset at low charge generation. On the other hand, PMOS reset allow to work with low charge collection but it takes up more space and it has large capacitance.

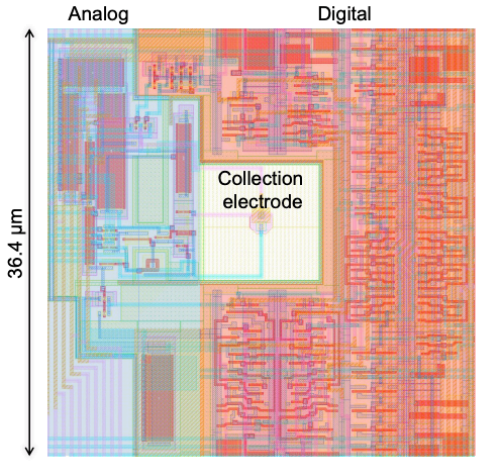

Figure 3.4. The layout of a MALTA pixel. The analogue and the digital circuits are represented with blue and red colours respectively. The picture is taken from (51).

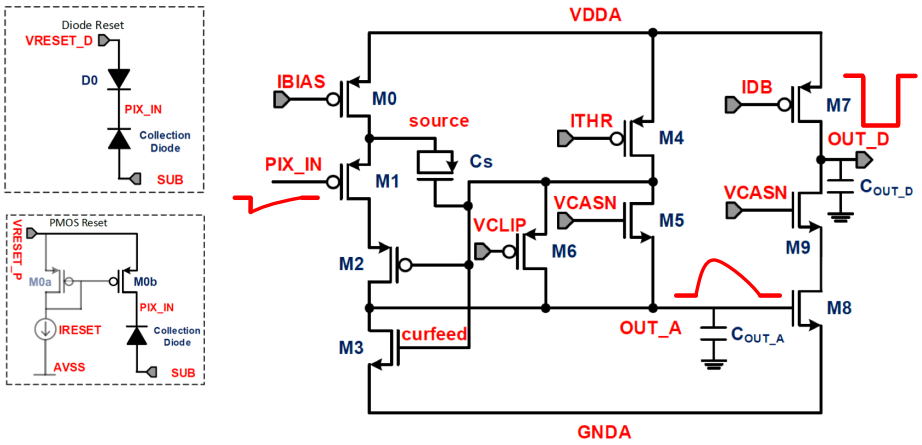

Figure 3.5. Diode reset and PMOS reset circuits of the MALTA sensor are shown on left top and on left bottom, respectively. The analogue front-end circuit of the sensor and stages of collected charge pointing out PIX_IN (pixel input of signal), OUT_A (amplifier output of signal) and OUT_D (discriminator output of signal) are shown on the right. The circuit diagrams are taken from (51).

In Figure 3.5, the analogue front-end circuit of the MALTA sensor is illustrated showing stages of the signal. The analogue front-end design of the ALPIDE sensor has been modified to operate in the low-threshold configuration of

the MALTA sensor, such as 200 electrons (e^-). Considering the 25 μm thick sensitive area of the sensor, the maximum produced charge by a minimum ionizing particle is around 1700 e^- for the most probable value of the Landau distribution. The maximum amplitude of the signal is around 50 mV since the capacitance of the collection electrode is in the order of a few fFs. Therefore, the signal needs to be amplified by the open-loop voltage amplifier. In the design, the circuit is biased by 7-bit DACs transistors, M0, M4 and M7, to control the distribution of voltage and current of the front-end. While M0, labelled as IBIAS, controls the baseline shift of the signal, M4, is ITHR, controls the return to the baseline of the signal. The transistor M7 which represented as IDB controls the threshold voltage. All of these transistors allow altering the gain of the circuit in other words it is controlling mechanism for the threshold of the sensor. In the last stage of the analogue front-end, the signal is discriminated by transistors and trigger transmitted to in-pixel logic. This was the first analogue front-end design of the MALTA sensor, which was later modified by enlarging certain transistors in mini-MALTA. Later, the design was improved by adding an additional cascode transistor between M2 and M3 that controls the return to the baseline which makes M3 less relevant in the threshold and noise contribution. These updates in the front-end will be discussed in the following sections with showing threshold and noise measurements.

3.1.4 Asynchronous Digital Matrix Readout

The MALTA chip uses an asynchronous digital readout architecture (53) where the pixels are organized in groups of 2 pixels columns (double columns) and 8 pixels rows as shown in Figure 3.6. The readout architecture works without clock propagation to decrease power consumption. Any signal out that comes from the discriminator (OUT_D in Figure 3.5) activates a reference signal inside the group which is used to collect the signals in any of the pixels of the group in a 2 ns window, and is used as the clock signal at the end-of-column logic. There are two independent buses that serve pixel groups separated even or odd. The pulses are distributed using these 22-bit wide buses which include reference bit, 16-bit pixel address and 5-bit encoded group address.

As can be seen in Figure 3.6, non-neighbouring groups share same bus. This avoids the overlap of signals at the periphery that occurs in the case of charge sharing between neighboring groups. Since double-columns are independent, data

can be transmitted without any time difference for hit observation on the different pixel locations at the same time. This means that up to 16 hits can be transmitted out of the pixel group in single at once. At the end of the process, the two busses are merged in a single bus adding an extra bit to indicate the group parity is even or odd. Then, the three bits Delay Count, eight bits double column ID, two bits Bunch Crossing ID (BCID) and four bits chip ID are included in the MALTA output word. While the Delay Count bits represent the arrival time information of the hit to the periphery, the double column ID bits are associated with the double column ID of the hit in that pixel group. The BCID bits represent the Bunch Crossing Trigger inputs from the sync memories created using a 40 MHz external clock. Lastly, the chip ID bits store the identification MALTA sensor. The MALTA output word is listed in Table 3.2.

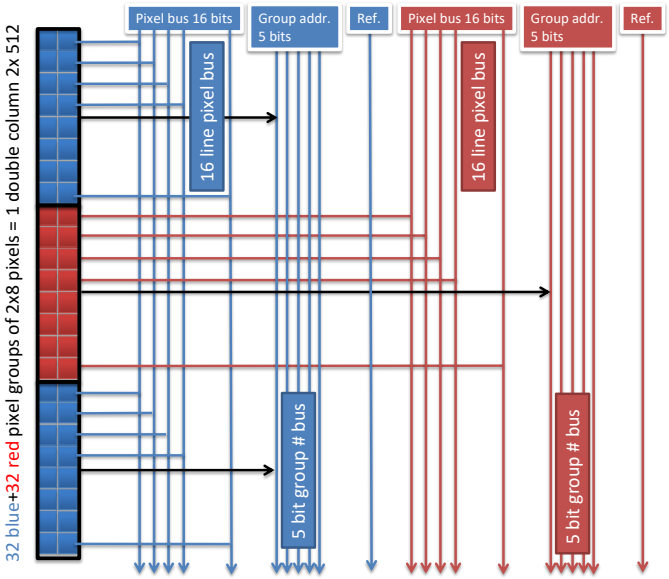

Figure 3.6. Schema of asynchronous readout architecture and illustration is taken from (54).

Table 3.2. Bit Descriptions of the MALTA output word

Bit ID	Content
0	Reference
1-16	Pixel Address
17-21	Group Address
22	Group Identifier (red or blue)
23:25	Delay Count
26:33	Double Column ID
34:35	Bunch Crossing ID
36:39	Chip ID

3.1.5 The MALTA Readout System

The MALTA chip is wire-bonded on a high density 10-layer PCB carrier board to interface with it. The chip is powered by external power supply sources. There is a 1 × 1 cm^2 square hole where the sensor sits, and conductive glue is used on the back of the sensor before the bonding process. The chip is attached to the carrier plate with up to 700 aluminium wedge bonds. The analogue and digital grounds of the chip are connected to the reference 0 V of the PCB which is externally supplied to avoid floating voltages. The MALTA carrier board and the aluminium wedge bonds are shown in Figure 3.8.

The data is asynchronously transmitted in parallel to the output pads with a low voltage differential signal (LVDS) and transmitted to an evaluation board, Xilinx 7-series Virtex VC707 or Kintex KC705, for further processing via the FMC connector (55). A dedicated firmware stores the data in a First In First Out memory (FIFO) on the FPGA with a 390 ps time stamp which is later read-out via an Ethernet connection through C++ using IPbus protocol (56).

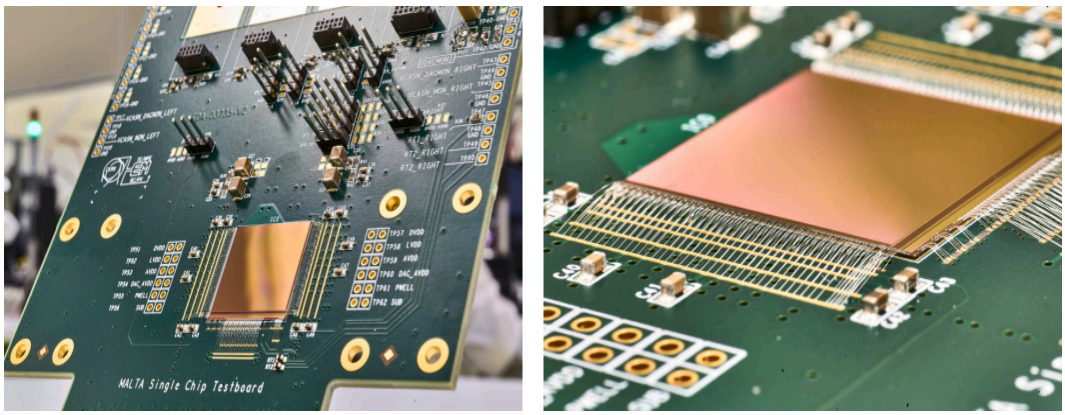

Figure 3.7. The MALTA carrier board and the aluminium wedge bonds

3.1.6 Laboratory Measurements and Test Beam Results

In order to do the characterization test and determine the effects of radiation damage to samples, some laboratory measurements were performed before the the test beam measurements. The performed laboratory measurements such as the Fe^{55} source spectra, threshold and noise distributions of MALTA sensors were obtained and reported in the references(51,53,57–66). In here, the threshold and noise measurements will be summarized the for the irradiated and non-irradiated samples since they are directly effects the tracking efficiency. During the threshold and noise measurements, two sectors of the pixel matrix, S2 and S3 (see Table 3.1), were

focused on and the measurements were performed inside a climate chamber at −20°C.

The threshold of a pixel is measured by injecting a controlled charge. The charge is produced in a circuit known as a charge injection circuit and is directly connected to the collection electrode of the pixel. Each pixel has its own charge injection circuit and uses the test capacitance in the circuit to send pulses with a certain amount of charge to the pixel. The charge amount can be controlled by increasing or decreasing the applied voltage to the charge injection circuit. To measure the threshold of a pixel, a fixed number of pulses is sent to the pixel by increasing the charge amount by the means of increasing applied voltage to charge injection circuitry. Then, the output signal from the analogue front-end of the pixel is counted to determine saturation with respect to the number of pulses for a given charge. Once the taken data is fitted with a Gaussian error function as it follows;

$$\mathrm{f}(x|N,\mu,\sigma) = \frac{N}{2}\left(1 + Erf\left(\frac{x-\mu}{\sqrt{2}\sigma}\right)\right) \tag{3.1}$$

where N represents number of pulses sent to chip, μ and σ values correspond to the threshold and noise of the measured pixel, respectively. The threshold scan of a pixel on MALTA is shown in Figure 3.8.

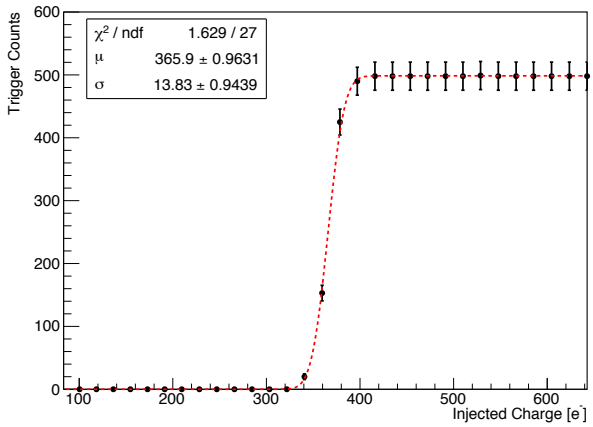

Figure 3.8. Threshold scan of a MALTA pixel and applied fit of Gaussian error function which calculates the threshold μ = 365.9 e^- and noise σ = 13.83 e^-.

In a similar way, the statistically sufficient amount of pixel was scanned and obtained threshold and noise distributions of the non-irradiated MALTA sample are shown in Figure 3.9. There is nearly 30 e^- difference in the threshold for the same

settings between the two sectors due to the medium and maximum deep p-well approach that affects the input capacitance of pixels. Also, the threshold distribution of both sectors has an RMS value of around 37 e^-. This is pretty high to operate a pixel whose threshold is below 200 e^- because that pixels with lower thresholds cause increase the noise rate. On the other hand, although the noise distribution is expected to be a Gaussian distribution, it has a long tail distribution as shown in Figure 3.9. The phenomenon is known as Random Telegraphic Signal (RTS) noise usually occurs in the MOS transistors because of the trapped electrons and it causes the long-tailed noise distribution. In addition, the contribution of RTS noise increases with radiation damage. One of the transistors (M3) in charge of the feedback loop in the analogue front-end (see Figure 3.5) may be responsible in the RTS noise contribution.

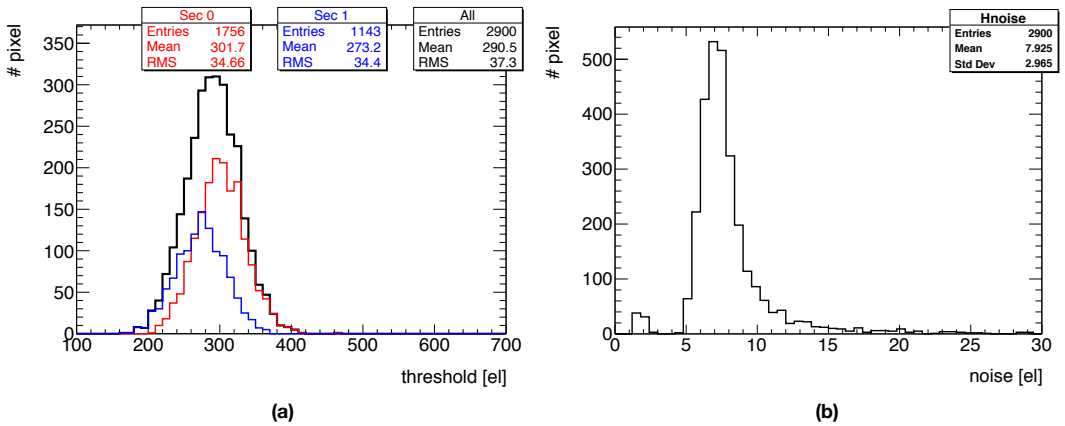

Figure 3.9. (a) The obtained threshold distribution of the non-irradiated sample is shown for Sector 2 (Sec 1 in the figure) and Sector 3 (Sec 2 in the figure) representing with red and blue colour lines respectively. The black line is the combination of two sectors (Sec 1 + Sec 2) to show mean threshold value of sample. (b) The noise distribution of the Sector 2 and Sector 3 are shown in one distribution. The plots are adopted from (51).

In Figure 3.10, the threshold and noise scan distributions of the MALTA sample irradiated with x-ray up to 70 Mrad are shown. There is nearly 45% increase in threshold dispersion and threshold difference of two sectors was not disappeared on the contrary is doubled reaching 60 e^-. In the previous chapter, TID effects on the readout electronics were discussed and it is expected to be increase the noise generated within front-end. As seen in Figure 3.10, mean value of the noise distribution increases to 17 e^- and tail related with RTS still remains. Therefore, sensor cannot be operated in low threshold configurations due to high noise contribution from the in-pixel readout electronics.

The threshold and noise distributions were also obtained for sample irradiated with neutron up to 5×10^{14} 1 MeV n_{eq}/cm^2. As shown in Figure 3.11, the threshold of the pixels has wide distribution and the dispersion is two times larger values than un-irradiated sample results reaching around 70 e^- for both sectors. This makes chip impossible to operate at low below threshold such as below 200 e^- after neutron irradiation when the noise rate contribution is also taken into account. The mean value of noise distribution is around 12 e^- after neutron irradiation and tail related with RTS noise still can be seen in Figure 3.11(b).

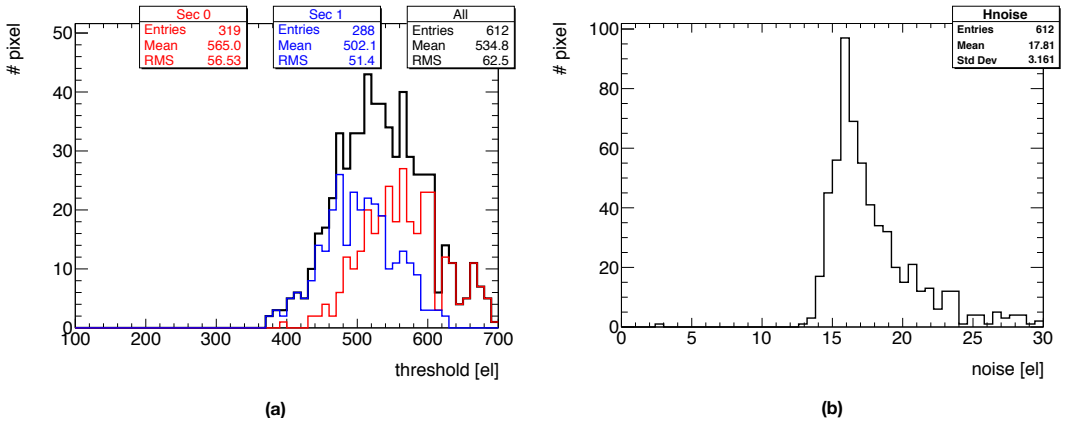

Figure 3.10. (a) The threshold distribution of the irradiated sample with X-ray up to 70 MRad dose is shown for Sector 2 (Sec 1 in the figure) and Sector 3 (Sec 2 in the figure) representing with red and blue colour line respectively. The black line is the combination of two sectors (Sec 1 + Sec 2) to show mean threshold value of sample. (b) The noise distribution of the Sector 2 and Sector 3 are shown as one distribution. The plots are reproduced from (63).

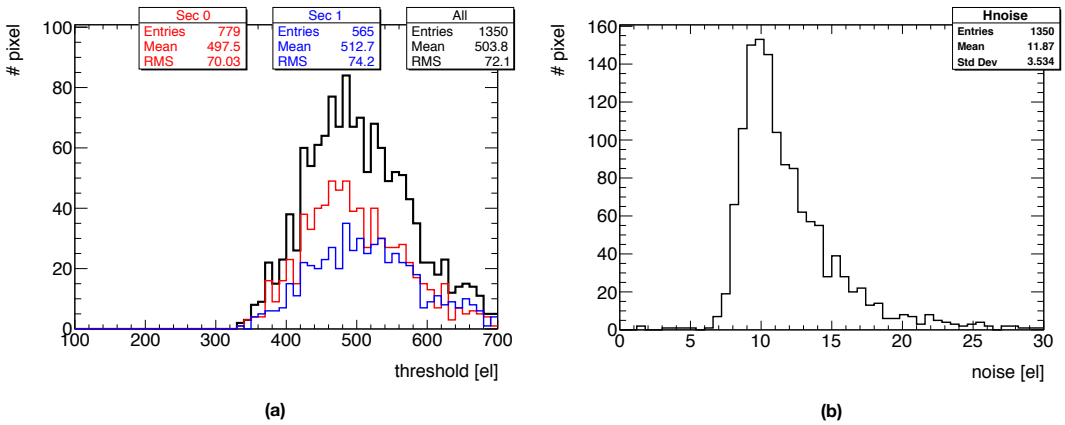

Figure 3.11. (a) The threshold distribution of the irradiated sample with neutron up to 1.5×10^{15} 1 MeV n_{eq}/cm^2 dose is shown for Sector 2 (Sec 1 in the figure) and Sector 3 (Sec 2 in the figure) representing with red and blue colour line respectively. The black line is the combination of two sectors (Sec 1 + Sec 2) to show mean threshold value of sample. (b) The noise distribution of the Sector 2 and Sector 3 are shown as one distribution. The plots are taken from (63).

After the laboratory measurements, the MALTA samples were tested under a 180 GeV pion beam at SPS CERN to determine tracking efficiency performance. During the test beam, MALTA samples were placed in a MIMOSA telescope which consists of 6 MIMOSA-26 pixel detectors (67) as a Device Under Test (DUT). Recorded hits from telescope planes and the DUT were used to build tracks via the Proteus framework (68) so that the pixel efficiency and cluster sizes could be determined on the MALTA sensors. During the test beam, the MALTA samples were kept at −20°C to avoid leakage current related to thermal runaways. To deplete MALTA samples fully without any leakage, the substrate was biased to −15 V while the p-well was biased to −6 V. Test beam in-pixel results of unirradiated and irradiated samples are shown with 2 × 2 pixel matrix maps from Sector 4. The results were obtained for hit efficiency and cluster size that indicates the charge sharing between pixels. Since the threshold of the pixels has an impact on the hit efficiency and cluster size, the results were obtained for 3 different threshold configurations, low, medium and high. Figure 3.12 shows the hit efficiency maps of the unirradiated MALTA sample. In the low threshold, the efficiency is above 90% for the whole pixel. However, when the threshold value is increased, the efficiency of the entire pixel drops and is above 85% only for around the center of the pixel.

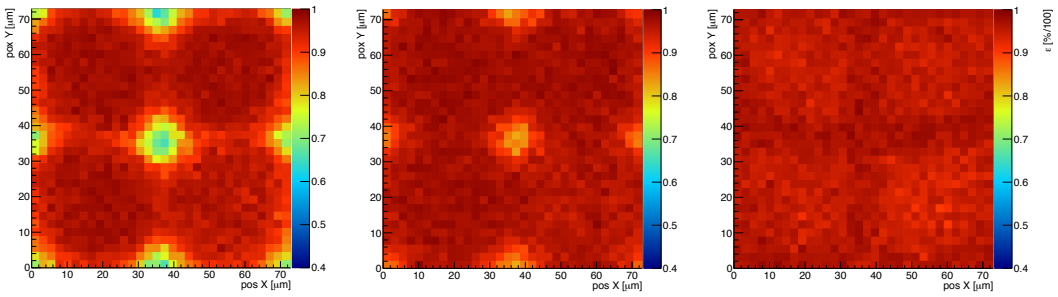

Figure 3.12. Hit efficiency maps of the non-irradiated MALTA 2 × 2 pixel matrix of Sector 3 is shown from left to right for different thresholds of 470 e^-, 400 e^- and 210 e^-. The figures are taken from (57).

As discussed earlier, the charge generated by the minimum ionizing particle is around 1700 e^- in the sensitive area of 25 µm of the sensor, and if the particle hits the corner of one of the pixels, the generated charges are shared by other 3 pixels. In the case like the threshold is around 450 e^-, the collected charge cannot exceed the threshold and it cannot be sent to the readout circuits. Therefore, efficiency on

the corners drops to around 50% at the high threshold applied due to charge sharing between pixels. The situation can be seen clearly in cluster size maps of the pixels as shown in Figure 3.13. At the low threshold 210 e^-, while cluster size is around 1.2 in the center of the pixel where the collecting electrode is located, it reaches around 2.5 at the edges of the pixels. This explains the reason for the drop in the hit efficiency especially when looking at the cluster size maps obtained with a high threshold of 470 e^-. Whereas the cluster size is around 1.2 at the pixel center, it is only around 1.6 at the corner of the pixels.

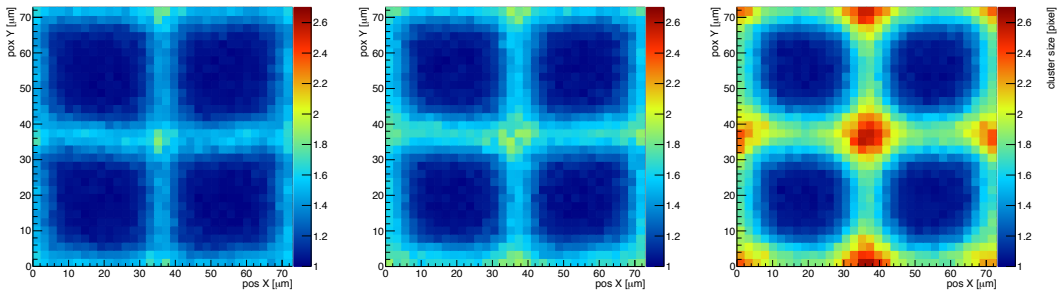

Figure 3.13. Cluster size maps of the non-irradiated MALTA 2 × 2 pixel matrix of Sector 3 is shown from left to right for different thresholds of 470 e^-, 400 e^- and 210 e^-. The figures are taken from (57).

The same test was done for the samples irradiated with 5×10^{14} 1 MeV n_{eq}/cm^2. Again, the results of the 2x2 pixel matrix maps from Sector 4 were focused to make a comparison. However, two different threshold values, 600 e^- and 400 e^-, could be used in the results due to the high noise rate in the 200 e- threshold configuration. The Figure 3.14 shows the hit efficiency maps of the irradiated MALTA sample. As it can be seen, the efficiency is only above 80% at the center of the pixel without any difference in the threshold. The efficiency drops aroud 30% to 10% at the corners with an increment of threshold. Due to the noise related to the radiation damage, the hit efficiency of the pixel decreases in the corners and the chip was not able to operate in the low threshold (around 200 e^-) configurations, unlike the un-irradiated sample. When cluster size maps were taken into account, it is 1.0 at the pixel center and increases by 1.2 for and even 1.4 depending on the threshold at the corners of the pixel as seen in the Figure 3.15. Despite to high threshold configuration, the cluster size is very low considering the un-irradiated samples. This is directly related to the deficiency caused by NIEL. The depletion region is limited to the pixel center resulting in the low electric field formation at the edges

of the pixel and generated charges cannot be drifted through the collection electrode. Due to high threshold configuration, the cluster size is very low considering the un-irradiated samples. This is directly related to the deficiency caused by NIEL. The depletion region is limited to the pixel center resulting in the low electric field formation at the edges of the pixel. Therefore, generated charges cannot be drifted through the collection electrode.

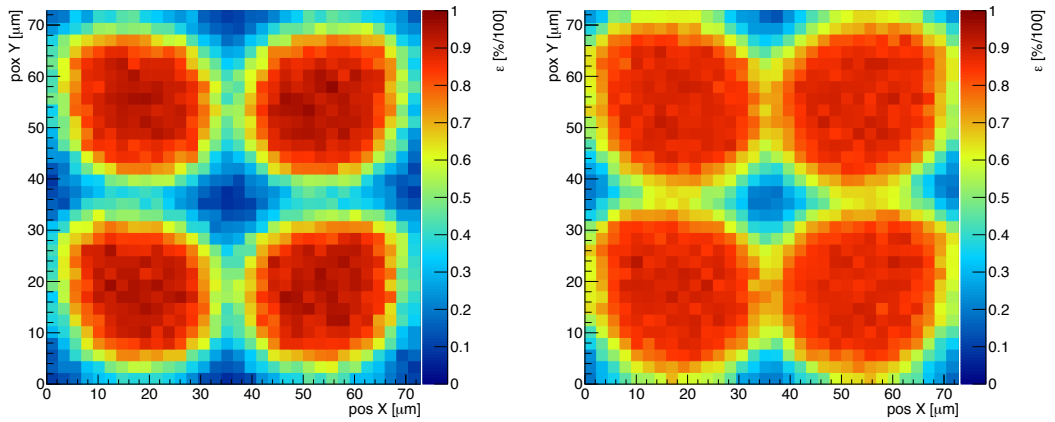

Figure 3.14. Hit maps of the 2 × 2 pixel matrix of Sector 3 after 5×10^{14} 1 MeV n_{eq}/cm^2 neutron irradiation are shown on the left and right side for different thresholds of 600 e^- and 400 e^-. The figures are taken from (57).

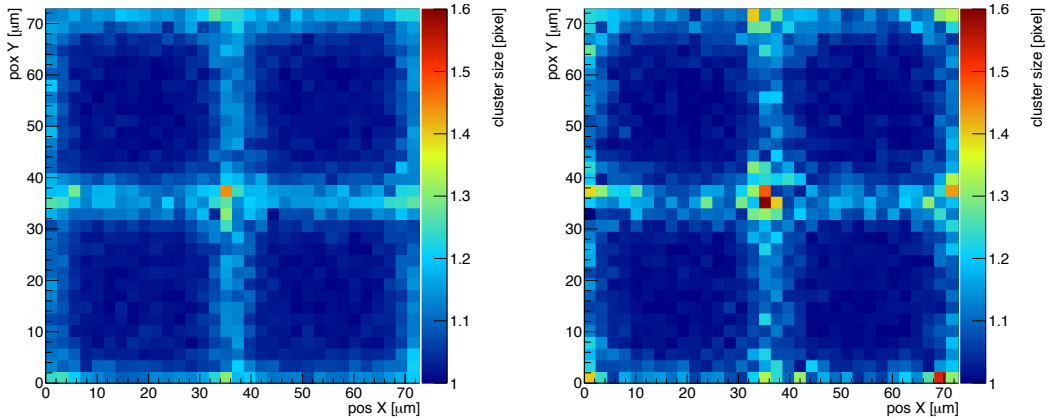

Figure 3.15. Cluster size maps of the 2 × 2 pixel matrix of Sector 3 after 5×10^{14} 1 MeV n_{eq}/cm^2 neutron irradiation are shown on the left and right side for different thresholds of 600 e^- and 400 e^-. The figures are taken from (57).

On the other hand, an effect is also seen in the event maps formed at the pixel edges when looking at the efficiency plots. The expected hit efficiency should be distributed in a round shape decreasing from the center of the pixel to the edges. However, hit efficiency is not in a round shape it has special pattern. Once the hit

efficiency of other sectors is obtained, it is well understood that it is related to medium and maximum deep p-well arrangement in pixel design. As a reminder, while the p-well is removed from the fields below the NMOS transistors in the medium-deep p-well design, while in the maximum deep p-well arrangement, all transistors are covered with a deep p-well. In Figure 3.16, the pixel design that has the medium and maximum deep p-well arrangement on the top and the hit efficiencies of those pixels are shown at the bottom respectively. As can be seen in the efficiency maps of the Figure 3.16, the pattern overlaps with the design. One can conclude this behaviour, the bigger the p-well cut-out the better the charge collection efficiency.

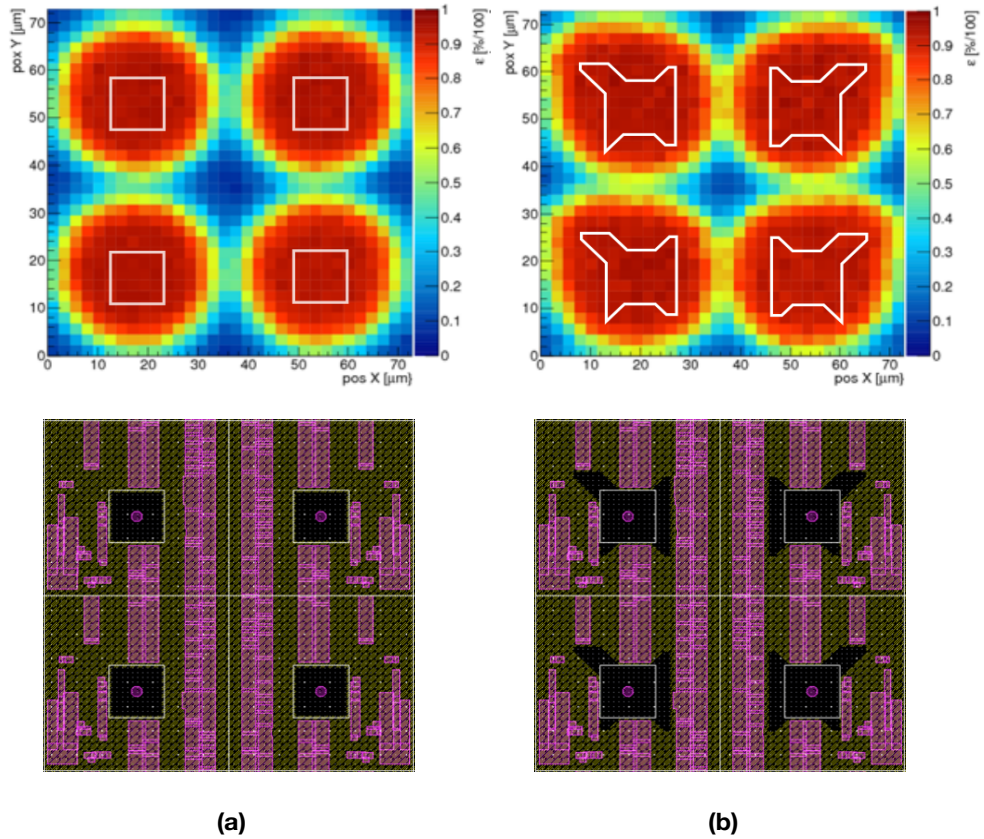

Figure 3.16. (a) Maximum deep p-well design of pixels on the top and its hit efficiency map on the below are represented in the bellow. (b) Minimum deep p-well design of pixels on the top and its hit efficiency map are shown at the bottom. The figures are adopted from (51).

The first large-scale MALTA sensor has been extensively studied based on laboratory characterization tests and test beam measurements. According to the results obtained, the hit efficiency decreases in the pixel corners after irradiation as shared in this section. In addition, the low-threshold configuration is subject to RTS

noise, which makes sensor operation impossible. The first problem can be overcome by process modifications in the pixel design to prevent loss of charge collection efficiency after irradiation. Another modification in front-end design is also needed to reduce noise and operate the sensor at a low threshold.

3.2 Mini-MALTA

3.2.1 Pixel Design and Analogue Front-End Modifications

With the experience gained from the MALTA sensor, the development of the sensor continued with not only modifications on the pixel design but also in analogue front-end design. In this context, the studies were carried out in the simulation environment using the TCAD program. The simulation study (69) shows that modifying the pixel edges extends the electric field lines through the pixel corners and collect the charges by drift even after irradiation. Therefore, two promising modifications that are shown in Figure 3.17 are proposed for the pixel design. The first modification is the removal of the low dose n- implant at the edges of the pixel and the second change is the implementation of an extra deep p-well at the edges of the pixel. These modifications are referred in the thesis as n-gap and extra-deep p-well, respectively. The modifications were applied for the medium deep p-well arrangement in which the p-well is removed from the area below the NMOS transistors.

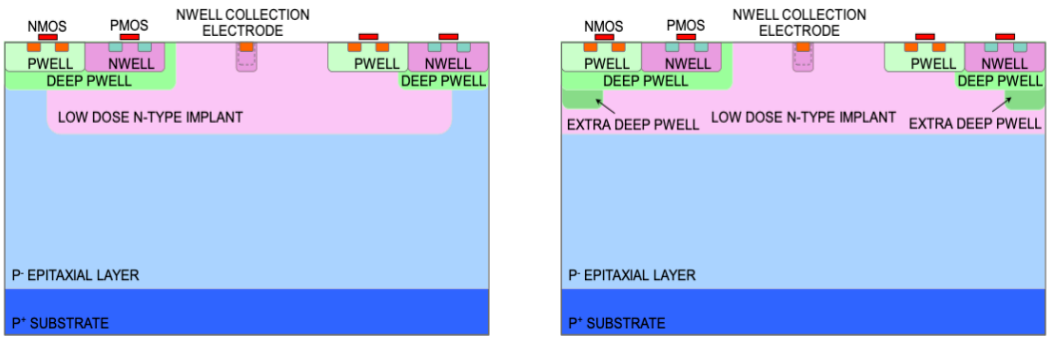

Figure 3.17. Cross-section of the small collection electrode MALTA pixels which are 180 nm Tower Semiconductor modified process with (a) n-gap and (b) extra deep p-well implementation. The figures are taken from (70).

The irradiated MALTA sensor suffers RTS noise, and it was related with the certain transistors in analogue front-end. Therefore, another improvement was done in the front-end side by enlarging some transistors to reduce RTS noise. The

Figure 3.18 shows the analogue front end of the pixel representing the enlarged transistors in the red circles.

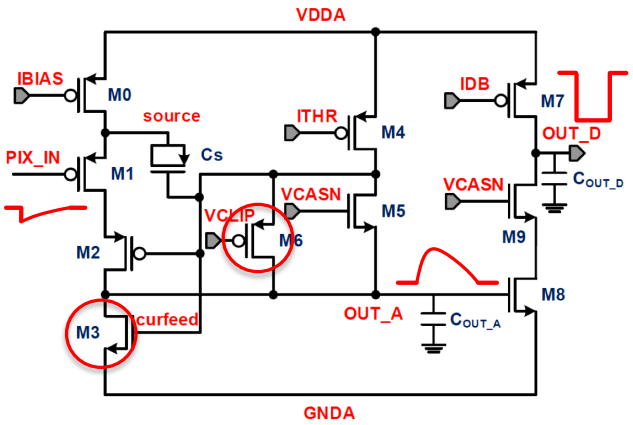

Figure 3.18. Analogue front-end circuit of the sensor are represented indicating enlarged transistors, M3 and M6, in red circle. The circuit diagram is adopted from (51).

3.2.2 Pixel Matrix and Digital Matrix Readout

The mini-MALTA chip matrix consists of 16 × 64 square pixels that have a 3 µm collection electrode and a 36.4 µm pitch size. The full chip measures 1.7 × 5 mm^2 and the top view of the chip is shown in the Figure 3.19 (a) with periphery blocks. In order to compare modifications, the matrix is divided into 8 sectors of 64 pixels and each sector differs in analogue front-end design, reset mechanism and pixel modification. These modifications of the sectors are tabled in the Table. The Figure 3.19 (b) also shows the pixel matrix of the chip representing the modifications.

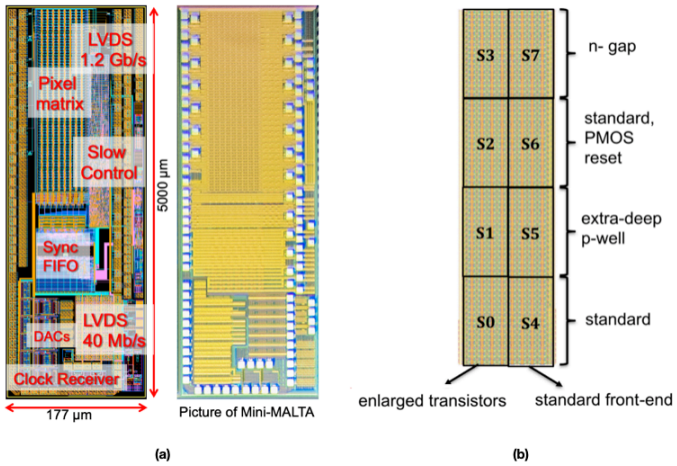

Figure 3.19. (a)The top view of mini-MALTA and (b) the sectors of the pixel which differ in analogue front-end design, reset mechanism and pixel modification. The figures are taken from (70).

Table 3.3. The pixel flavours of 8 different sectors

Sector	Reset	Front-End Design	Process
S0	Diode	Enlarged Transistor	Standard Process
S1	Diode	Enlarged Transistor	Extra-deep p-well implant
S2	PMOS	Enlarged Transistor	Standard Process
S3	Diode	Enlarged Transistor	n-gap implant
S4	Diode	Standard Transistor	Standard Process
S5	Diode	Standard Transistor	Extra-deep p-well implant
S6	PMOS	Standard Transistor	Standard Process
S7	Diode	Standard Transistor	n-gap implant

As can be seen in Figure 3.19 (b) and Table 3.3, three different modifications were used in the sectors. The modified process which is represented as a standard process in table and figure, n-gap and extra-deep p-well modifications were applied to sectors. Except the sectors S2 and S6, the pixels are connected to the continuously active diode reset circuit. However, these two sectors are not working due to problems at the design level. The pixel matrix is divided into two groups that differ in terms of analogue front-end modification. As shown in Figure 3.19, enlarged transistor modification is used in the analogue front-end on the left side of the pixel matrix. On the other hand, the same standard analogue front-end is used as in the MALTA sensor on the right side of the pixel matrix. Putting these features together in one sample give the mini-MALTA sensor advantages to compare modifications with the previous MALTA design.

The digital matrix readout of the mini-MALTA uses an asynchronous readout just as the MALTA sensor has. The digital signals from the digital front-end of the chip are 2 ns wide and are transmitted to the periphery to be stored in the end-of-column logic memory asynchronously. The memory consists of 16 synchronization memories where precise time-of-arrival information is added using a priority encoder. The logic memory is read out by the external 320 MHz clock with respect to the priorities. In the end-of-column logic, the again 4-bit double-column address and the 3-bit bunch-crossing counter-information (BCID) are added in addition to the 22-bit data words to be stored into the FIFO. The mini-MALTA word that is stored in its FIFO is described in Table 3.4. The chip can be operated in two readout modes, fast and slow, which sends 48-bit 8b/10b encoded data from chip at 1.2 Gbps or 40 Mbps, respectively.

Table 3.4. Bit Descriptions of the mini-MALTA output Word

Bit ID	Content
0-14	Binary BCID
15-17	BCID
18	Reference
19-22	FineTime
23-27	Group Address
28-43	Pixel Address
44-47	Memory Address

3.2.3 Laboratory Measurements and Test Beam Results

As with MALTA samples, some characterization tests were performed prior to test beam measurements to determine the effects of radiation damage on samples. Among them, threshold and noise measurements were taken for the enlarged and standard transistor design to compare the performance of the design. Also, other characterization tests of the chips such as the ^{55}Fe source spectra were done and reported in the references. After laboratory measurements, the test beam performance of the irradiated and non-irradiated mini-MALTA samples was completed at DESY and ELSA under 3-5 GeV electron beam. In this subsection, the threshold and noise measurements, as well as in-pixel efficiency maps obtained in the test beam, will be summarized for irradiated and non-irradiated mini-MALTA samples.

In the threshold and noise measurements, three different samples which are unirradiated and two neutron-irradiated with doses 1×10^{15} and 2×10^{15} 1 MeV n_{eq}/cm^2 were characterized. During the measurements, samples were operated with −6 V for substrate and at −2 V for p-well bias and the measurements were performed at the climate chamber at −20°C. The distributions were obtained using the same configuration in the front-ends which gives the highest threshold for each sample. The Figure 3.20 shows the threshold distributions of enlarged and standard transistor designs of non-irradiated and irradiated samples on the left and right, respectively. As can be seen in Figure 3.20 (a and b), the Gaussian fit was applied to the distributions and fit results are shown in the right legend on each plot. The first thing to notice when looking at the distributions is the improvement in the enlarged transistor design which decreases from 570 e^- to 290 e^- for the unirradiated samples. The other difference is in the sigma value compared to the standard transistor design for the unirradiated samples. As threshold dispersion is around 50

e^- in standard transistor design, it decreases around 25 e^- in enlarged transistor design for unirradiated and irradiated samples. In addition, the mean threshold values in irradiated samples with 1×10^{15} 1 MeV n_{eq}/cm^2 were not affected in enlarged transistor design as dramatically as standard transistor design. In standard transistor design, while the difference between unirradiated and irradiated with 1×10^{15} 1 MeV n_{eq}/cm^2 is around 200 e^-, this value is 85 e^- in enlarged transistor design. Both designs have a shifting behaviour toward the low threshold area when the radiation dose amount increases. This behaviour can be explained simply by the radiation damage in the transistors. The enlarged transistor design can be operated at low threshold configuration (around 100 e^-) to achieve high efficiencies for the irradiated samples. The laboratory measurements shows that the conduction of the transistor, M3, has higher conductance than expected in standard design. This results in a large threshold dispersion once combined with a large gain of the transistor as seen in Figure 3.20 (b).

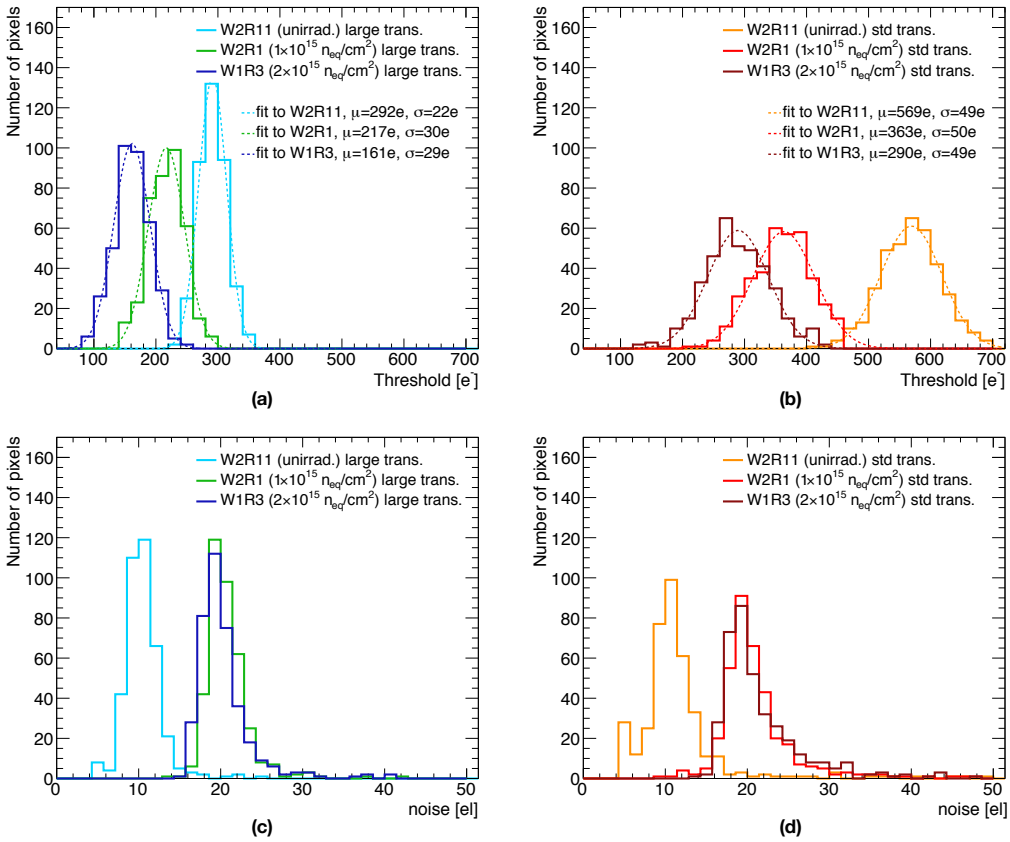

Figure 3.20. The threshold (top plots) and noise (bottom plots) distributions of the unirradiated and irradiated samples with neutron up to 1×10^{15} and 2×10^{15} 1 MeV n_{eq}/cm^2 dose are shown for enlarged and standard transistor designs on the left (a and c) and right (b and d), respectively. The figures are reproduced from (70).

The Figure 3.20 (c and d) also shows the obtained noise distributions of unirradiated and irradiated samples for the enlarged and standard transistor design on the left and right sides respectively. The peak noise values are around 11 e- for both designs. However, the dispersion of the noise decreases from 5 e^- to 3 e^- in the large transistor design compared to the standard design. After irradiation, the peak noise values increase to 20 e^- for both designs. As it can be seen in Figure 3.20 (c), the tail related to RTS noise is decreased in the enlarged transistor design once irradiated samples are considered. Measurements clearly show that the size of these transistors significantly affects RTS noise reduction.

The tracking performance of the mini-MALTA samples was tested under a 2-5 GeV electron beam at DESY and ELSA test beam facilities. The test beam result obtained at ELSA which has a 3.5 GeV electron beam will be summarized in this subsection. The mini-MALTA sample (DUT) was placed in a MALTA telescope which consists of 6 MALTA detectors as planes. The DUT was placed between planes and an additional MALTA plane was attached backside of the DUT as a reference plane. The test beam setup and layout of the planes are shown in Figure 3.21.

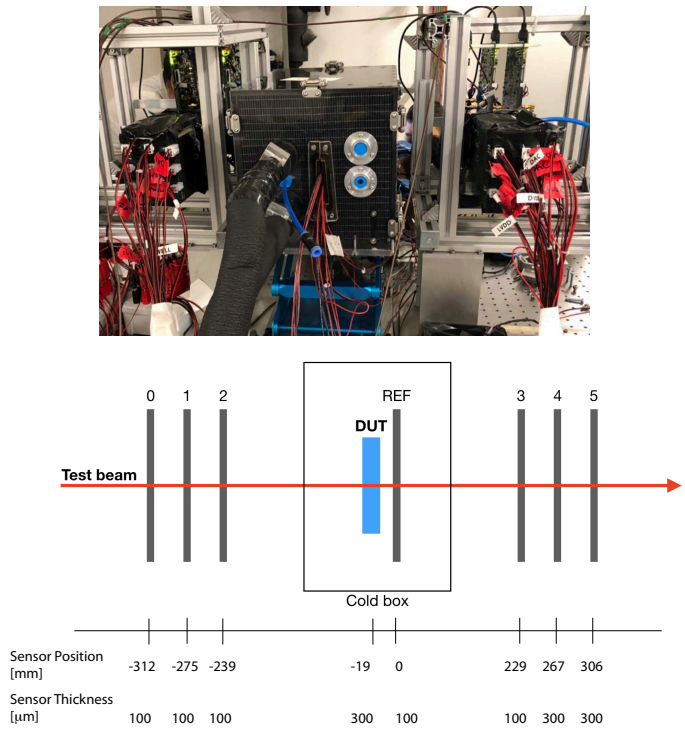

Figure 3.21. The test beam setup (top) and telescope arrangement (bottom) in ELSA. The figure is taken from (70).

During the test beam, the MALTA samples were kept at −20°C to prevent leakage current related to thermal runaways. The substrate of the DUT was biased from −6 V to −10 V to find the best in-pixel efficiency while the p-well was biased to −2 V. Recorded hits from 3 selected planes which are the plane in the front of DUT (Plane 2), the reference plane (REF) and a plane (Plane 3) behind the reference plane were used to build tracks via the Proteus framework as described in the reference (70). Since the electron beam is of low energy, the material used, and the thickness of the planes are important factors in the probability of multiple scattering. Therefore, a method, the General Broken Lines (GBL) formalism (71), which considers all of those factors was used in trajectory calculation in Proteus.

The full hit efficiency maps of non-irradiated and irradiated with 1×10^{15} and 2×10^{15} 1 MeV n_{eq}/cm^2 samples are shown in the Figure 3.22 and mean efficiency results for each sector are summarized in the Table 3.5 giving the mean threshold values of that sector. Comparing the two efficiency maps, it can be clearly seen that the sectors that have enlarged transistor design, the right side of the chip, perform excellent hit efficiency after irradiation. The sector that has no modification except enlarged transistor design has also 91.9% efficiency. Once an enlarged transistor design is combined with pixel modification either n-gap or extra deep p-well, the hit performance reaches beyond 97%. On the other hand, the efficiency of the standard front-end design stays around 87% even pixel has neither n−gap nor extra deep p-well modification. As listed in table, the hit efficiency performance of sample irradiated with 2×10^{15} 1 MeV n_{eq}/cm^2 is also over ≈ 90% for the n-gap and extra deep p-well modification where enlarged transistor design is used.

Table 3.5. The mean efficiency results of non-irradiated and irradiated samples with respect to the threshold value.

Fluence [1MeVn_{eq}/cm^2]	EPI [µm]	SUB [V]	Pixel Modification	Eff. [%] / Th. [e^-] Enlarged Transistor Design	Eff. [%] / Th. [e^-] Standard Transistor Design
un-irrad.	30	-6	n-gap	99.6 ± 0.1 / 200	99.1 ± 0.1 / 380
			extra deep p-well	99.6 ± 0.1 / 200	98.9 ± 0.1 / 380
			continuous n^-	99.6 ± 0.1 / 200	97.9 ± 0.1 / 380
1×10^{15}	30	-6	n-gap	97.6 ± 0.1 / 200	86.5 ± 0.1 / 340
			extra deep p-well	97.9 ± 0.1 / 200	87.0 ± 0.1 / 340
			continuous n^-	91.9 ± 0.1 / 200	78.8 ± 0.2 / 340
2×10^{15}	25	-10	n-gap	92.1 ± 0.2 / 120	73.1 ± 0.3 / 230
			extra deep p-well	93.7 ± 0.2 / 120	76.4 ± 0.3 / 230
			continuous n^-	86.5 ± 0.2 / 120	70.9 ± 0.3 / 230

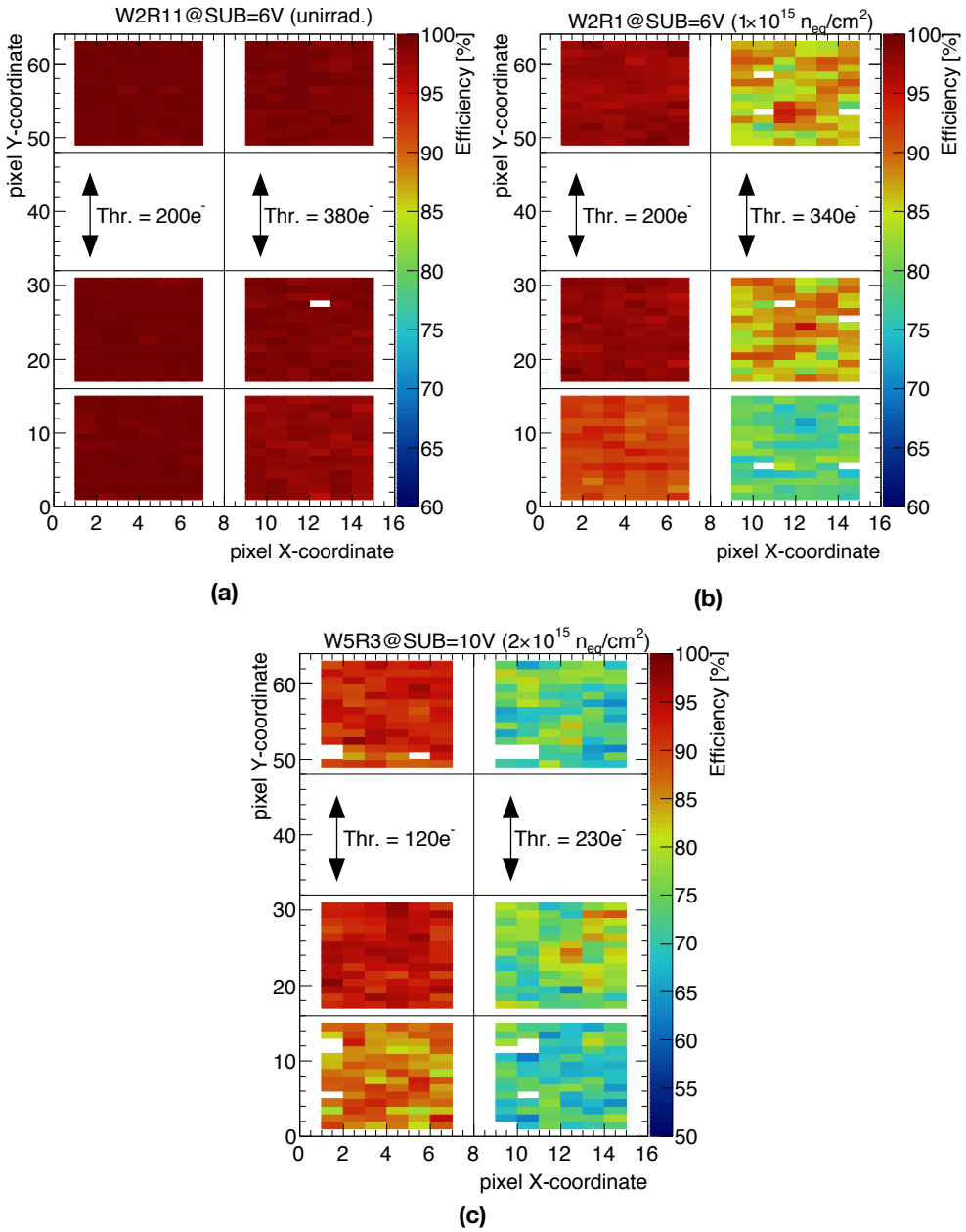

Figure 3.22. The full hit efficiency maps of non-irradiated (a) and irradiated with 1×10^{15} (b) and 2×10^{15} 1 MeV n_{eq}/cm^2 (c) samples are shown with the relative thresholds of the transistor design. The left side of the chip has an enlarged transistor design, while the right side has a standard transistor design. The figures are taken from (70).

After the large-scale MALTA sensor tests, general problems of the sensor were determined and therefore some implementations were proposed for the pixel design and front-end. These proposals were applied to the same chip divided into eight sectors. Thereby, laboratory characterization tests and test beam measurements were completed using a single chip. The results show that one of the main problems, RTS noise, was suppressed with the implementations by enlarging

two related transistors. Compared to the old design, the chip can be controlled with a low threshold configuration after irradiation up to 2×10^{15} 1 MeV n_{eq}/cm^2 without large dispersion. Another problem was the low hit efficiencies on the corners of the pixels after irradiation. The problem can be overcome by process modifications in the pixel design. Two different modifications are low dose n^- implant and implementation of an extra deep p-well at the edges of the pixels were tested. The pixels which have new designs have around 5% better efficiencies than the first design. The obtained results show that the combination of the pixel implementations and enlarged transistors design has 25% better hit efficiency.

3.3 MALTA Czochralski

The Czochralski method (72) allows to grow single crystalline silicon substrates with high resistivity (>3-4 kΩ·cm). It is one of the cheap and fast silicon grown methods in the semiconductor industry. Due to its high resistivity, the Czochralski silicon is depleted at high substrate voltages on the contrary of the epitaxial silicon. This makes it a good candidate for radiation-hard detector applications. Since the collected charge is related to the depth of the depletion region, the deeper the depletion region, the more charge collected via drift from a particle passing through. These not only aid to improve the radiation hardness of the sensor but also improve the time resolution of the sensor as large substrate voltage can be applied. Therefore, MALTA samples were fabricated with Czochralski silicon to combine the advantages of small electrode sensors with the advantages of the large depletion depth.

The MALTA Czochralski (MALTA Cz) samples were manufactured in 300 μm thick and p-type Czochralski substrate. Three different sets of pixel masks are used in the pixel implant designs: continuous n^- layer, n-gap, and additional deep p-well which shown in Figure 3.2 and Figure 3.17, respectively. However, the enlarged transistor design which is used in mini-MALTA is not implemented to the MALTA Cz samples and the standard analogue front-end design is used the same as the first MALTA (see Figure 3.5). The pixel matrix layout is also the same as the first MALTA pixel layout. It consists of 8 sectors and each sector has a different pixel flavour as listed in Table 3.1. The MALTA Cz's digital matrix readout uses the same asynchronous readout that the first MALTA sensor has.

3.3.1 Test Beam Results

Since the MALTA Cz has no modification on the front-end design, the threshold and noise measurements results are the same as the first MALTA sensor as expected. For that reason, the threshold and noise distributions of the MALTA Cz will not be discussed in this section. The threshold and noise values in the hit efficiency of the pixels will be detailed in the captions of the figures. As discussed in the mini-MALTA section, even though the front-end of the pixel has no modification in the transistors, n-gap or additional deep p-well modifications in the pixel design have an impact on tracking efficiencies by improving the electric field at the pixel edges resulting in additional charge collection via drift for the irradiated samples. When these modifications meet with the Czochralski silicon, the radiation hardness of the MALTA Cz is expected to improve more. In order to avoid confusion, the MALTA produced with epitaxial silicon will be entitled as MALTA EPI in the thesis after this section.

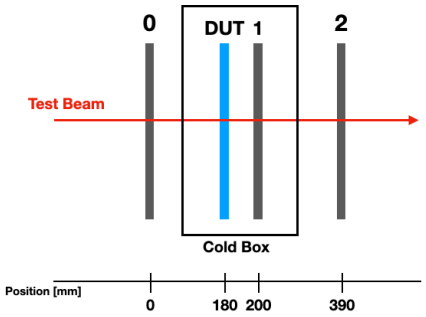

Figure 3.23. The test beam telescope arrangement in DESY

The MALTA Cz and MALTA EPI samples were tested at DESY under a 4 GeV electron beam. The MALTA samples (EPI or Cz) were placed in a MALTA telescope which consists of 4 MALTA planes. The reason for using 4 planes is the place them close and avoid multiple scattering of electrons which occurs at low energies. The orientation of the telescope planes and DUT are shown in Figure 3.23. During the test beam, the DUT was kept at −20°C to avoid leakage current related to thermal runaways as did in previous test beams. The MALTA Cz samples were operated at the substrate was biased up to −55 V while the p-well was biased to −6 V. On the other hand, the substrate of MALTA EPI samples was operated up to −10 V keeping p-well at −6 V. During the data taking procedure, Plane 2 was used as a trigger plane in the telescope setup and hits from Plane 0 and Plane 1 were used to build tracks via the Proteus framework. In the reconstruction of the tracks, again

GBL formalism was preferred due to the low energy of the beam and large scattering probability. Using reconstructed tracks, in-pixel efficiency results of unirradiated and irradiated MALTA Cz and EPI samples were obtained and represented with 2 × 2 pixel matrix maps from Sector 2 of the sensor matrix. In Figure 3.24, hit efficiency and cluster sizes of continuous n^- layer pixel design is shown for unirradiated Cz and EPI samples. As expected, both samples have over 98% hit efficiency if they were not irradiated. However, the Cz sample tends to be a large cluster size in the pixel. While the average cluster size of EPI samples is 1.25 pixels, it is around 1.45 pixels for Cz samples at the same substrate bias (−6 V). The MALTA Cz has large cluster size at the edges of the pixels compared to MALTA EPI when the substrate voltage were increased to −30 V as seen in Figure 3.25. Since EPI samples reaches full depletion around at −15 V substrate bias, expanding of depletion region stops. In the Cz samples, on the other hand, the expanding of the depletion region stops around at −55 V already at −30 V Cz substrate has deeper depletion than EPI. This results in more charge production in the depletion region and therefore charges are shared with other pixels especially at the edges of the pixels.

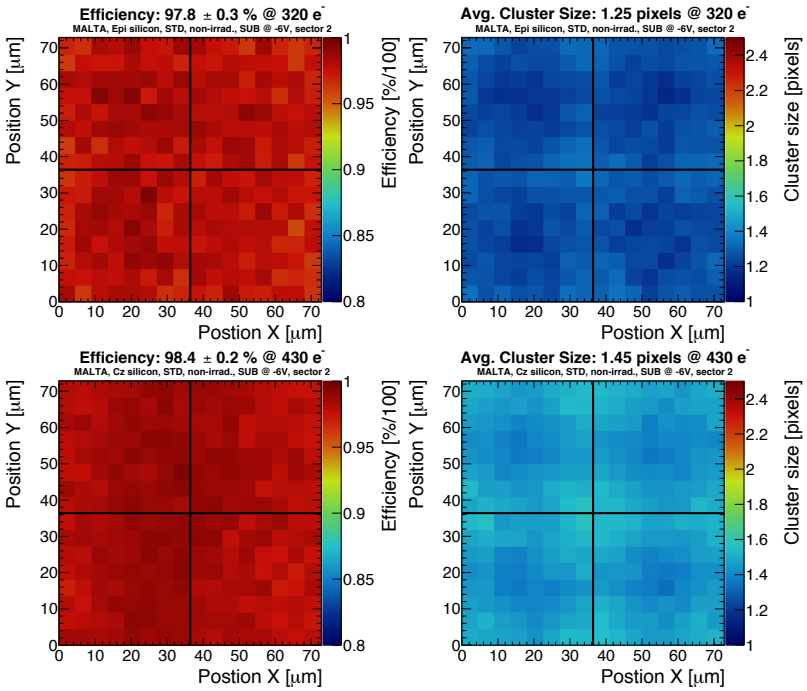

Figure 3.24. The in-pixel efficiencies and cluster sizes of unirradiated EPI (on the top) and Cz (on the bottom) MALTA samples for continuous n^- layer pixel design at -6V substrate bias. The threshold values of EPI and Cz sample are 320 e^- and 430 e^-, respectively.

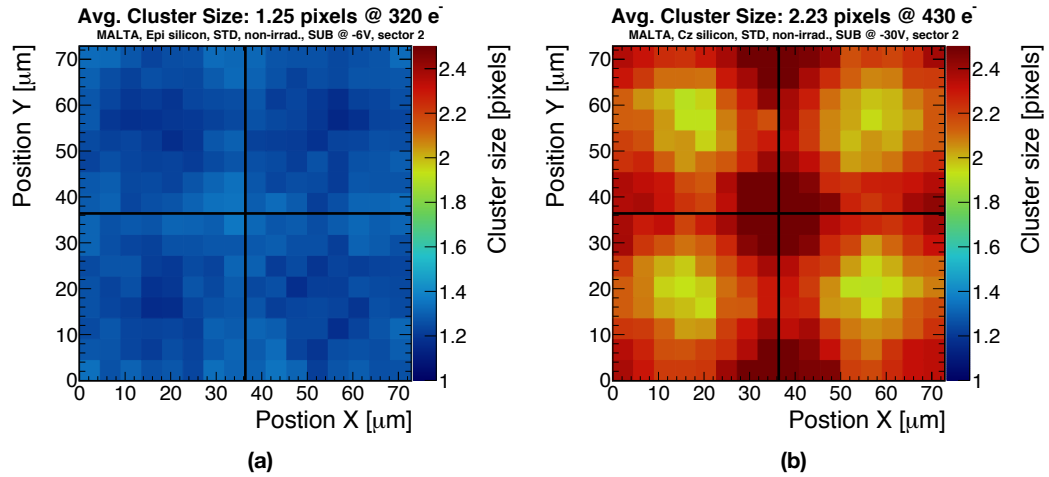

Figure 3.25. The cluster sizes of unirradiated EPI (a) and Cz (b) MALTA samples for continuous n^- layer pixel design at -30V substrate bias. The threshold values of EPI (a) and Cz (b) sample are 320 e^- and 430 e^-, respectively.

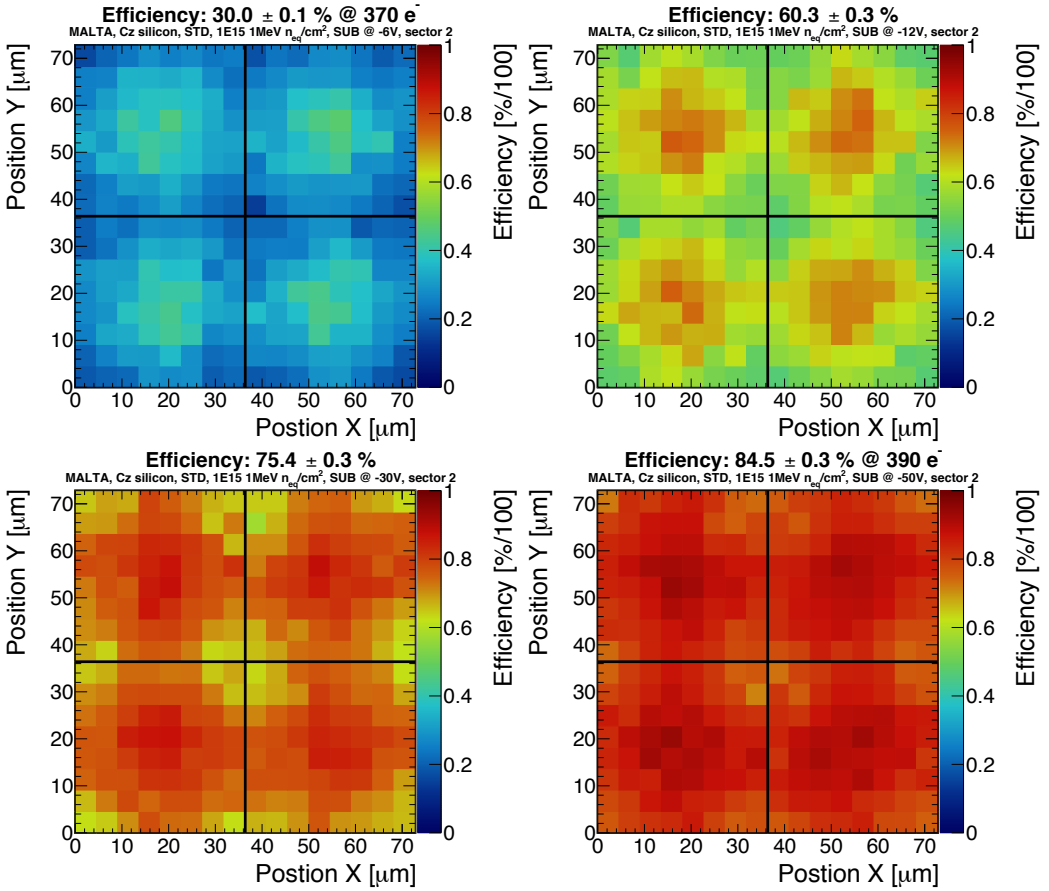

Figure 3.26. The in-pixel efficiencies of irradiated (1×10^{15} 1 MeV n_{eq}/cm^2 NIEL dose) MALTA Cz sample with respect to the substrate bias voltage which increases from top left to bottom right. The obtained threshold value of the sample is around ~360 e^-.

This feature of the Cz silicon has also an impact on hit efficiency for the irradiated samples. Increment of applied bias voltage to substrate results in high efficiency like 84.5% at −50 V substrate bias even for continuous n^- layer pixel design which did not exceed 80% in EPI samples at low threshold configuration (≈200 e^-) for 1×10^{15} 1 MeV n_{eq}/cm^2 NIEL dose. The evolution of the tracking efficiency with respect to the substrate voltage is shown for pixel maps in Figure 3.26. As it can be seen, there is still in-pixel efficiency loss, ≈15%, on the edges of the pixels for continuous n^- layer design despite the high substrate bias application. There is already an improvement in-pixel hit efficiency in mini-MALTA samples for irradiated samples when n-gap or additional deep p-well pixel modifications are taken into account. Since not only the MALTA Cz depletion region grows at the high substrate bias voltage but also n-gap or extra deep p-well pixel modification increases the electric field at edges of the pixels, more charge can be collected by drift from the pixels for irradiated samples with less loss. Therefore, a combination of these pixel modifications and Cz silicon were achieved a better hit efficiency for irradiated MALTA Cz samples. The hit efficiency maps were obtained for continuous n^- layer, n-gap, extra deep p-well pixel modifications which irradiated NIEL dose and they are shown in Figure from left to right respectively. The average efficiencies for both designs, n-gap and extra deep p-well, are over 95% and the efficiency loss at the pixel corners is almost disappeared as seen in Figure. Moreover, these results were obtained at high threshold values to avoid RTS noise which exists at low threshold values.

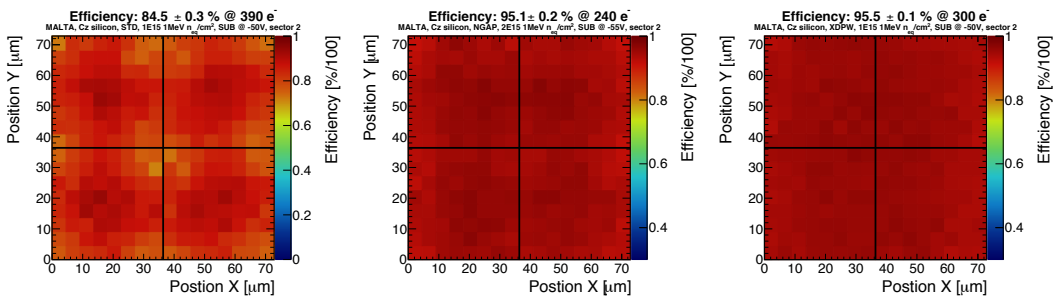

Figure 3.27. The in-pixel efficiencies of irradiated (1×10^{15} 1 MeV n_{eq}/cm^2 NIEL dose) MALTA Cz sample for continuous n^- layer, n^- gap, extra deep p-well pixel modification respectively. The obtained threshold values of the samples are 370 e^-, 260 e^- and 300 e^- from left to right.

As mentioned earlier, MALTA Cz is expected to have high time resolution because of the applied high substrate voltage that creates a strong electrical field and charges collected quickly by drift. In order to measure the time resolution of the Cz and EPI MALTA samples, a time to digital converter, ASIC chip, was used to measure hit times precisely during the test beam. This device is PicoTDC (73) and the time of output signals of the telescope planes was tagged with it. PicoTDC was developed with experience gained from the HPTDC chip (74) used in High Energy Physics (HEP) experiments for the last 15 years. It bins the time of 3 ps or 12 ps with low jitter which is below 1 ps. Therefore, it can be used in many fields such as medical imaging, material research, laser ranging and of course HEP experiments. In the test beam, the time was measured with PicoTDC using 3 ps binning from Plane 0, DUT and Plane 2 for unirradiated EPI and Cz samples. Since there should be a linear relationship between planes in terms of time, the time differences between planes were taken and Gaussian-shaped distributions were obtained as shown in Figure 3.28.

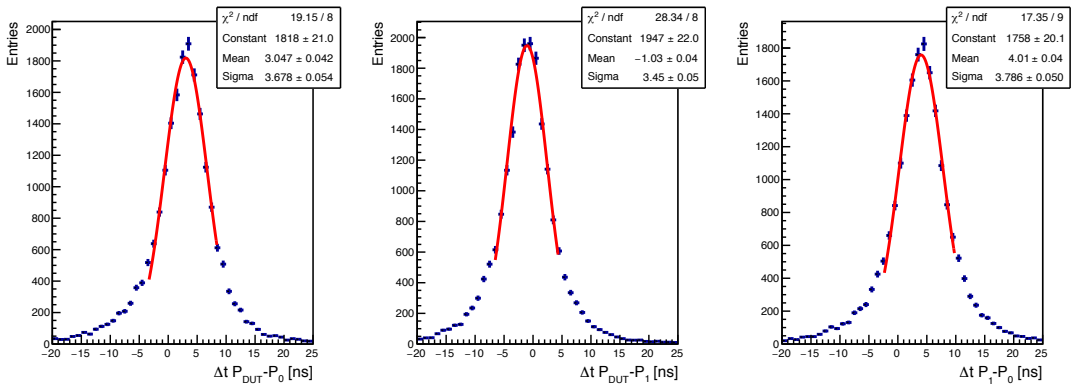

Figure 3.28. Distribution of the time difference between telescope planes and MALTA Cz (DUT) which has continuous n^- layer pixel design measured at DESY with a 4 GeV electron beam. Distributions require at least one hit on each plane.

To calculate the time resolution of the DUT, the time difference distributions were fitted to the Gaussian function, taking into account that at least 50% of the events are covered in the fits. Then, sigma values of these fits were used in the calculation using linear relation between them. For instance, the obtained sigma value from the time difference distribution of Plane 0 and DUT is σ_{12} and it is equal to;

$$\sigma_{12}^2 = \sigma_1^2 + \sigma_2^2 \tag{3.2}$$

where time resolutions of Plane 0 and DUT are represented with σ_1 and σ_2, respectively. Similarly, same relations can be written for the other obtained sigma values as it follows:

$$\sigma_{23}^2 = \sigma_2^2 + \sigma_3^2 \tag{3.3}$$

$$\sigma_{13}^2 = \sigma_1^2 + \sigma_3^2 \tag{3.4}$$

where σ_1, σ_2 and σ_3 are represents the time resolutions of the planes relative to the Plane 0, DUT and Plane 1.One can evaluate time resolution of DUT (σ_2) from these equations (Eq. 3.2, Eq. 3.3 and Eq. 3.4) using their relations;

$$\sigma_2 = \sqrt{\frac{\sigma_{12}^2 + \sigma_{23}^2 - \sigma_{13}^2}{2}} \tag{3.5}$$

According to the Eq. 3.5, the time resolution of unirradiated MALTA EPI and Cz samples that have with n^- layer pixel design was obtained and time resolutions were represented as a function of the substrate voltage are shown in Figure 3.29. Since the non-irradiated EPI sample reached full depletion at −6 V unlike Cz silicon, the MALTA EPI sample was measured at this substrate voltage, but the bias voltage of the Cz substrate was increased to various voltages up to −40 V. As it can be seen in Figure, this improved the time resolution of Cz substrate as expected. Time resolution on the EPI sample is 2.60 ± 0.05 ns at −6 V, while the time resolution on the Cz sample is compatible with 1.7 ± 0.1 ns between −10 V and −30 V. The hit efficiency of irradiated MALTA Cz was better than the MALTA EPI. In addition to the radiation tolerance of the sensors, it is clear that Cz silicon has better time resolution performance compared to EPI. The time resolution of the MALTA Cz is promising once the 25 ns bunch crossing time is considered for HL-LHC. As mentioned above, the results were obtained using at least 50% of time measurements and this leads to the efficiency loss in the pixels. Therefore, the results show that modifications are needed at the analogue front-end in addition to the enlarged transistor design that suppresses RTS noise in mini-MALTA.

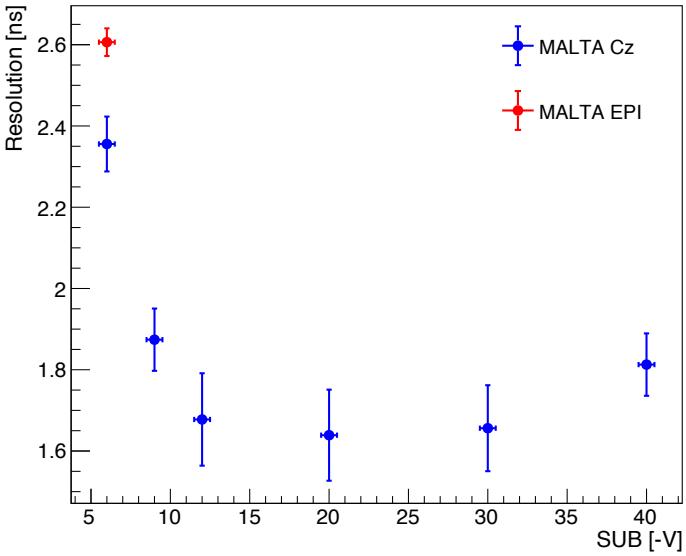

Figure 3.29. Time resolutions of the EPI and Cz MALTA samples as a function of substrate bias voltage. Time resolutions are calculated by the linear combination of the sigma values of the Gaussian fit to time difference between telescope planes. The figure is reproduced from (75).

3.4 MALTA2

3.4.1 Pixel Design, Pixel Matrix and Digital Matrix Readout

A new MALTA sensor was developed with the experience gained from MALTA, mini-MALTA and MALTA Cz. This developed sensor is named MALTA2 on account of the implementation of previous updates and adding new features (76). Important changes were made to the pixel, pixel matrix and analogue front-end designs. The MALTA2 samples were manufactured on a 300 µm thick p-type Czochralski or EPI substrate and some of the samples were thinned to 100 µm. Three different sets of pixel masks are used in MALTA Cz for the pixel implant designs: continuous n^- layer, gap in the n^- layer and additional deep p-well which are depicted in Figure 3.2 and Figure 3.17, respectively. The sensors were produced with a 180 nm Tower CMOS imaging process. The pixel design was kept the same as the previous MALTA samples except for 30 µm continuous n^- layer dopant density. The dopant level of the MALTA2 sample is represented in the thesis as low, intermediate and high, where intermediate was the same dopant level used in MALTA, mini-MALTA and MALTA Cz. This modification was done to monitor radiation tolerance and the effect of time resolution on the MALTA2 samples. The pixel pitch of 36.4 µm is not changed for MALTA2 but the pixel matrix is changed from 512 × 512 pixels to 224 × 512 pixels which are equal to 10.12 × 20.2 mm^2 total detection area. The pixel matrix is not divided into sectors. The pixels in the

matrix has the same properties in terms of pixel design, collection electrode size, spacing between collection electrode and read-out circuitry and reset mechanism, etc. The micrograph of the MALTA2 chip is shown in Figure 3.30. The pixels have a 2 μm diameter octagonal-shaped n-well collection electrode and spacing between collection electrode and read-out circuitry covered by p-well is 4 μm to the corners.

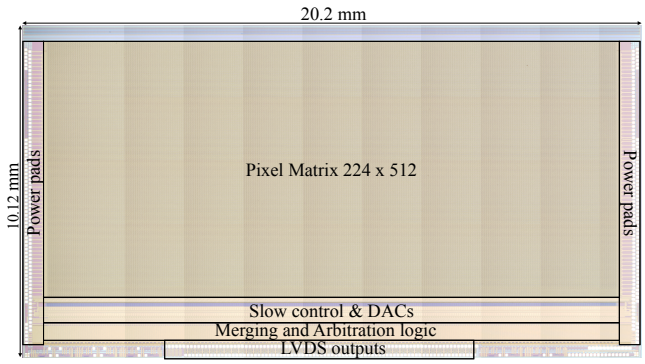

Figure 3.30. The micrograph of the MALTA2 chip and is adopted from (76).

3.4.2 Analogue Front-End Design and Read-out

MALTA2 comes up with a new front-end design but the changes made in the front end contain a lot of technical information and are not the subject of this thesis. Therefore, the main changes of front-end will be discussed briefly but more technical and detailed explanations of the front-end can be found in the reference (76). As discussed in the mini-MALTA section, some of the transistors were responsible for RTS noise after irradiation in the first MALTA prototypes so their size was enlarged in the design of the mini-MALTA front-end. However, the MALTA2 front-end design was re-designed instead of keeping some components that one used in mini-MALTA or MALTA. The analogue front-end circuitry of MALTA2 is shown in Figure 3.31. In the design of MALTA2, the diode reset circuitry which is the same as in previous MALTA samples transmits the collected charge as an input signal to an amplifier. On the other hand, major changes are made to transistor elements. The first change is the introduction of cascode transistor, M3, to the analogue front-end. The main advantage is the prevention of the Miller effect, a phenomenon known in voltage amplifiers that increases the input capacitance. Besides, the capacitance of C_s is enlarged to not only increase the gain but also increase the feedback loop speed of the amplification stage. Another change is made in the size of the M4 making it bigger which results in low output capacitance. This not only helps to deal with RTS noise but also improve the timing performance of

the front-end. As discussed in the previous chapter of the thesis, TID is responsible for leakage current in transistors and an Enclosed Layout Transistor (ELT) design is the solution to suppress the effects of the TID. The transistor M6 is designed as ETL to eliminate TID effects. In short, it is aimed to obtain an analog front end that can be controlled with high gain and low noise with this design.

Asynchronous digital matrix readout of mini-MALTA is not modified and retained in MALTA2. The 48-bit encoded data is transmitted from the chip by LDVS drivers. The descriptions of the MALTA output word are same for MALTA2 as detailed in Table 3.4.

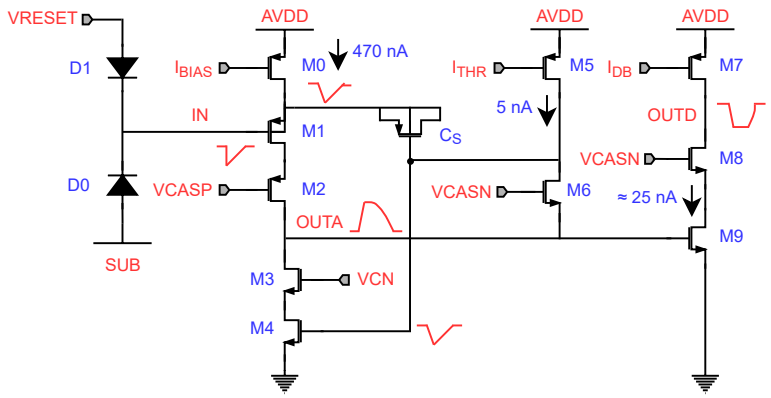

Figure 3.31. The illusturation of analogue front-end circuit of the sensor and stages of collected charge pointing out IN (pixel input of signal), OUTA (amplifier output of signal) and OUTD (discriminator output of signal). The circuit diagram is taken from (76).

3.4.3 Laboratory Measurements

To determine the performance of the front-end design, some characterization tests were performed in the laboratory as did in previous versions of MALTA. The first laboratory measurement was the threshold and noise measurements for non-irradiated samples. Since the front-end design changed in MALTA2, a better threshold and noise performance were obtained compared to MALTA as shown in Figure 3.33. The threshold dispersion of MALTA2 is not large as MALTA and is still around 10% as with MALTA at the same threshold level but one can see difference in noise distribution that the tail related to RTS is disappeared in MALTA2. This behaviour allows homogeneous threshold settings without the need of an in-pixel threshold. Similarly, the same measurements were made for the irradiated MALTA2 sample with 3×10^{15} 1 MeV n_{eq}/cm^2 NIEL dose and the results

are compared with non-irradiated MALTA2 sample at the same threshold configuration for both chips. During the measurements, bias voltage applied to substrate of samples was -6 V and samples were kept at 20°C temperature to prevent thermal leaks. Obtained threshold and noise distributions are shown in Figure 3.44. It can be seen that the threshold value of the MALTA2 sample can reach the ~100 e^- with small dispersion for 3×10^{15} 1 MeV n_{eq}/cm^2 NIEL dose which was impossible in MALTA samples. Also, the mean noise value increases from 6 e^- to 12 e^- after irradiation without RTS related tail. These results demonstrate the improvements in the new analogue front-end against NIEL radiation.

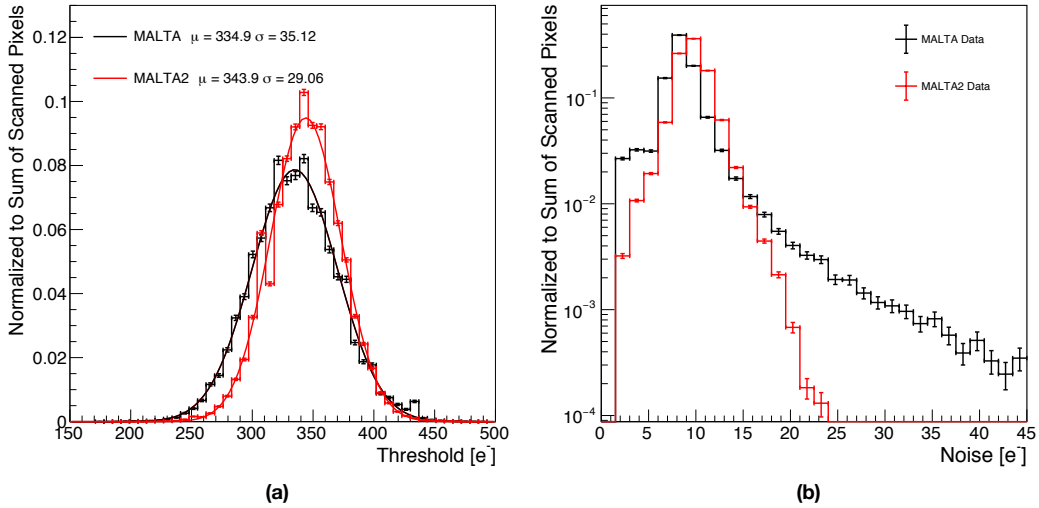

Figure 3.32. (a) The threshold distribution of unirradiated MALTA and unirradiated MALTA2 samples (both EPI silicon with n-gap pixel design) are represented with black and red colors, respectively. The Gaussian fit separately applied to threshold distributions and fit results are shown in the legend of the graph. (b) The noise distributions of the same samples are represented with black and red colors, respectively.

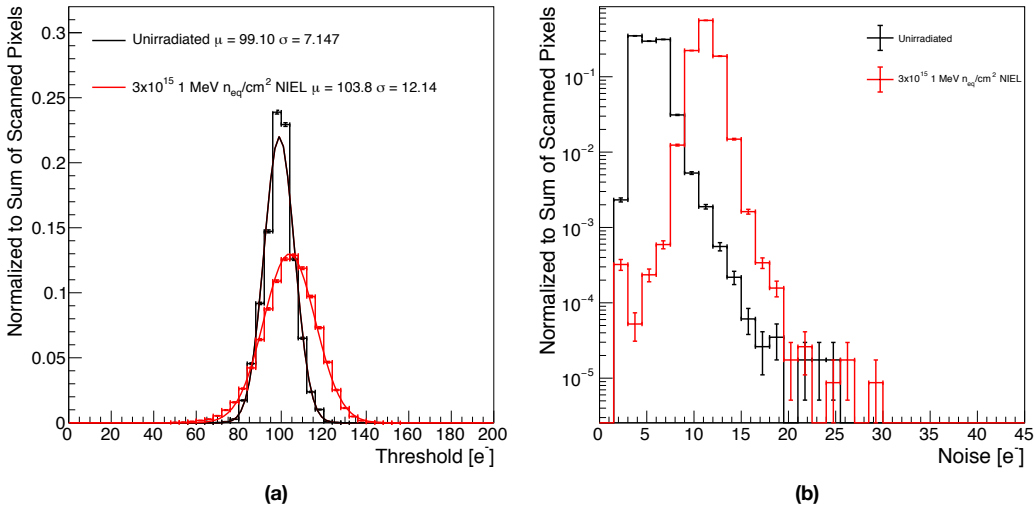

Figure 3.33. (a) The threshold distributions of unirradiated MALTA2 and irradiated MALTA2 with 3×10^{15} 1 MeV n_{eq}/cm^2 NIEL dose samples (both EPI 100 µm thick silicon with n-gap pixel modification) are represented with black and red colours, respectively. The Gaussian fit separately applied to threshold distributions and fit results are shown in the legend of the graph. (b) The noise distributions of the same samples are represented with black and red colors, respectively.

In addition to threshold and noise measurements, the analogue front-end performance of the MALTA2 sample was also tested for high TID levels starting from 25 krad/min up to 100 Mrad with X-rays. During the measurements, the bias voltage applied to the substrate was −6 V and samples were kept at 10°C temperature to avoid an annealing effect. The threshold dispersion and noise were measured after each desired irradiation dose keeping the threshold value of the sensor at 100 e^-. The threshold dispersion and noise with respect to the TID levels are shown in Figure 3.34. While the threshold dispersion reaches the maximum at 10 Mrad and stays around 22.5 e^- till 100 Mrad, the noise increases from 5.9 e^- to 22.5 e^- as a result of RTS noise. These threshold dispersion values are below the MALTA threshold dispersion at 70 Mrad (see Figure 3.10) but noise values are similar to MALTA. After 24 hours of room temperature annealing, the threshold dispersion and noise decrease around 19 e^- and 15 e^-, respectively. In the default annealing process, the sample has to annealed again at 180°C temperature for 24 hours after the room temperature annealing process. However, since the sample is bonded to a carrier board, the carrier board, and its components on it are damaged at this temperature level. Therefore, the chip was annealed at 80°C temperature for 24 hours. Nevertheless, improvement was observed in the threshold distribution, which decreased to 7.5 e^-, and the noise came to 13 e^-.

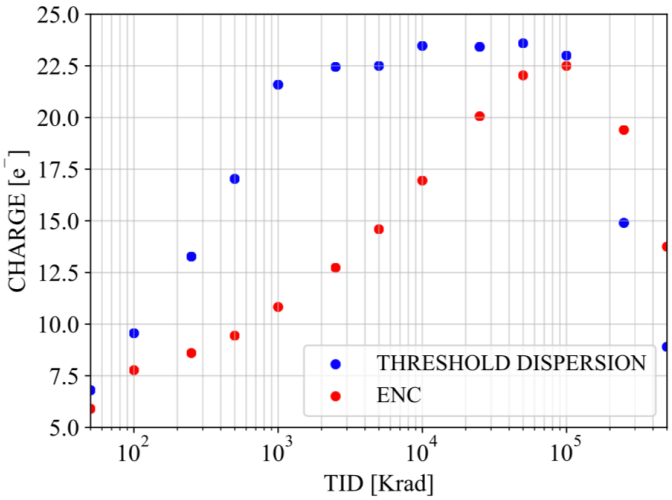

Figure 3.34. The analogue front-end performance of the EPI MALTA2 sample with n-gap pixel modification as a function of TID. While the blue points represent threshold dispersion, the red points indicate noise of analogue front-end for threshold value at around 100 e^-. The last two points locate at 250 Mrad and 500 Mrad show the threshold dispersion and noise values after 24-hour room and 80°C temperature annealing process. The figure is taken from (76).

After TID measurements of MALTA2 samples, another important laboratory measurement, the time-to-threshold curve or time walking curve, was also made for the MALTA2 sensor. The time walking curve is basically the behaviour of the analogue front-end speed relative to the amount of charge collected. As discussed, the collected charge is evaluated by the analogue front end and transmitted to the digital circuit. However, the amount of charge collected directly affects the time spent on the analogue front-end and it is inversely proportional to signal amplitude. The time spent for the amplification process should be less than the bunch crossing time of the collider for example 25 ns for HL-LHC or FCC-hh (see Table 1.1). Otherwise, the events cannot be recorded correctly and result in pile-up in electronic devices. The time walk measurements of unirradiated EPI and Cz MALTA2 samples were performed by using the charge injection circuitry that sends pulses to pixel with different amount of charge as done in threshold measurements. Since measurement was made by charge injection, substrate voltage of the samples was set −6 V while the p-well was biased to −6 V during the measurements. The measurement was done at the lowest threshold configuration that can achieve in that chip. The time difference between the trigger and the MALTA2 output signal after the different amounts of charges injections into the pixel which is the closest one to the digital periphery was determined using

measured times with PicoTDC. The obtained time walk curves of MALTA2 samples are shown in Figure 3.35. The measurements show that the output of the analogue front-end of MALTA2 responds quickly with respect to the injected charge amounts. Indeed, the time consumed in the analogue front-end for 100 e^- is six times larger than 400 e^- as seen in the MALTA2 EPI sample.

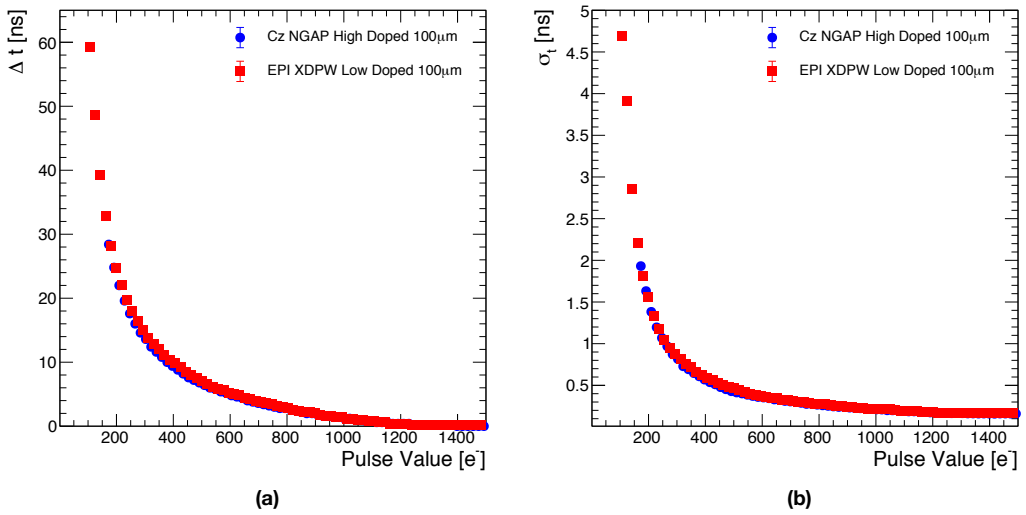

Figure 3.35. Time walk distribution as a function of injected charge for Cz (blue) and EPI (red) MALTA2 samples. While the Cz sample is 100 µm thick with high doping and n-gap modification, EPI sample is 100 µm thick with low doping and additional deep p-well modification pixel design.

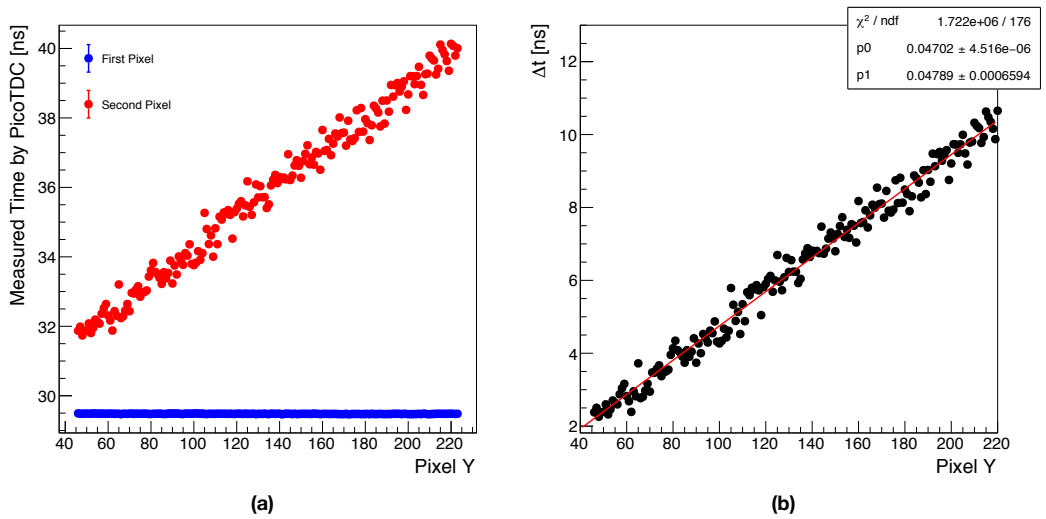

Figure 3.36. (a) The measured arrival times of the two pixels with PicoTDC for the 5th column of MALTA2 sample. The graph was produced by holding the first pixel (blue colour) in a fixed position at the bottom of the column and moving the second pixel (red colour) along the column and measuring the arrival time of signals from these pixels at the same time. (b) Time difference between second and first pixel arrival time measure by PicoTDC and applied linear fit to this time difference distribution.

The jitter at the analogue front-end was also determined for unirradiated MALTA2 samples. In the measurements, the again charge injection circuit was used and a charge (~1400 e^-) above the threshold is simultaneously injected into two different pixels on the same column. Then, the arrival time of the pixels hits was measured with PicoTDC. The measurement was repeated by keeping the first charge injected pixel at the bottom of the column and moving the second pixel along the column. Since the first pixel is close to the digital periphery, the signal was arrived before the other one as expected. On the other hand, the output signal of the second pixel was transmitted after the first pixel. In short, while the arrival time of the first-pixel signal was the same for every measurement, the arrival time of the first-pixel signal was increased the further away from the digital periphery. However, process variations from pixel-to-pixel result in slight variations since every pixel has own analogue front-end. This behaviour is quantified as the jitter of the analogue front-end and it is shown in the Figure 3.36 (a). The time difference between the first pixel measurements and the second ones gives a linear distribution as shown in Figure 3.36 (b). Applying linear fit to the time difference and determining the distribution of the distance between each individual point and that fit line gives the jitter of the analogue front-end. Basically, it defines the variation in the timing of the signal from its nominal value and therefore it depends on noise. However, every pixel has its own analogue front-end as mentioned and more statistic is needed to obtain the mean jitter of the whole pixel matrix. Hence, the measurement is shown in Figure 3.36 (a) was repeated for every fifth column of the matrix in total 100 columns. Then, the distance between each individual point and obtained fit on that column was determined and the mean jitter of the pixel matrix was obtained by applying a Gaussian fit to the distribution. The obtained jitter distributions of the two non-irradiated MALTA2 Cz samples that have different continuous n^- layer dopant densities and applied Gaussian fits to those distributions are shown in Figure 3.37. As a result, both MALTA2 samples have jitter around ~300 ps, indicating that time resolution better than 1 ns cannot be attainable as it is equal to 3σ of each distribution. This is a benchmark measurement and considerable effort is needed to put the matrix design of the next generation of MALTA sensor to reduce jitter.

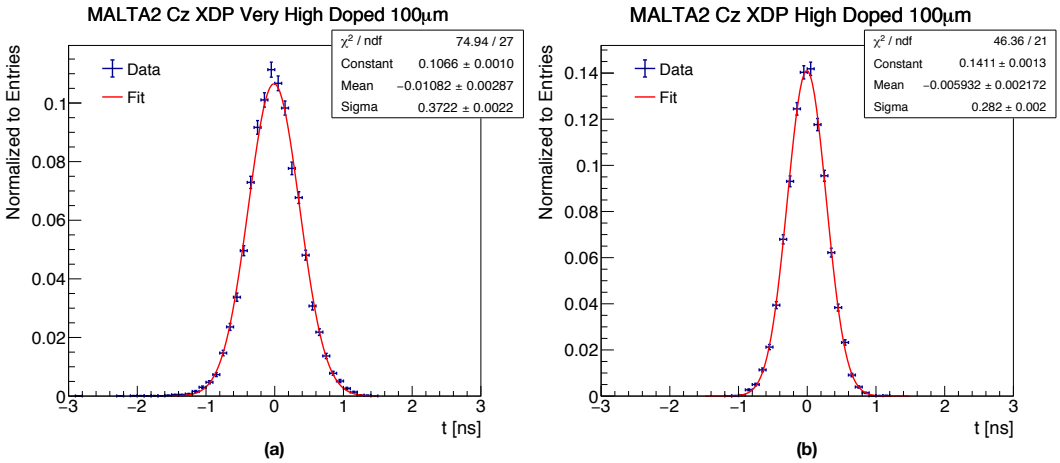

Figure 3.37. Jitter of the MALTA2 analogue front-end electronics measured every 5th column on Cz sensors with additional deep p-well thinned down to 100 μm for two different doping concentrations. The low doping (a) has 282 ± 2 ps jitter while the higher (b) doping has 372 ± 2.2 ps jitter.

In short, the laboratory measurements show that the MALTA2 analogue front-end has better performance for radiation endurance compared to MALTA. Besides, it has a low time walk at a large charge collection with a small jitter on the front-end. Considering the minimum ionizing particle which produces around 1500 e^- in the silicon that has a 30 um depletion depth, MALTA2 samples transmit the signal that has larger than 400 e^- within 10 ns to the digital periphery. Considering the charge sharing between 4 pixels, this value is still under the bunch crossing times of LHC, HL-LHC and even FCC-hh. This property makes MALTA2 reliable not only for HL-LHC but also for future circular colliders such as FCC-hh. However, the signal down to the column with around ~300 ps jitter can be a problem for time tagging especially a large number of pile-up events that occur after a bunch crossing. Therefore, the jitter of MALTA2 on the front-end is needed to be improved for FCC-hh.

3.4.4 Test Beam Results

The unirradiated and irradiated MALTA2 samples were tested at SPS under a 180 GeV pion beam. The MALTA2 samples were placed in a MALTA telescope which consists of 6 MALTA planes and hosts two DUTs at the same time. The telescope layout is shown in Figure 3.38. Similar to the previous measurements, the DUT was kept at −20°C to prevent leakage current related to thermal runaways. The substrate of MALTA2 Cz samples was biased from −6 V to −55 V but the

substrate of MALTA EPI samples was operated up to −10 V keeping the bias voltage of p-well which houses the electronic periphery at −6 V for both types of MALTA2. A scintillator plane with a PMT module was placed in the back of Plane 6 and was used as a trigger unit of the telescope for better timing. Again, the Proteus framework (68) was used in the reconstruction of the tracks on the planes and DUTs. Before the reconstruction, the coarse and fine alignment of the detector planes and DUTs were done for accurate reconstruction. Otherwise, misalignment can result in incorrect track reconstruction and a lack of efficiency in the pixel matrix can be observed. In the reconstruction of the tracks, the General Broken Lines algorithm used in previous measurements was not preferred due to the large beam energy at SPS and negligible particle scattering. Therefore, a simple method, linear regression fit, was applied in the track reconstruction. It uses each hit on the telescope planes to reconstruct track intersections on DUT by applying linear regression fit to these hits. If the reconstructed track intersections on DUT are close to the hits on the DUT, the reconstructed track is used in the determination of efficiency or cluster size distributions of pixels. The residual distribution between reconstructed track position and the center of the cluster on DUT was determined for *X* and *Y* directions. In other words, tracks are reconstructed with resolution of ~10.25 µm on *X* and ~10.23 µm *Y* directions as shown in Figure 3.39.

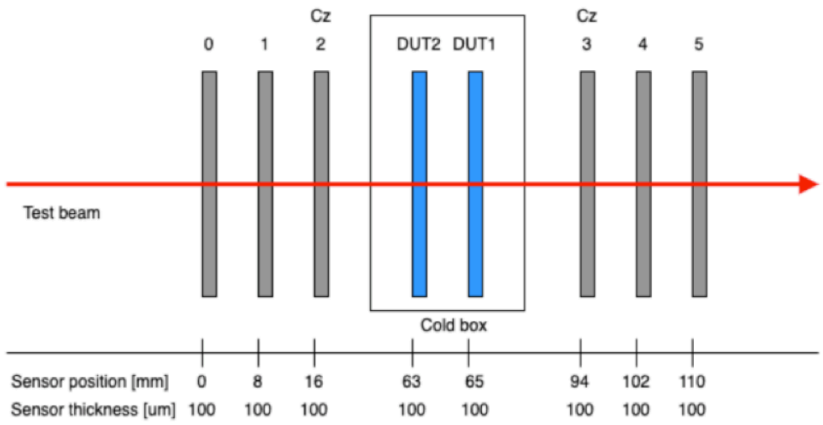

Figure 3.38. The test beam telescope arrangement in SPS

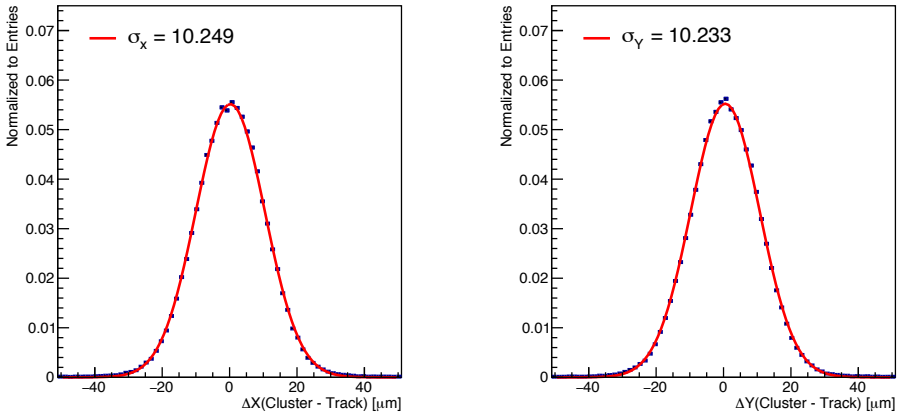

Figure 3.39. The residual distribution between reconstructed track position and the center of the hit cluster for X (left) and Y (right) directions.

In this section, the average pixel efficiency and the average cluster size of the track hit for the irradiated MALTA2 samples are shown instead of pixel maps. In Figure 3.40, the average pixel efficiency and average cluster size of irradiated with 1×10^{15} 1 MeV n_{eq}/cm^2 NIEL dose MALTA2 EPI, which has the extra-deep p-well pixel modification with low n^- layer dopant density, are shown as a function of the substrate voltage for the three threshold values ordering high, medium and low. The pixels reach maximum efficiency once substrate bias voltage at −10V for the minimum threshold configuration as observed in mini-MALTA even with low n^- layer dopant density. The cluster size increases with the substrate voltage since depletion region depth increases and therefore electrical field strengthens within the pixels. One can see that behaviour at low threshold configuration.

The same measurement was done for the MALTA2 sample that has the same properties but it was exposed to 2×10^{15} 1 MeV n_{eq}/cm^2 NIEL dose. The Figure 3.41 shows pixel efficiency and average cluster size distributions as a function of the substrate voltage for the three threshold values ordering high, medium and low. As seen, the pixel efficiency performance was decreased by 20% for the lowest threshold configurations are compared to the previous measurement (see Figure 3.40). The reason for the drop is directly related to low n^- layer dopant density because depletion region width and uniformity depend on the dopant density of the silicon that is used in the detector. It seems that the MALTA2 EPI with a low n^- layer dopant density can stand the 1×10^{15} 1 MeV n_{eq}/cm^2 NIEL but it suffers efficiency loss once exposed to radiation increased to 2×10^{15} 1 MeV n_{eq}/cm^2 NIEL dose.

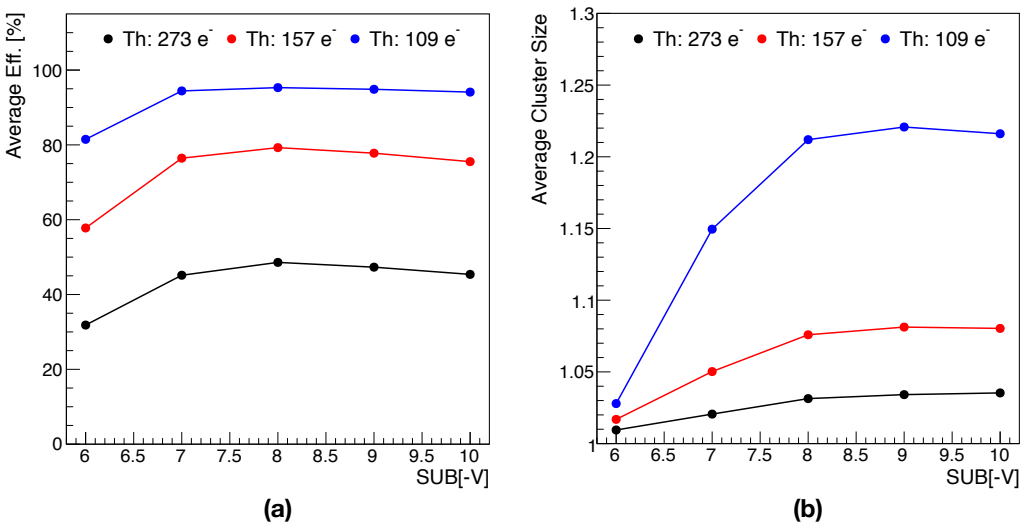

Figure 3.40. The obtained average pixel efficiency (a) and average cluster size (b) distributions of a 100 µm thick, extra-deep p-well pixel modification, low n^- layer doping density, and irradiated MALTA2 sample with 1×10^{15} 1 MeV n_{eq}/cm^2 NIEL as a function of applied substrate voltage for three different threshold values.

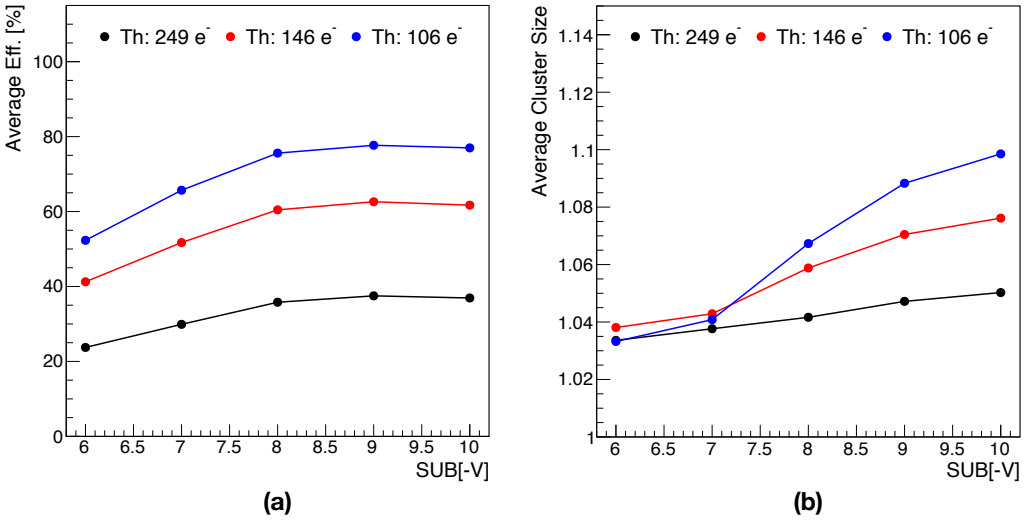

Figure 3.41. The obtained average pixel efficiency (a) and average cluster size (b) distributions of a 100 µm thick, extra-deep p-well pixel modification, low n^- layer doping density, and irradiated MALTA2 sample with 2×10^{15} 1 MeV n_{eq}/cm^2 NIEL as a function of applied substrate voltage for three different threshold values.

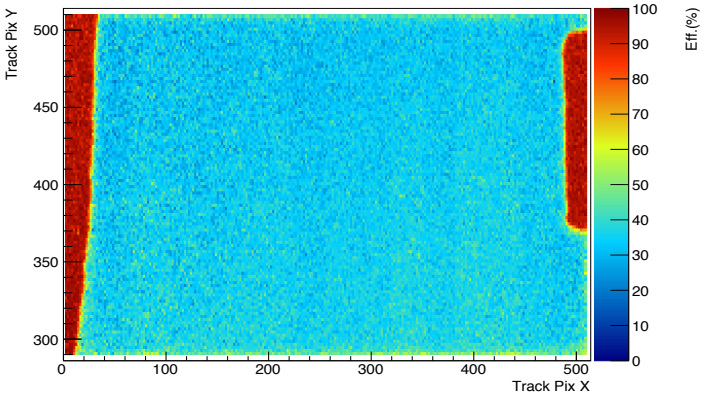

Figure 3.42. The pixel efficiency map of 100 µm thick, extra-deep p-well pixel modification, high n^- layer doping density MALTA2 sample and glue patterns on the pixel matrix.

Similarly, same measurements were performed for the MALTA2 Cz samples. However, large efficiency loss in the pixel matrix was observed due to the lack of depletion in pixels. It is expected to be related to the distribution of the substrate voltage as a result of the high resistivity of Cz silicon. Since MALTA Cz readout PCB have a smaller hole which is 1 cm × 1cm and conductive glue was applied to the corners of the sensor, this behaviour was not observed in the previous test beam measurements held in DESY. On the other hand, the MALTA2 chip sits up to 300 µm on the corners of the readout PCB and most of the backside is on the hole of PCB. As seen in Figure 3.42, only high efficiency can be achievable at the edges of the pixel matrix where conductive glue applied to place the sensor to readout PCB. This partially confirms the lack of depletion in the pixels due to the non-distribution of the substrate.

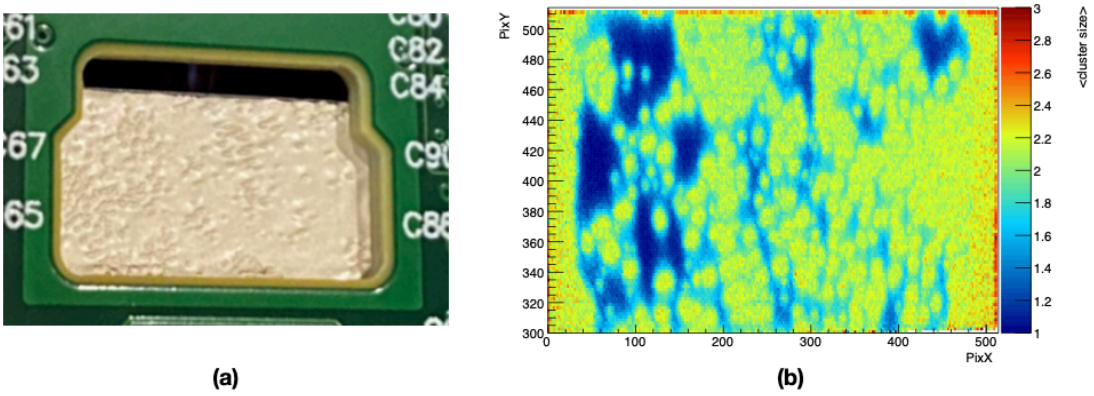

Figure 3.43. The backside of conductive glue applied MALTA2 Cz sample (a) and cluster size distribution (b) of that sample at −50 V substrate bias.

One way to prove this is to back metallization of the sample and repeat the measurement. Examples related to backside metallization of silicon sensors can be found in the literature, but it is a very sophisticated process and needs a serious attention (77). Thus, a very thin layer of conductive glue was applied with a soft brush to one of the irradiated MALTA2 Cz samples as a temporary solution. After glue application, the sample was annealed at 180°C for 2 minutes. The picture of applied glue (a) and cluster size distribution of pixel matrix (b) are shown in Figure 3.43. Since some bubble forms was occurred after conductive glue application, they negatively effected the power distribution on the pixels. As seen in Figure 3.43 (b), low cluster size distributions were observed around the bubble forms. Despite the bubble forms after conductive glue application to the backside of the sensor, the results are still better than the MALTA2 EPI samples for 2×10^{15} 1 MeV n_{eq}/cm^2 NIEL. The Figure 4.44 shows the average pixel efficiency and average cluster size distribution with respect to the applied substrate voltage for the MALTA2 Cz sample for three different threshold values. Similar to the previous MALTA Cz test beam results, it was observed that pixel efficiency and cluster sizes increase with applied substrate voltage as shown in Figure 3.44. At −50 V substrate bias, the average pixel efficiency of the pixel matrix reaches above 95% and the average cluster size is around 1.9 pixels.

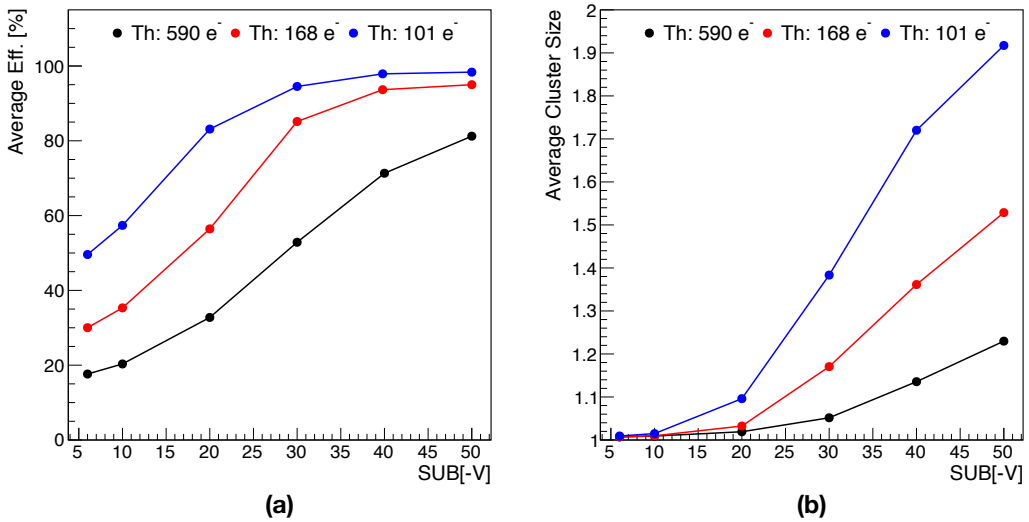

Figure 3.44. The obtained average pixel efficiency (a) and average cluster size (b) distributions of a 300 µm thick, n-gap pixel modification, intermediate n^- layer doping density, and irradiated MALTA2 sample with 2×10^{15} 1 MeV n_{eq}/cm^2 NIEL as a function of applied substrate voltage for three different threshold values.

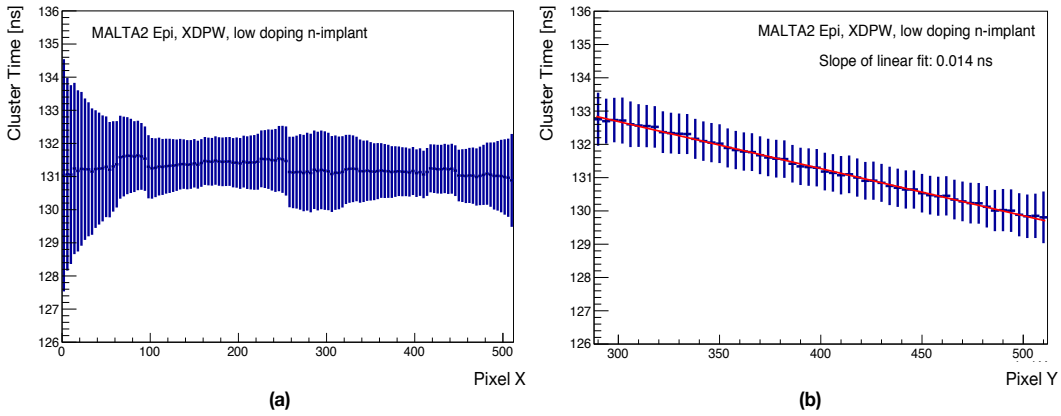

Figure 3.45. Time of the arrival of the leading hit in the cluster with respect to a scintillator reference along the column (a) and row (b) direction of the pixel of the matrix. Error bars indicate the corresponding RMS of the leading hit time. The unirradiated MALTA2 Cz is extra-deep p-well, 100 µm thick, with high doping of n-blanket and measurements were performed at −6 Vsubstrate bias. The threshold of the chip was around 170 e^-. The plots are adopted from (78).

Another important measurement, in-time efficiency performance, was made during the test-beam campaign of MALTA2 samples. The main aim of these measurements is to determine the in-time hit efficiency of MALTA2 pixels with respect to the different bunch crossing times. Therefore, the time resolution of MALTA2 samples and in-time efficiencies of pixels that depends on time resolution was observed for 4 different time windows. In the measurements, the arrival time of the leading signal of the hit in a pixel cluster was measured in a proper time window. Since time linearity exists along the column of the pixel matrix as discussed in laboratory measurements of MALTA2 samples, time measurements need to be corrected according to the linear behaviour. A similar non-uniformity exists along the row, and it has to be also corrected for the row. In Figure 3.45, the observed non-uniformities for both directions (*X* and *Y*) were measured with the arrival time of the signal of the hit in a pixel cluster. After the correlations were applied for both directions, the correlated arrival time distributions of the leading signal of the hit in a pixel cluster are shown for 100 µm thick MALTA2 EPI and Cz samples Figure 3.46. Both samples have time resolution below 2 ns including scintillator (~0.5 ns) and FPGA sampling ($3.125 / \sqrt{12} = 0.9$ ns) jitters.

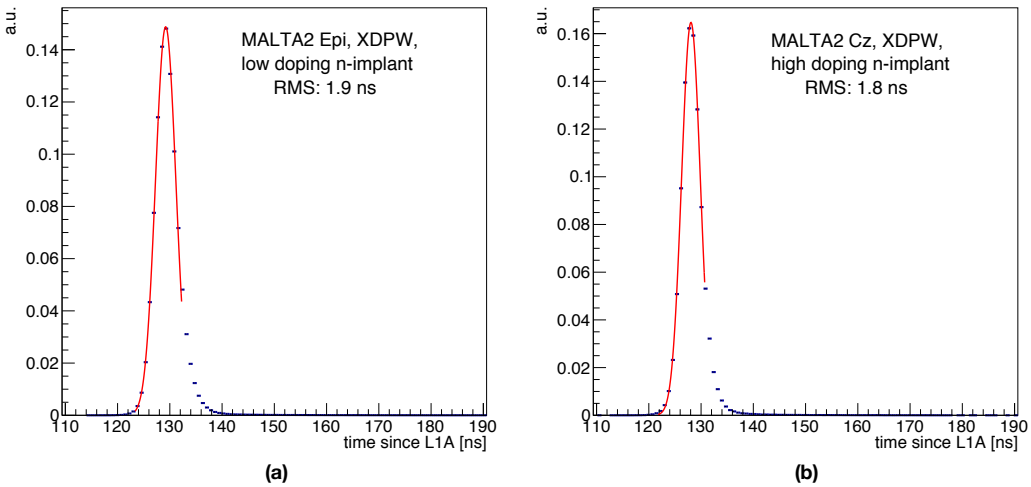

Figure 3.46. Time of arrival of leading hit in the cluster with respect to a scintillator reference for MALTA2 EPI (a) and Cz (b). The RMS value, both represented, corresponds to a Gaussian fit of the distribution. While the EPI sample has low doping of n-blanket, the Cz sample has high doping of n-blanket. The measurements were performed at −6 V substrate bias. The threshold of the chips was around 170 e^- and 130 e^- for Cz and EPI, respectively. The plots are adopted from (78).

The time resolution of the measurement can be formulated as:

$$\sigma^2_{time-resolution} = \sigma^2_{MALTA2} + \sigma^2_{Scint.} + \sigma^2_{Sampling} \tag{3.6}$$

where $\sigma_{time-resolution}$ is the obtained time resolution during the test beam measurements, σ_{MALTA} is actual time resolution of MALTA2 sensor, $\sigma_{Scint.}$ and $\sigma_{Sampling}$ are the scintillator and sampling jitter, respectively. The time resolution of the sensor can be found approximately by using Eq. 3.6. Nevertheless, the time resolution of the sensor (σ_{MALTA}) also depends on some internal parameters and the time resolution of the sensor can be represented with these parameters as follows:

$$\sigma^2_{MALTA2} = \sigma^2_{time\ walk} + \sigma^2_{Landau} + \sigma^2_{jitter} + \sigma^2_{TDC} \tag{3.7}$$

where $\sigma_{\text{time walk}}$ is the resolution of time walk contribution and σ_{Landau} represents the spatial time variation of the produced charges once the particle passes through the sensor (79). These two parameters are instrinsic parameters of the sensor. The other two parameters are related to the readout system of the sensor. The analogue front-end jitter is shown with σ_{jitter} and contribution of the time-to-digital

converter (TDC) of the sensor is represented as σ_{TDC}. In a nutshell, the actual time resolution of the MALTA2 sensor can be evaluated by using the Eq. 3.7.

Once the pile-up environment of the HL-LHC and the FCC-hh are taken into account, it becomes important to the determination of these parameters to mitigate pile-up particles by using the time and position-based 4D algorithms. Otherwise, it results in event loss due to the mistagging. The time resolution around 2 ns is not sufficient time resolution neither HL-LHC nor FCC-hh to reconstruct tracks properly, but it can be corrected by Eq. 3.6. The time-walk parameter depends on the collected charge and can be corrected by applying a threshold for a rough approximation. Also, it can be corrected in the integrated circuit within the pixel by correcting the time walk based on a time-over-threshold (TOT) on the time-of-arrival (TOA) which is a more common method. The jitter depends on noise value of the analogue front-end so it can be determined for given threshold settings. Thereby, its contribution to the time resolution also can be used to correct time resolution of the sensor. Besides, the σ_{TDC} is a fixed parameter and generally is around 3-5 ps as seen in PicoTDC. Among these parameters, however, the σ_{Landau} cannot be determined like time-walk or it cannot be assumed constant number like σ_{TDC}. Due to the non-homogenous energy deposition of a particle in pixel, charges are produced in different depths and collected via drift at different times. Therefore, it cannot be evaluated with direct measurement. It basically determines the time resolution limits of the sensor.

The time resolution of the MALTA2 sensor is roughly evaluated for high doped Cz sample as an example. Before the correction, the MALTA2 resolution was calculated with Eq. 3.6 to discard scintillation and sampling jitters. The time resolution is then corrected for the 200 e^- using the Eq. 3.7, where the $\sigma_{time\ walk}$ value is around 1.4 ns (see Figure 3.35(b)). Since the FCC-hh bunch crossing time is 25 ns, MALTA2 reaches that value 25 ns at 200 e^- (see Figure 3.35(a)). The σ_{jitter} resolution is around 280 ps (see Figure 3.37) and σ_{TDC} value is taken as 3 ps for the calculation. As a result of the correction, it was found around ~350 ps time resolution. However, this is a very rough approximation result obtained by applying cut on time-walk resolution distribution and therefore, it requires detailed study. The contribution of $\sigma_{time\ walk}$ on time resolution has to be corrected via TOT and TOA values to obtain more accurate results.

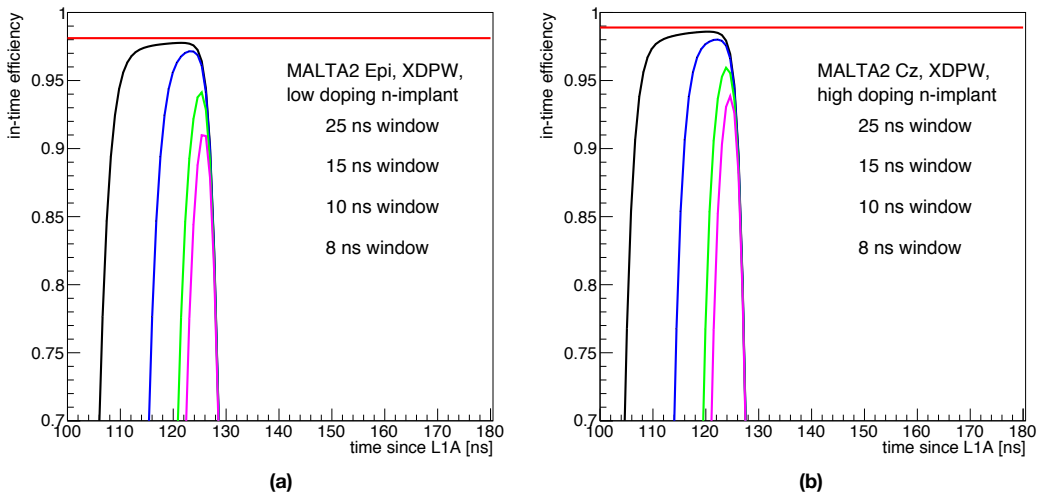

Figure 3.47. The in-time efficiencies of MALTA2 EPI (a) and Cz (b) samples for four different time windows. Both MALTA2 samples are 100 µm thick and have extra-deep p-well pixel modification. While the EPI sample has low doping of n-blanket, the Cz sample has high doping of n-blanket. The measurements were performed at −6 V substrate bias. The threshold of the chips was around 170 e^- and 130 e^- for Cz and EPI, respectively. The plots are taken from (78).

In addition to the correction of time resolution, the taken data was analyzed considering 4 different time windows 25, 15, 10 and 8 ns, respectively. The in-time efficiencies with respect to the arrival time of the leading signal of the hit in a pixel cluster are shown for these time windows in Figure 3.47. It can be seen that in-time efficiencies can be reached at around 98% in a time window of 25 ns for both samples, but it is obvious that the MALTA Cz sample has better performance at 8 ns time window. In order to observe time loss in pixels, an in-time map of 2 × 2 pixel matrix which considers the time difference between the arrival time of the leading hit in the cluster and the average leading time of signals from all pixels was obtained for the same MALTA2 samples. Thereby, the time evolution of the pixels with respect to the reconstructed track position was determined as seen in Figure 3.48. Taking into account the position of the track, the time difference between the arrival time of the lead hit in the cluster and the mean propagation time of the signals is high at the corner of the pixels, with no difference in Cz or EPI silicon. Since the charge sharing between pixels is high once a particle passes through at the edges of pixels, a time walk occurs in the front-end due to low charge. Therefore, there is a large time difference between center of the pixel and the corner of the pixels as seen

in the Figure 3.48. This also explains the 8% drop in-time efficiency in 8 ns time window.

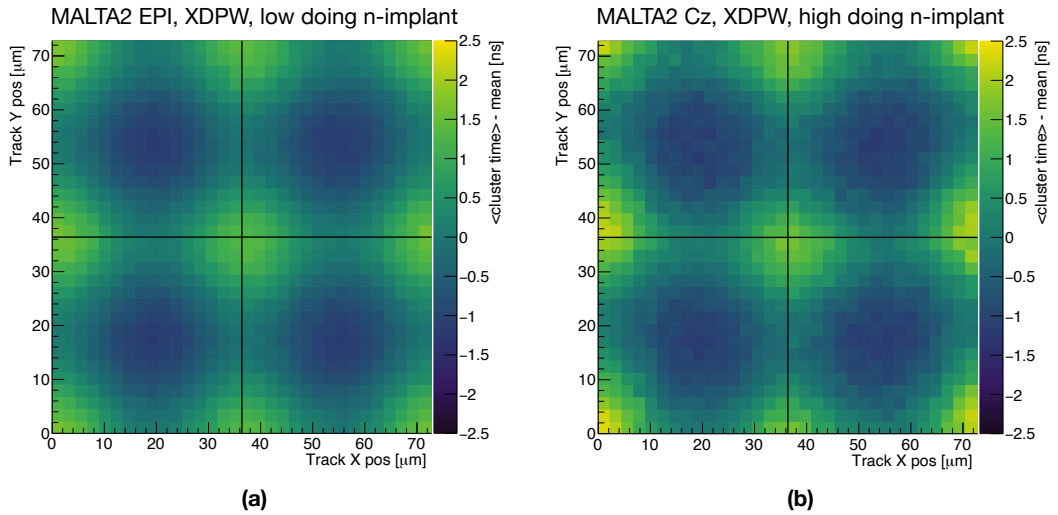

Figure 3.48. The in-time 2 × 2 pixel matrix of MALTA2 (a) EPI and (b) Cz samples. Colour scale indicates the difference in timing of the leading hit in the cluster and the average timing over the entire matrix. Both MALTA2 samples are 100 μm thick and have extra-deep p-well pixel modification. While the EPI sample has low doping of n-blanket, the Cz sample has high doping of n-blanket. The measurements were performed at −6 V substrate bias. The threshold of the chips was around 170 e^- and 130 e^- for Cz and EPI, respectively. The figures are reproduced from (78).

As a result of the test beam measurements, the performance of the MALTA2 samples shows that the improvements in the front-end effects the hit efficiency. This can be seen in the MALTA2 EPI samples with low dose n-layer implementation which is applied lower dopant level than the first MALTA samples. Samples have over 95% hit efficiency for 1×10^{15} 1 MeV n_{eq}/cm^2 NIEL dose at the low threshold configuration. However, low dose n-layer implementation drops to below 80% for 2×10^{15} 1 MeV n_{eq}/cm^2 NIEL dose. It is expected to give better performance in intermediate dopant levels for that radiation dose. Even though power distribution issue on the pixel matrix for the MALTA2 Cz sample, the test beam results show that hit performance over 97% is achievable for 3×10^{15} 1 MeV n_{eq}/cm^2 NIEL dose if overcome to power distribution through the pixel matrix. In addition to the hit efficiencies, the in-time efficiencies of samples are around 98% for the 25 ns window which is the bunch crossing time of LHC, HL-LHC and even FCC-hh. As observed in time walk measurements at laboratory, the MALTA2 front-end responds fast with respect to the collected charge amount. This behaviour

related to time walk was directly noticed once particle passes through the corners of the pixels.

3.5 Summary of MALTA Sensors

The development process of MALTA sensors is described in detail in the chapter. In the development process, not only different types of high resistivity silicon were used in the production but also modified pixel designs were applied to improve the radiation tolerance of the sensor. In addition, the analogue front-end design was modified to operate pixels at the low threshold and noise values by adding and enlarging transistors. Thereby, radiation-related efficiency drops were aimed to prevent by controlling chips at the low threshold settings. Thanks to its structure openness to development, the radiation tolerance of MALTA sensors was improved after laboratory and test beam measurement results. The latest version is reached the desired radiation limits of HL-LHC with high in-pixel and in-time hit efficiency. Even though it is developed for HL-LHC upgrades of the Pixel Detector of ATLAS Inner Tracker, properties of MALTA such as small collection electrode pixel structure, pixel pitch size, thickness and novel asynchronous read-out architecture are promising for future experiments like FCC-ee and FCC-hh. However, some crucial improvements are still required for the FCC-hh detector.

The first one of these and the most important is radiation hardness at ultimate luminosity. The NIEL radiation limit at the inner tracker (barrel) of the FCC-hh is around 6×10^{17} 1 MeV n_{eq}/cm^2 NIEL dose and this is 300 times larger than the current limits of the MALTA2. It is also the same for TID, and it is far from the FCC's desired limits. The expected radiation TID level is 30 Grad, and this dose is 300 times larger than MALTA2 limits which is 500 Mrad. These levels can be achievable by finding optimum dopant levels of the pixel design for Cz silicon. It is expected that the noise ratio in the front-end increases due to the radiation. This results in new analogue and digital and front-end design requirements. During the development process, some transistors were added and some transistors were enlarged to overcome radiation-related noise in MALTA sensors. In such a demanding radiation environment, 180 nm CMOS technology may not be sufficient especially pixel pitch size considered. Therefore, production with smaller CMOS technologies like 65 nm can be needed. The thickness of the sensor is also an important parameter in terms of less material cost as discussed in FCC section. The

thickness of MALTA is thinned from 300 μm to 100 μm in the current MALTA2 design and it is pretty enough for the FCC-hh tracker in terms of the low material cost.

Another important requirement for FCC-hh is the improvement in the time resolution of the sensor. The in-time efficiency of MALTA2 sensors meets perfectly with demanding of the FCC-hh but the time resolution of the MALTA sensor is still below the desired time resolution. The pile-up event size per collision requires good position measurement as well as near perfect time measurement to reconstruct not only tracks but also vertices. However, the improvement in the time resolution is a challenging process and it depends on many other parameters. The actual time resolution of the sensor can be determined and can be correlated once the parameters are determined well. Even if correlated with the other contributions, the sensor itself has a large time resolution and the MALTA2 sensor has a 10 times larger time resolution than the FCC-hh limits. Since the produced charges after incoming particles are collected via drift, the electric field inside the sensor has crucial importance for time measurements. Therefore, the dopant levels, pixel design and silicon type, EPI or Cz, become determinants in the time resolution. In order to achieve good time resolution such as 30 ps, these modifications need to be applied to the next generation MALTA sensors increasing the radiation hardness.

4. SIMULATION OF FCC-HH TRACKER TIMING PERFOMANCE WITH A PHYSICS PROCESS

Many phenomenological physics studies were done at 100 TeV including FCC-hh baseline detector effects and those can be found in the literature. They clearly show why FCC-hh is necessary for physics searches. In the reality, simulation studies will not be easy because the pile-up events are not taken into account to measure the signal strength of the physics study under test. These pile-up events require detailed understanding and study to unveil rare physics events. For this reason, the tracker system of FCC-hh detector may take a fundamental role in determining the pile-up vertices in the collision by reconstructing tracks with high resolution. As mentioned in the Chapter 1, the tracker will consist of innermost, intermediate and outermost regions. In the innermost region, CMOS pixel sensors with a small pitch size (30-50 μm) are planned in barrel layers for high resolution. The MALTA sensor, which has not only a small pixel pitch size and in-time resolution but also an asynchronous readout system, stands out for future experiments. Indeed, radiation levels of the tracker of the FCC-hh detector are higher than the current radiation limits of the MALTA sensor. Also, time resolution of the MALTA sensor is around 350 ps and it is very high for the proper tracking when the high pile-up environment of the FCC-hh is considered. This value can be problematic for the reconstruction of vertices from detected tracks in the innermost layer. Hence, the time resolution limit of the MALTA sensor is needed to be tested for FCC-hh pile-up environment.

In this section of the thesis, the validation of the MALTA sensor for the FCC-hh tracker system will be tested under pile-up environment with a benchmark physics process that is one of the rare physics events, Higgs self-coupling ($gg \rightarrow HH \rightarrow b\bar{b}\gamma\gamma$) process. It will be simulated in DELPHES including ideal detector effects of FCC-hh detector.

4.1 Overview of DELPHES and FCC-hh Detector Card

The Monte-Carlo event generation techniques are commonly used in high energy physics experiments to optimize detector components or analysis strategies. Some of the Monte-Carlo methods can be sophisticated depending on the experiment or physics analysis. The large detector geometries and the complexity

of the detector components make it hard the description of the Monte-Carlo method. In the case of the large experiments like ATLAS and CMS, the effort for computing increases and require expertise in coding to describe the detector environment in a realistic way. Interactions of particles with matter in complex detector geometries also slow down the simulation in high particle flows. Therefore, a full simulation of a simple physics event can require a lot of computing power. In the reality, Monte-Carlo simulators such as GEANT4 (28) can perfectly simulate the environment of high energy physics experiments, thus being usually preferred by large collaborations. This creates a demand for fast and user-friendly Monte-Carlo simulations. At this point, the DELPHES framework (80–82) was developed to meet this need in high energy physics experiments. It has been demonstrated to be a simple, fast, and realistic tool for high-energy physics experiments. It is based on modular structure so the event generation, realistic detector effects and particle identification algorithms are defined as modules. These modules do not contain complex detector geometries or probability distributions of physics processes (physics lists) like in GEANT4. In the modules, the properties of the particles such as momentum, position and time are smeared with respect to a detector resolution distribution that can be obtained, for instance, from the technical design report of the ATLAS or CMS experiments. These resolution parameters are implemented into the DELPHES modules or can be read from configuration files. In this way, the truth (generator) values of the particles are smeared. Users also can write their own modules in C++ programming language that can be run in DELPHES easily.

As mentioned, DELPHES does not contain any physics list. Therefore, it requires simulated particles after the collision as an input. The output of the event generator like PHYTIA8 (29,83) is an excellent choice, since it simulates physics theories and models including particle interactions, decays, parton distributions, initial and final state parton showers. The output of PHYTIA8 can be saved in different formats. The most commons are Les Houches Event File (LHEF) and HepMC (84,85). These formats are supported by reader modules in DELPHES. Likewise, the pile-up events produced with PHYTIA8 can also be incorporated with the input data in a module that combines the pile-up and physics data as vertices. The block diagram of DELPHES is shown in Figure 4.1. Each block represents a module that runs special algorithm related to the detector or reconstruction of particles.

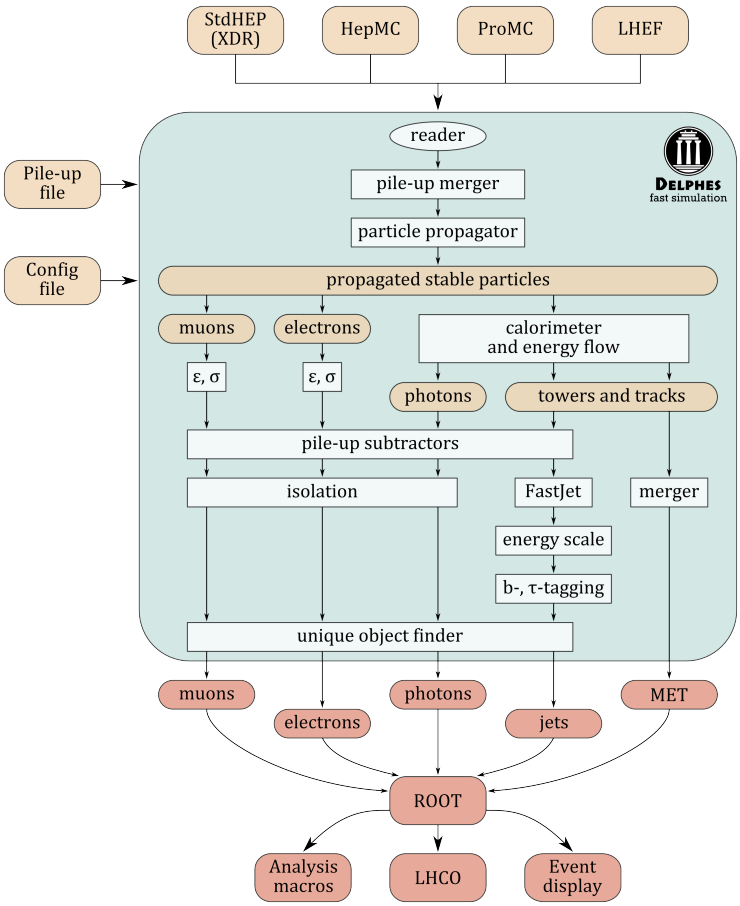

Figure 4.1. Block diagram of the different modules in DELPHES. The figure is taken from (80).

In order to control the flow of inputs and outputs between the modules for a specific detector, a configuration file known as a detector card is needed in DELPHES. This card can be defined by users or pre-defined detector cards of some collaborations such as ATLAS, CMS and FCC can be used. The detector card lines up the modules to be used at each step as shown in Figure 4.1. Input particles produced with PHYTIA8 follow the reconstruction order of the detector card. As a result, the output particles are reconstructed with realistic detector effects and are used for physics objects by applying some algorithms like isolation, tagging and FastJet (86). The simulation output which consists of final state particles such as photons, muons, jets etc. is written to a ROOT (87) file for offline analysis. In conclusion, DELPHES allows the production of desired physics process in a simple and fast way including realistic detector effects.

The FCC-hh baseline detector and the performance of its subsystems are detailed in Chapter 2. The full simulation of the detector has done by the GEANT4 and the performance of the subsystems is parametrized to be used in DELPHES. These parametrized variables such as momentum resolution of tracker and photon energy resolution of electromagnetic calorimeter are implemented into the FCC-hh detector card (88) . However, the current FCC-hh baseline card is developed for phenomenological physics studies which include realistic detector effects on the physics process. Even though some of the defined detector cards, especially for HL-LHC, in DELPHES include detector effects and pile-up events, this is not eligible for the FCC-hh. The main reason is that the high energy physics community focus on the signal strengths of physics theories at 100 TeV, including FCC-hh detector effects, to determine the importance of the FCC-hh project in terms of physics. Moreover, track reconstruction, vertex finding and pile-up subtraction algorithms are still being studied for HL-LHC pile-up environment, not for the FCC-hh project. Nevertheless, the initial stage of the FCC-hh project is expected to have almost similar pile-up environment and algorithms developed for the HL-LHC not only can be used for the initial luminosity but also test for the nominal luminosity environment of the FCC-hh baseline detector. Since properties and resolution values of the detector components are discussed in the introduction section, hence will not be discussed in this section. All properties and resolution values of detector components are already implemented in the FCC-hh baseline detector card. In addition, algorithms that are developed for reconstruction of the vertices is implemented into DELPHES as modules. The vertex reconstruction module searches tracks and determines the vertices that tracks belong. In following section, the deterministic annealing algorithm for vertex finding will be detailed briefly.

4.2 Deterministic Annealing Algorithm for Vertex Finding

The pile-up with a simple definition is number of particle interactions per bunch-crossing and average number of these events depends on the collider properties and center-of-mass energy. Average pile-up size per bunch-crossing can be calculated with the following formula;

$$< \mu > \; = \; \frac{\sigma_{in.\,el.} L}{n_b f_r} \qquad (4.1)$$

where $\sigma_{in.el.}$ is cross-section of inelastic collisions at center-of-mass energy, L denotes the instantaneous luminosity of collider, n_b stands for number of particles in bunch and f_r is revolution frequency of the collider. Taking n_b, $\sigma_{in.el.}$ and f_r parameters constant, two different mean pile-up event sizes are calculated as $<\mu>$ = 200 and $<\mu>$ = 1000 for two different, 5 ab^{-1} and 30 ab^{-1}, luminosity options at 100 TeV center-of-mass energy, respectively. Basically, it is planned that the collider is operated with different instantaneous luminosity options for each integrated luminosity option. The simulated pile-up environment after a collision is shown for two different pile-up scenarios in Figure 4.2.

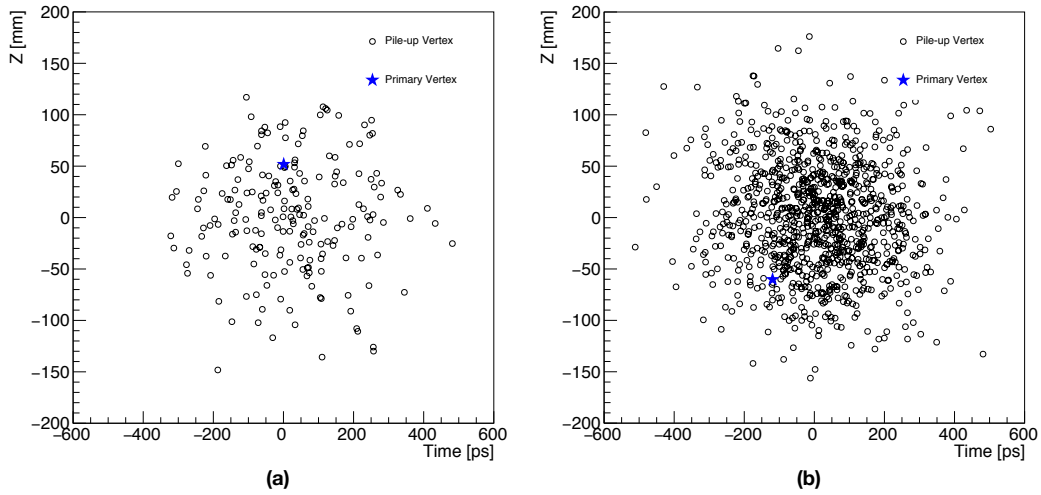

Figure 4.2. The mean pile-up environment of the FCC-hh is shown with 200 and 1000 generated vertices on the position and time plane for 5 ab^{-1} and 30 ab^{-1} luminosity, respectively. The pile-up vertices are represented with black dots and the hard vertex that contains the real physics event is plotted with a blue star.

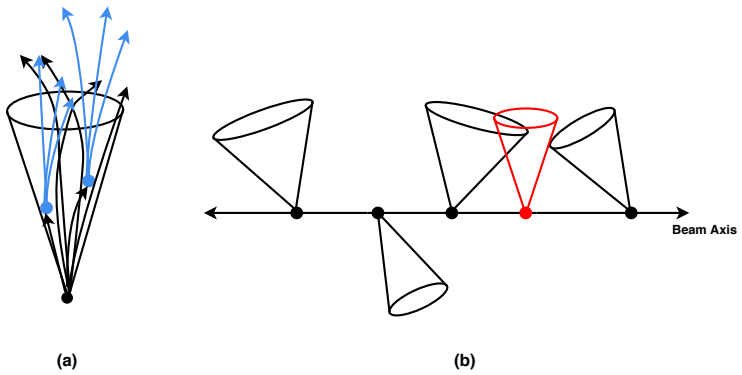

Figure 4.3. (a) Illustration of a jet cone with charged and neutral particles produced inside it. (b) Produced vertices on the beam axis and their jets. The black dots and cones represent the pile-up vertices and jest, respectively. The red dot is the hard vertex that contains the real physics event, and the red cone is its jet.

These pile-up events are the product of strong interactions, and as a result of interactions, the flow of charged and neutral hadrons in a shape of narrow cone known as jets is observed in the detector. As the mean pile-up increases, the jet number per collision explodes in the environment dramatically. A jet (a) and jet production on the beam axis (b) are illustrated for hard and pile-up vertices in Figure 4.3. Therefore, determining the initial position of each pile-up event, the vertex, at the beamline becomes crucial for physics studies. More accurate physics research can be done only after the reconstructions of the vertices are made using charged particles in the environment. Many effective algorithms for vertex reconstruction can be found in the literature. In these algorithms, vertices are reconstructed using initial position and time information particles but different mathematical approaches. Among these algorithms, the Deterministic Annealing (DA) algorithm (89,90), has good performance in vertex determination and is validated with CMS data. As it can be understood from its name, the DA algorithm is a kind of annealing procedure like a thermodynamic process in which a solid is heated to its melting point. This breaks the bond between atoms and dislocates them. Then, a decrease in the temperature starts to locate atoms to previous positions in the material. This process is known as annealing, and it continues till the equilibrium state of the material. As a result of the process, a material that can be bent more easily is obtained. If we consider the particles generated in the collisions as dislocated atoms in the material example, a similar approach can be defined for the remnants, tracks, of produced vertices distribute in the detector. Using the statistical mechanics, a system can be described for given conditions by defining proper thermodynamical equations. Then, using the particles in the system after collisions, the defined system can be annealed to the equilibrium state to find their vertex positions.

The DA algorithm basically evaluates the vertex position using initial position and initial time information of particles that are obtained with the closest approach to beam axis. Therefore, it does not reconstruct secondary vertices that form inside the jets. As described in refence (90), the algorithm defines a partition function for the statistical properties of the system as follows;

$$Z_i = \rho e^{-\beta \mu^2} + \sum_{k=1}^{n} e^{-\beta E_{ik}} \tag{4.2}$$

where ρ and μ are used as free parameters to gauge the outlier rejection of the system. The μ parameter is simply the number of standard deviations of the track to determine an outlier for a given vertex prototype and it is fixed to 4. The parameter ρ is fixed to zero in the beginning, then increased to 1 in small steps at the end of the annealing cycle to enable outlier rejection quasi-adiabatic. The temperature of the system is defined as $\beta = 1/T$. The energy of the system is defined as a relation between the tracks and the vertex prototypes as it follows;

$$E_{ik} = \frac{(t_i - t_v^k)^2}{\sigma_{t,i}^2} + \frac{(z_i - z_v^k)^2}{\sigma_{z,i}^2} \tag{4.3}$$

where t_v^k and z_v^k are time and position of the vertices. While the z_i and t_i are the time and position of tracks, σ_t and σ_z denote the uncertainties on the time and position, respectively. Tracks are weighted with the track impact parameter (d_0) within standard deviation (S_0=1) in the reconstruction process to penalize particles which have high impact parameter. The weighting formula can be written as;

$$w = \frac{1}{1 - e^{\left(\frac{d_0}{\sigma_{d_0}}\right)^2 - S_0}} \tag{4.4}$$

Then, the vertex prototype time value can be computed for the definition of $p(k,i) = p_k e^{-\beta E_{ik}} Z^{-1}$ and $p_k = \sum_i w_i p(k,i) / \sum_i w_i$ with the equation as follows;

$$t_v^k = \left(\sum_i \frac{p(k,i) w_i}{\sigma_{t,i}^2} t_i \right) \Bigg/ \left(\sum_i \frac{p(k,i) w_i}{\sigma_{t,i}^2} \right) \tag{4.5}$$

with similar approach vertex prototype position z_v^k also can be calculated. Using the relations;

$$p(i,k) = \frac{w_i p(k,i)}{p_k} \tag{4.6}$$

$$w_{tz}^{i,k} = \frac{p(i,k)}{\sigma_{t,i}\sigma_{z,i}} \tag{4.7}$$

and vertex covariance matrix, C_{tz}^k, is the following;

$$C_{tz}^{k} = \frac{\sum_i w_{tz}^{i,k}(t_i - t_v^k)(z_i - z_v^k)}{\sum_i w_{tz}^{i,k}} \tag{4.8}$$

The annealing loop over from $\beta = +\infty$ till the critical temperature β_s. The first vertex prototype is computed at β_0 for the system. Once β_0 is computed, the system cooled down to find particle clusters using particles in the system. From slightly above β_0, the annealing loop runs until $\beta_s = 0.2$ to find and update vertex positions for the following requirement;

$$\left(\frac{\Delta t_v^k}{\sigma_v^t}\right)^2 + \left(\frac{\Delta z_v^k}{\sigma_v^z}\right)^2 \leq 0.5 \tag{4.8}$$

in which Δ corresponds the variation in the update cycle for given normalization σ_v^t and σ_v^z factors. The normalization factors (σ_v^t and σ_v^z) basically determine the resolution of the reconstructed vertex. If the distance between two vertices in the system is less than 2σ, they are considered unsolvable. As a result, prototypes with a normalized distance of less than 2 are combined and the cycle is updated. Then, the temperature of the system is cooled down with a factor of 0.8 to keep process quasi-adiabatic. If the reconstructed vertex is valid, satisfying the Eq. 4.8 and distance between two vertices in the system is more than 2σ, it bisects along the direction of the maximum eigenvalue. Then, the temperature of the system is cooled down again with a factor of 0.8. The follow diagram of update cycle is shown in Figure 4.4.

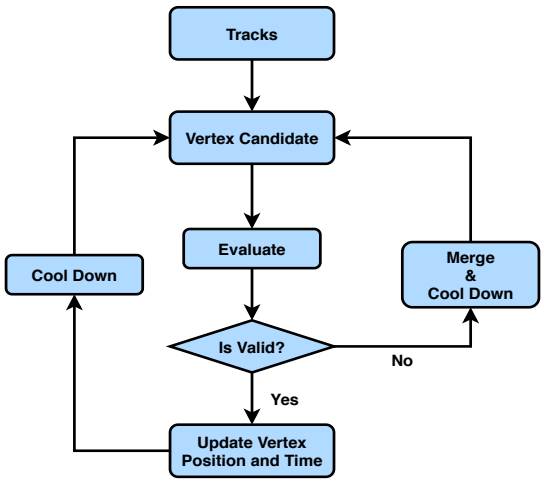

Figure 4.4. Update cycle of deterministic annealing

At the end of annealing loop, $\beta_s = 0.2$, purging loop starts to remove vertices which have tracks less than two. After that, whole procedure is repeated but cooling down to system till $\beta_p = 1$. In order to sharpen the borders of the clusters, the ultimate cooling procedure runs again till the system temperature of $\beta_M = 1.5$. After this process, selected tracks are marked with vertex indices to point out which vertex belongs. As an example, the reconstruction loop of two vertices, a pile-up and a hard, is shown in Figure 4.5. The first vertex position is determined for the system at β_0 as seen in Figure 4.5 (a) where the vertex does not match any other candidates. After that, the algorithm updates the position vertex and reconstruct new vertices till the β_s where all possible clusters consider as vertex candidate. Although two real vertices are tested from the system, there are 6 possible vertex candidates reconstructed at β_s as shown in Figure 4.5 (b). The main reason of this is remnants of secondary vertices. These secondary vertices have same position but their time is later than actual vertex. Hence, these secondary vertices are already cleaned from the system at β_p and β_M as mentioned.

The algorithm is already tested for HL-LHC performance of CMS and it is embedded into DELPHES as a module (91). In the study, the initial time values of tracks are calculated for given time-of-flight resolution and momentum values applying the closest approach to the pion mass (comprises the majority of charged particles in LHC). Then, the calculated initial time value and the longitudinal impact parameter of the tracks, which defines the closest position of the track to the beam spot, are given as position and time values of the track to the algorithm. On the other hand, this thesis focuses on the time-resolution importance of the FCC-hh inner tracker for different pile-up scenarios. Therefore, the initial time of tracks, which are already known thanks to the Monte Carlo simulation, are smeared for 3, 30, 100 and 300 ps time resolution instead of the closest approach for the initial time of tracks. In this study, these smeared initial time values and track impact parameters are given to the DA algorithm. Thereby, it is aimed to determine the effect of time resolution on vertex reconstruction for tracks around the inner tracker.

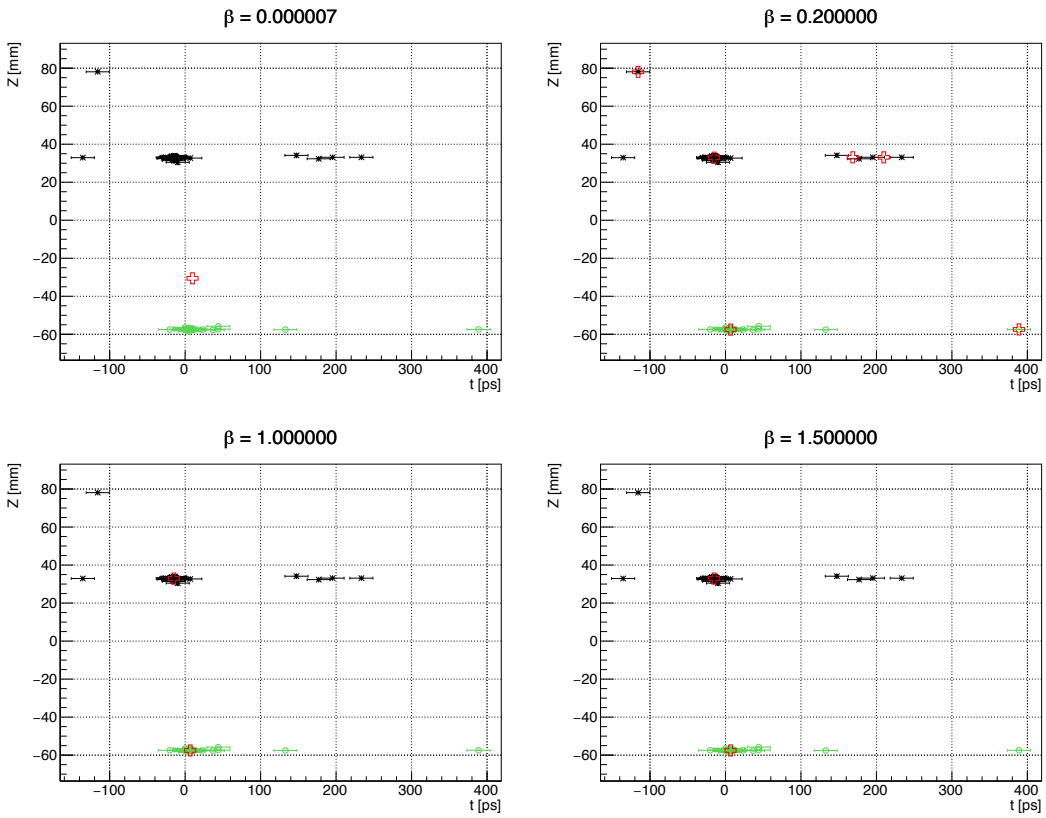

Figure 4.5. Performance of deterministic annealing algorithm cycles (β_0, β_s, β_p and β_M, respectively) is obtained for two vertices. While the black colour dots are tracks of pile-up vertex, the green ones are for hard vertex which are the truth tracks of two b-jets from the Higgs boson. The cross marker indicates the position and time of the vertex candidate at that temperature.

4.3 Benchmark Physics Process: Higgs Self-coupling

In order to determine the required timing performance of the inner tracker system of the FCC-hh detector, a benchmark physics process was chosen and tested under different pile-up scenarios with the DELPHES framework. As a physics process, Higgs self-coupling, is chosen for the benchmark physics process. It is a very rare phenomenon and immense amount of data is needed for accurate measurement. This increases the importance of high luminosity experiments at high center-of-mass energies. Recent phenomenological studies show that it can be measured with a high precision at high confidence level in FCC-hh. Therefore, it is important to test the timing performance of the inner tracker system of the FCC-hh detector under different pile-up scenarios for such a rare phenomenon.

The Standard Model basically describes the fundamental components of matter and their interactions. The mass generation in the model is explained with Brout-Englert-Higgs (BEH) mechanism. The BEH mechanism introduces a new

field, known as the Higgs field, and it explains why weak bosons (W^+, W^- and Z) have a massive and photons are massless. As discovered by the ATLAS and CMS collaborations in 2012, this field produces a Higgs boson once excited. According to the BEH mechanism, a single Higgs boson also interacts with the Higgs field and produces two Higgs bosons. This process is known as the Higgs self-coupling and it can be shown with the following expression, once Higgs potential is perturbed around its minimum;

$$\mathcal{L}_h = \frac{1}{2} m_H^2 H^2 + \lambda_3 H^3 + \lambda_4 H^4 \tag{4.9}$$

where Higgs mass is corresponds the m_H, and trilinear and quadraditic Higgs couplings are repesented with λ_3 and λ_4,respectively. The self-couplings in the SM are prediced to be $\lambda_3^{SM} = m_H^2/2$ and $\lambda_4^{SM} = m_H^2/8\upsilon^2$ in which υ is the vacuum expectation value of the Higgs field and it is evaluated as $\upsilon = \left(\sqrt{2}G_F\right)^2 = 246\ \text{GeV}$ using its relation with the Fermi constant. The BSM models can also be measured with $\kappa_\lambda = \lambda_3/\lambda_3^{SM}$ relation. The observation of any Higgs pairs (HH) does not mean the measurement Higgs self-coupling because the Higgs pairs can be produced via gluon fusion (ggHH), vector boson fusion (VBF HH), associated production with top pairs ($t\bar{t}$HH) and double Higgs-strahlung (VHH) as represented in Figure 4.6. As seen in the diagrams, either Higgs pair production or Higgs pair production with trilinear Higgs self-coupling have same final state. Therefore, the precise measurement of κ_λ is crucial for the Higgs self-coupling to discriminate Higgs pair production and trilinear Higgs self-couplings. Each production process has an individual cross section values depending on the production and the center-of-mass energy as shown in Table 4.1. The cross sections of the HH productions are shown in Table 4.1 at 14 TeV and 100 TeV center-of-mass energies for $\kappa_\lambda = 1$.

Table 4.1. The calculated cross sections of the HH productions at 14 TeV and 100 TeV center-of-mass energies for $\kappa_\lambda = 1$ including QCD corrections. The cross section of double Higgs-strahlungs (W^-HH, W^+HH and ZHH) are represented as one in VHH. The values in table are adopted from (92) and calculation procedure of cross sections is described in (93).

Process	σ (fb) @ 14 TeV	σ (fb) @ 100 TeV	Accuracy
ggHH	36.69 ± 5.3	1224 ± 5.6	$NNLO_{FTapprox}$
VBF HH	2.05 ± 2.1	82.8 ± 2.1	N^3LO
$t\bar{t}HH$	0.949 ± 2.9	82.1 ± 7.8	NLO
VHH	0.982 ± 1.8	16.23 ± 2.9	NNLO

As seen in Table 4.1, the ggHH has the highest cross section among the other productions. Therefore, it was chosen as a signal in this study even though the study does not measure the sensitivity of coupling. However, the final state of the Higgs is important to measure performance of tracker time resolution under high pile-up scenarios. As described in reference (92), the most promising decay channels are $HH \rightarrow b\bar{b}\gamma\gamma$, $HH \rightarrow b\bar{b}b\bar{b}$ and $HH \rightarrow b\bar{b}\tau\tau$. Under large pile-up events, it becomes hard to reconstruct jets and it requires extra algorithms for the mitigation of pile-up particles from the jets even if the vertex position on the beam axis is correctly determined (see Figure 4.3 (b)). Therefore, $HH \rightarrow b\bar{b}b\bar{b}$ and $HH \rightarrow b\bar{b}\tau\tau$ are not suitable to see effects on the reconstructed Higgs masses. On the other hand, the $HH \rightarrow b\bar{b}\gamma\gamma$ decay channel is a good candidate to be used as a signal for this study. Since one of Higgs decays to two b-jets, vertex position can be found using the charged hadrons within the jets. In short, the decay of $H \rightarrow b\bar{b}$ can test the time performance of the inner tracker in the vertex and mass reconstruction. Moreover, Higgs mass can be reconstructed precisely with two prompt photons because pile-up events contain mostly QCD jets which consist of low energetic photons by their structure.

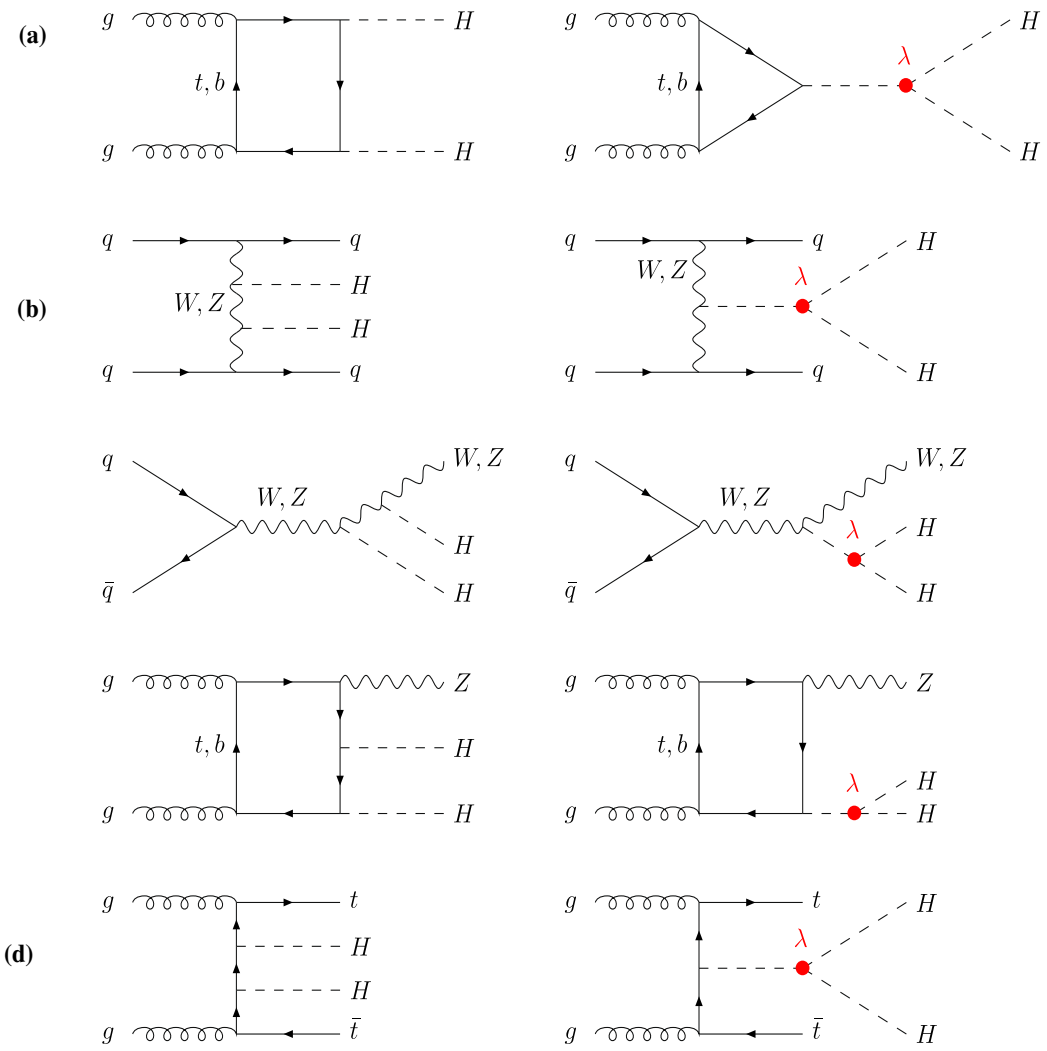

Figure 4.6. Feynman Diagrams of double Higgs productions with gluon fusion (ggHH), vector boson fusion (VBF HH), associated production with top pairs (tt̄HH) and double Higgs-strahlung (VHH) are shown on the left side. The diagrams of trilinear Higgs self-couplings are shown on the right side with a red colour.

In the simulation of the Higgs self-coupling with $HH \rightarrow b\bar{b}\gamma\gamma$ channel, MADGRAPH5_aMC@NLO Monte Carlo event generator (94) is used to produce signal events with next-to-leading order (NLO) corrections for $\kappa_\lambda = 1$ at 100 TeV center-of-mass energy. In the signal generation, the NNPDF3.0 set from LHAPDF tool is used as a parton-distribution (PDF) function. After that, parton-level events of signal data are evaluated with PHYTIA8 considering initial and final-state radiation, hadronization and underlying event. The pile-up events are also produced with PHYTIA8 pile-up event generator which produces the most probable QCD events for a given energy. The generated signal and pile-up data are given to

DELPHES to simulate realistic detector effects of the FCC-hh detector. In the DELPHES simulation, the FCC-hh detector card is used for the study. However, some modification is made on the detector card. These changes are user-defined parameters and implementation of the modules for the vertex finder, time-smearing and pile-up subtractor.

First of all, FCC-hh has two luminosity of options and it is expected two different pile-up scenarious for each option as mentioned in Section 4.2. Yet, the data is produced for 3 different mean pile-up scenarios, $<\mu>$ = 200, $<\mu>$ = 500 and $<\mu>$ = 1000, to see evolution of time resolution and pile-up effects on vertex reconstruction and Higgs masses. In the generation, a signal and pile-up events are distributed in the beam spot with the resolution of σ_t =160 ps and σ_z = 55 mm as Gaussian distribution (see Figure 4.2). In reality, charged particles can be only reconstructed with hit information from the tracker layers using algorithms like Kalman-Filter (95). However, DELPHES is not a full simulation, and it is not possible to reconstruct charged particles in that way. In order to realistically study, it is assumed that all charged particles are reconstructed well for p_T > 1 GeV within $|\eta|$ < 5. The initial time values of the charged particles are smeared for 3 ps, 30 ps, 100 ps and 300 ps time resolution values, seperately to determine limits of tracker on vertex finding. After that, the initial time and the longitudinal impact parameter of the tracks, t_i and z_d, are used in the reconstruction of the vertices with DA algorithm. The vertices are reconstruced for $\sigma_v^t = 10$ ps and $\sigma_v^z = 10$ μm resolution (see Eq. 4.8). In the reconstruction of the jets, anti-kt algorithm (96) is used to clusterize the hadrons with a parameter of R = 0.4. However, the pile-up subtraction is cruitial in the reconstruction of the jets especially at large pile-up events. Otherwise, jets become fat and large shifts is observed in the reconstructed Higgs mass from the jets (m_H > 124.1 GeV). Since the vertices are already reconstructed by DA algoritm, the charged particles from the pile-up events can be subtracted easily. In reality, there is no chance of knowing which vertex is the hard vertex. Thus, it is necessary to check all reconstructed vertex components for the final state of any physics process. In the study, instead of scanning all the vertices to build jets, the vertex has the closest distance to truth value of the hard vertex is selected among the reconstructed vertices inside DELPHES with a pile-up subtractor module which is written for this study. The closest distance of reconstructed vertex to actual vertex is evaluated with the following formula;

$$distance = \sqrt{\left(\frac{t_{Gen\,V.} - t_{Reco\,V.}}{\sigma^{t}_{Reco\,V.}}\right)^2 + \left(\frac{z_{Gen\,V.} - z_{Reco\,V.}}{\sigma^{z}_{Reco\,V.}}\right)^2} \qquad (4.8)$$

The charged particles inside the closest vertex are used in the jet reconstruction. As discussed in Section 4.2, the DA algorithm only reconstructs vertices in the beam line with prompt tracks. However, some secondary vertices forms within the jets (see Figure 4.3) and charged constituents of these secondary vertices are not attached to the vertices. Reconstruction of jets without them causes a shift in mass but this time towards the low mass region (m_H < 124.1 GeV). Therefore, the tracks of the secondary vertices of the signal jets are attached to the closest vertex if their p_T > 1 GeV. Another pile-up subtraction is performed for neutral particles within the jets. After the jets are reconstructed, the neutral pile-up particles are tried to be subtracted from the jets using the jet areas algorithm (97) already implemented into DELPHES. Jets with p_T > 30 GeV are b-tagged with respect to the efficiency as described in the reference. Similarly, a selection procedure is performed for the photons in DELPHES. In this process, the cone radius (R) between individual photons and charged hadrons is calculated, and if R < 0.3, the sum of the p_T values of the charged hadrons is obtained. The radio between sum p_T value and photon p_T gives the isolation constant ($p_T^{\gamma}/\sum p_T$) and a photon that has an isolation constant below 0.1 is considered as an isolated photon in the study. At the end of the simulation process, the data is saved as a ROOT file for offline analysis.

4.4 Analysis Results and Discussions

First of all, vertex reconstruction performance was obtained by comparing vertex positions and times with true values of vertices for different time resolution options. To make such a comparison, again the closest distance between the reconstructed vertex and the actual vertex was calculated with E.q 4.8. Then, the vertex reconstruction efficiency, merge, fake and duplicate rate of reconstructed vertices are evaluated for the closest distance, d < 2. In the Figure 4.7, all of these performance results are shown as a function of four different tracker time resolutions for different pile-up environments. In the plots, the vertex reconstruction efficiency indicates the ratio between reconstructed and actual vertex size. The merge ratio is the combination rate of two reconstructed vertices as one

vertex against to an actual vertex, while the fake rate stands for the rate of misaligned vertex that is not in $d < 2$ range. Lastly, the duplicate rate measures the reconstruction of any vertex more than once.

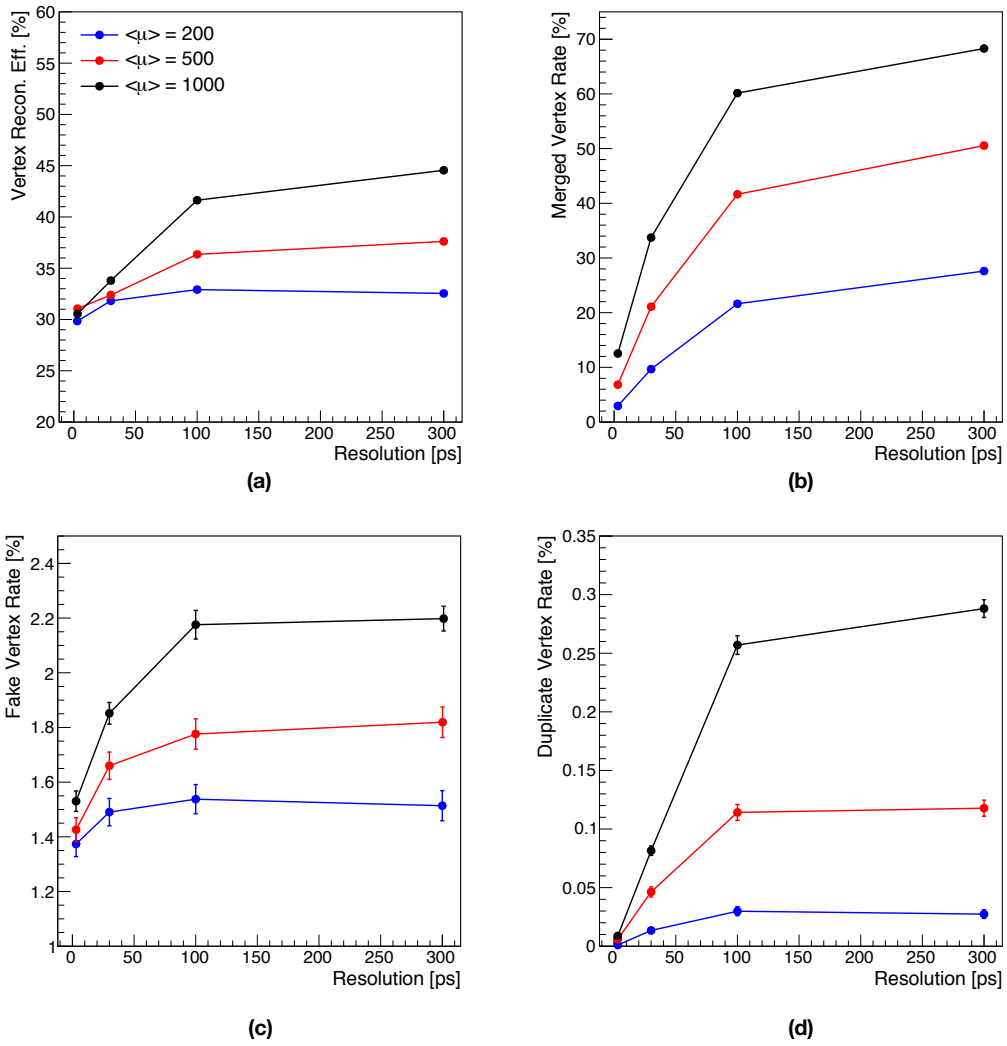

Figure 4.7. (a) Vertex reconstruction efficiency, (b) merged vertex (c) fake and (d) duplicate vertex rate are shown as a function of tracker resolutions for 3, 30, 100 and 300 ps at 200, 500 and 1000 mean pile-up environments.

As seen in Figure 4.7 (a), vertex reconstruction efficiency increases with the pile-up vertex size in the environment. Since vertices are dispersed with Gaussian distribution in the beam spot, the vertex density of the environment affects the reconstructed vertex size and hence efficiency. Moreover, the vertex reconstruction efficiency increases even if tracker has poor time resolution. This situation can be explained by the DA algorithm behaviour. Due to poor timing, the DA algorithm reconstructs a vertex using at least two close vertex tracks, resulting in an increase

as seen at 300 ps for 1000 pile-up vertices. The merge rate graph, Figure 4.7 (b), supports the behaviour mentioned. The ratio of the merged vertices within reconstructed vertices increases for poor time resolution and large the pile-up size. As a result of the merge rate, it is expected to raise the pile-up track contamination in the reconstruction of the primary vertex. Fortunately, the fake and duplicate rates of the reconstructed vertices are very low but similar behaviour is observed in also these plots for poor time resolution and a large pile-up environment parameters.

In addition to vertex reconstruction performance, the primary vertex reconstruction efficiency was determined by applying same the closest distance cut. The closest vertex to the actual primary vertex is considered a reconstructed primary vertex if it is at the closest distance. Then, the pile-up track contamination ratio is obtained for the selected vertex. These two distributions are shown in Figure 4.8 as a function of time resolutions for pile-up environments. The primary vertex reconstruction efficiency decreases dramatically when the tracker time resolution decreases. In addition to the time resolution effects on primary vertex reconstruction efficiency, it depends on the pile-up events and efficiency decreases under a high pile-up environment as seen in Figure 4.8. However, the drop in the primary vertex reconstruction efficiency is around 5% between 200 and 1000 pile-up events for the 30 ps time resolution. This plot is enough to put emphasis on the importance of time resolution because the drop reaches 10% at 300 ps. If the physics process is a very rare process like $HH \rightarrow b\bar{b}\gamma\gamma$, it can result in a poor measurement of the signal. As mentioned, time resolution acts on the vertex reconstruction algorithm in the clustering of tracks because the algorithm recognises some of the pile-up tracks as elements of the primary vertex. When the vertices are produced close enough, tracks can be attached to the wrong vertices at time resolutions larger than 100 ps. As shown in Figure 4.8 (b), the average fake track contamination in the reconstructed primary vertex is around 6% for 30 ps at a 200 pile-up. This simply means that 6% of tracks used in the reconstruction of the primary vertex are pile-up tracks which attached to that vertex in single event. Therefore, the pile-up track contamination increases in the condition of poor time resolution and high pile-up events. It reaches 20% for 300 ps at 1000 pile-up which directly affects the reconstructed mass from the jets and is responsible for a large shift including neutral pile-up particles.

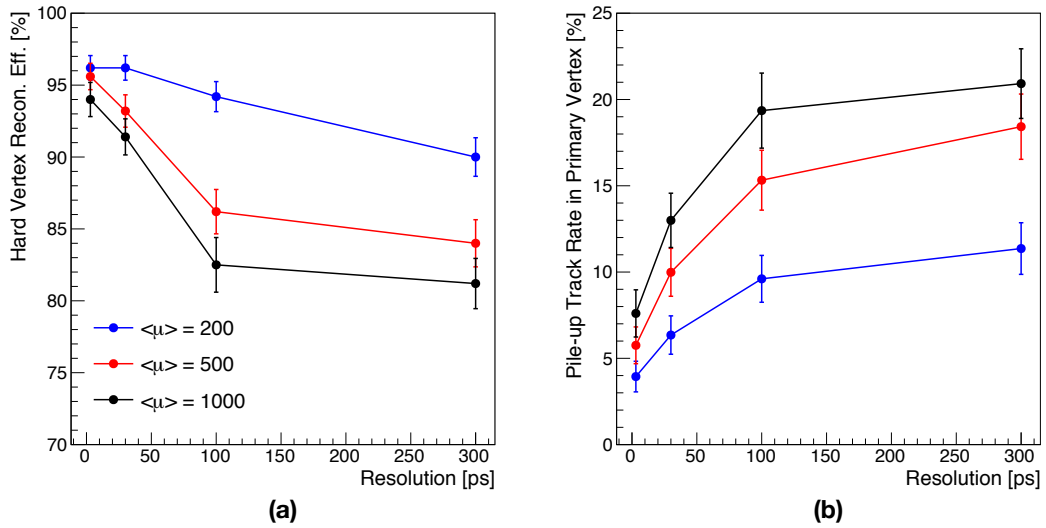

Figure 4.8. (a) The primary vertex reconstruction efficiency, (b) pile-up track contamination in the reconstructed primary vertex are shown for 3, 30, 100 and 300 ps at 200, 500 and 1000 mean pile-up environment.

Analysis of the process was fulfilled in two parts considering jet and photon parts of two Higgs decaying $H \rightarrow b\bar{b}$ and $H \rightarrow \gamma\gamma$, respectively. In the analysis, events are selected with a common preselection cut considering the final state of the process. The events contain at least two separate ($\Delta R > 0.4$) b-tagged jets (b-jets) and at least two isolated photons are selected for the study. Before the reconstruction of the Higgs masses, some kinematical cuts were applied to the b-jets and photons. For the b-jets, kinematical cuts, $p_T > 30$ GeV and $|\eta| < 4.0$, are applied after preselection cut. Then, the invariant mass of Higgs boson is reconstructed with the four-vector of survived ones applying the closest approach which finds the best b-jet pair close to the Higgs mass. In the Figure 4.9, the reconstructed mass plots are shown for 0, 200, 500 and 1000 pile-up scenarios for 30 ps. Without a pile-up environment, the reconstructed mass is around 124.1 GeV, and it meets with the literature. However, the mass of reconstructed Higgs starts to shift towards 200 GeV with the increase of pile-up event size. Even if the fake track contamination rate is below 15% in that 30 ps for all pile-up environments (see Figure 4.8 (b)), the mass shift is very large, and the mass distributions have also large sigma values once the Gaussian fit is applied for the range between 50 GeV and 200 GeV. The mean and sigma value of the applied Gaussian fits to the reconstructed masses for different tracker time resolutions and pile-up events are shown in Figure 4.10. The mass shift with respect to the time resolution of the

tracker cannot be seen clearly except for the 500 and 1000 pile-up environments. Therefore, the tracker time resolution seems less important in the reconstruction of the invariant masses due to the neutral particle contamination. As a result of the large pile-up events, the reconstructed Higgs invariant mass from jets has very broad distribution around m_H = 124.1 GeV. Once the the related backgrounds that has the same final state as the signal ($pp \rightarrow \gamma\gamma$ + jets or $pp \rightarrow j\gamma$ + jets) are included in a study which measures the limits of the signal, the unstisfying results are obtained from the analysis. Therefore, the other decay channels of Higgs self coupling, $HH \rightarrow b\bar{b}b\bar{b}$ and $HH \rightarrow b\bar{b}\tau\tau$, contains more than two jets seems problematic in the reconstruction of events under high pile-up environment.

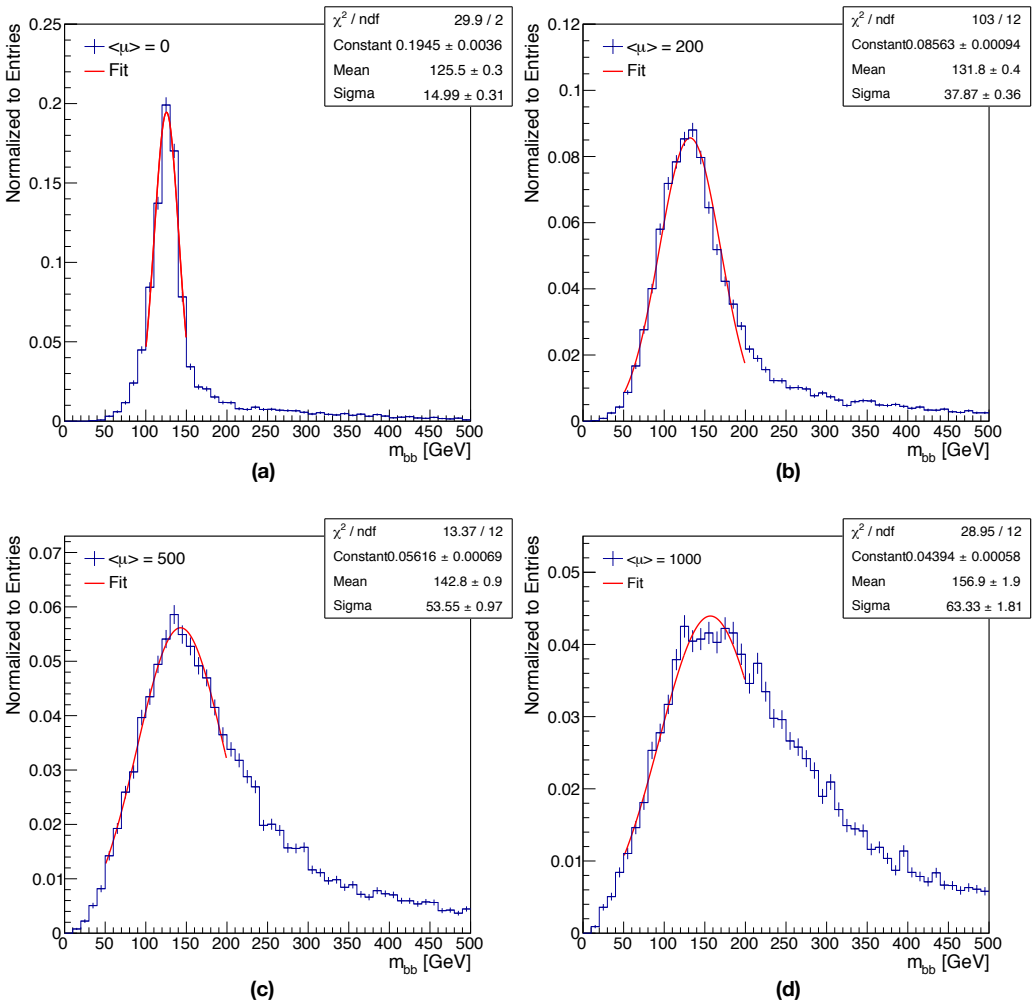

Figure 4.9. The reconstructed Higgs mass from two b-jets for 30 ps inner tracker time resolution at 0 (a), 200 (b), 500 (c) and 1000 (d) pile-up scenarios. The red line respresents the applied Gaussian fit to the obtained mass distributions in the range between 50 GeV and 200 GeV.

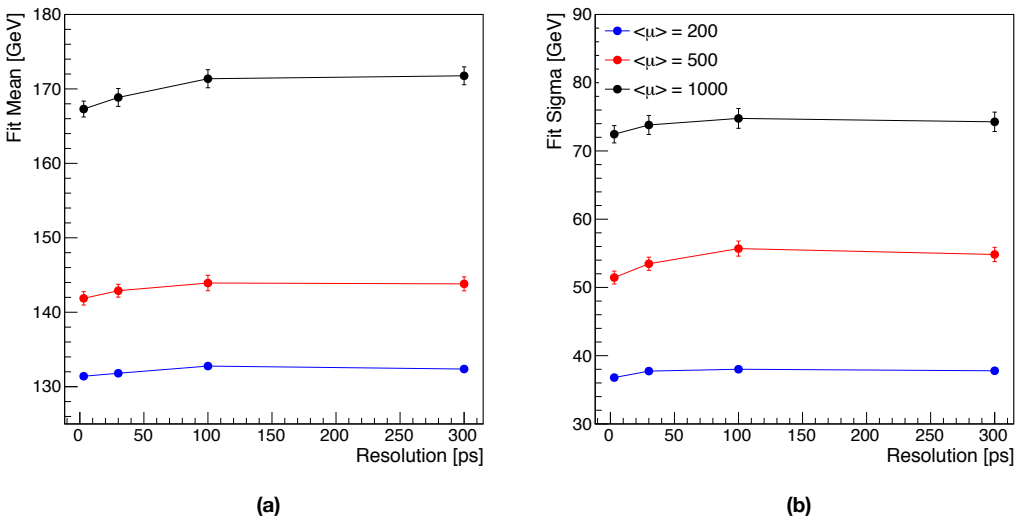

Figure 4.10. (a) Mean and (b)sigma values of Gaussian fit of Higgs mass distributions reconstructed from two b-jets for 3, 30, 100 and 300 ps inner tracker time resolutions at 200, 500 and 1000 pile-up scenarios.

On the other hand, the reconstructed Higgs from two photons is expected to have more sharp distribution than the Higgs mass that reconstructed with jets. Because the pile-up vertices consist of mostly hard QCD events and therefore they does not contain much prompt photons. As a results, more precise Higgs reconstruction can be achievable even in high pile-up environments comparing to the $H \rightarrow b\bar{b}$ part. Therefore, the $H \rightarrow \gamma\gamma$ part makes the signal more distinguishable than $H \rightarrow b\bar{b}$ part. After the reconstruction of H $\rightarrow b\bar{b}$ part, at least two isolated photons have $p_T > 30$ GeV and $|\eta| < 4.0$ are considered in the $H \rightarrow \gamma\gamma$ part of the analysis. Then, the ΔR between b-jets that are used in the reconstruction of Higgs and the selected photons are evaluated and the photons has $\Delta R > 0.4$ are taken into account to reconstruct invariant mass of Higgs boson with four-vector of photons. Due to the any increase pile-up events in the environment, the probability of isolated fake photons able to pass through the kinematic cuts increases in the reconstruction of the Higgs boson. Similar to the first part, Higgs invariant mass is obtained with the photons that give the closest mass result to $m_H = 124.1$ GeV after mentioned kinematic cuts. In Figure 4.11, the reconstructed Higgs boson from two photons is shown for 0, 200, 500, 1000 pile-up events. As seen in Figure 4.11, the reconstructed Higss peak around the 124.1 GeV regardless of the pile-up environment. To compare consistency in the mass region, a Gaussian fit are applied to the reconstructed Higgs considering to range between 110 GeV and 140 GeV. Mean and sigma results of the applied fits are represented in Figure 4.12. Since the

photons are not detectable by the tracker system of the detector, the time resolution of the tracker has no effect on the Higgs bosons reconstructed from the photons, and so the results in Figure 4.12 are shown for data generated with 30 ps time tracker time resolution. The mean and sigma results of the fits are very low comparing to the first part of analysis (see Figure 4.10) but the slight shift is related to the pile-up environment still can be seen in the fit plots.

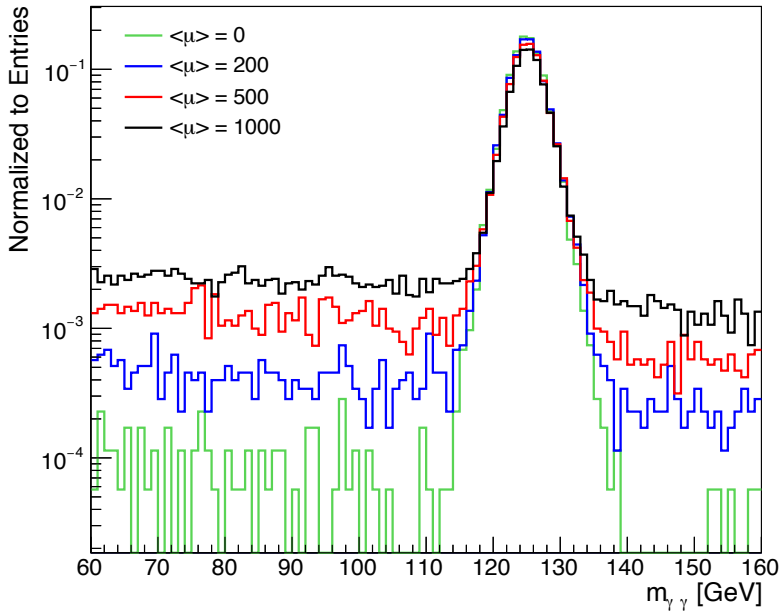

Figure 4.11. The reconstructed Higgs boson from isolated two photons that have p_T > 30 GeV and $|\eta|$ < 4.0 distribution for 0, 200, 500, 1000 pile-up events.

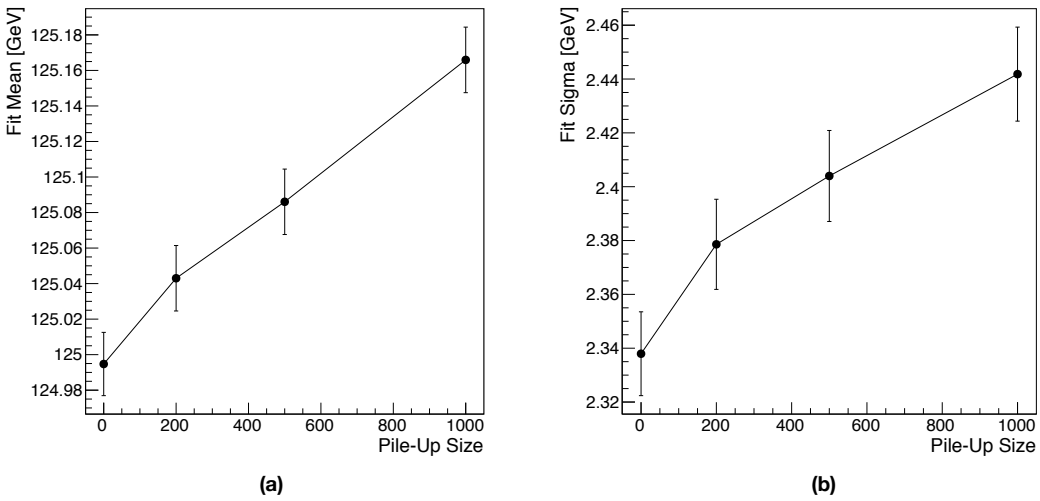

Figure 4.12. (a) The mean and (b) sigma results of the applied Gaussian fits on reconstructed Higgs invariant mass in the range between 110 GeV and 140 GeV.

Even though the reconstructed Higgs from photons has better distribution than the b-jets, it does not mean that there is no pile-up photon contamination in the reconstruction of the Higgs boson. This can be seen clearly in the reconstructed Higgs distribution except for the mass peaks. The reconstructed Higgs bosons outside the mass region increase with the pile-up event increase in the environment. While a few reconstructed Higgs outside of the mass region can be seen at zero pile-up environment, the size of reconstructed Higgs outside of the mass region increases with the pile-up event size as seen in Figure 4.11. This means that one of the photons used in the calculation of the mass are not come from Higgs and it comes from secondary elements, such as decay of π^0, within the QCD jets of pile-up vertex. Thanks to the Monte Carlo method, the mother of particles is known and average pile-up photon contamination ratio in the reconstructed masses can be obtained at different pile-up scenarios for given event size. In Figure 4.13, the average pile-up photon contamination rate in reconstructed mass is shown as a function of the pile-up environment for each tracker time resolution option. As expected, no significant effect of tracker time resolution is seen the pile-up photon contamination in the reconstructed Higgs except the pile-up size of environment. However, it is observed that the number of pile-up events in the detector directly increases the pile-up photon rate contamination in the reconstruction of the Higgs bosons up to 20%.

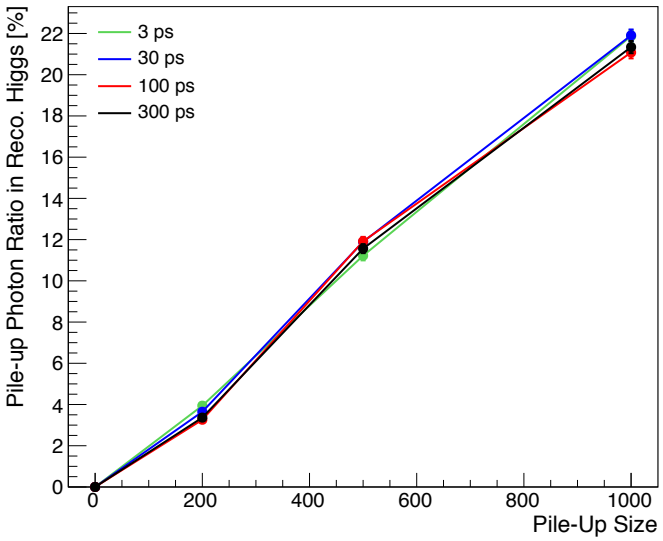

Figure 4.13. The average pile-up photon contamination ratio in the reconstructed Higgs bosons from two photons for different inner tracker time resolutions.

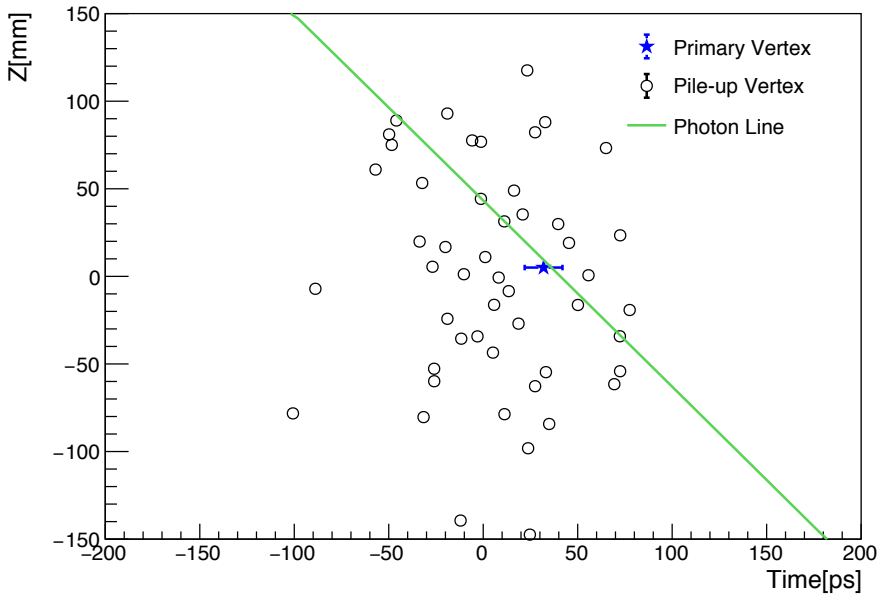

Figure 4.14. The obtained photon line, green line, with Eq. 4.10. and the reconstructed vertices at the 2D vertex perspective. The primary vertex, illustrated with blue star, is the vertex of the $HH \rightarrow b\bar{b}\gamma\gamma$ and pile-up vertices are represented with black circles.

The pile-up photon contamination problem can be solved using the primary vertex position and time values. Since the initial time and position of a photon cannot be determined by the inner tracker, there is no chance to find initial position and time of photon. However, the final position and time are measured in the electromagnetic calorimeter. Using the time-of-flight method, the initial position and time can be determined with respect to the vertex position and time values. The time-of-flight equation of the photon can be written as;

$$(t_c - t_i)\mathrm{c} = \sqrt{(X_c - X_i)^2 + (Y_c - Y_i)^2 + (Z_c - Z_i)^2} \qquad (4.9)$$

where t_c and t_i are measured time photon at calorimeter and initial time of photon respectively, c is speed of light, X_c, Y_c and Z_c are position components of the photon at calorimeter, X_i, Y_i and Z_i are initial position components of the photon. In reality, the beam profile is obtained to evaluate X and Y components of the vertices for precise measurement. In this study, the vertices are considered perfectly distributed and therefore the X_i and Y_i positions of the vertices are taken zero. Then, the initial position (Z_i) of photon can be re-written as a function of time with the Eq. 4.9;

$$Z_i = Z_c \pm \sqrt{(t_c - t_i)^2 c^2 \; - \; (X_c^2 + Y_c^2)} \tag{4.10}$$

where all parameters in the equation are known except t_i. The Eq. 4.10 is actually a linear function for a given photon hit at calorimeter (X_c, Y_c, Z_c and t_c). The representation of this function (Eq. 4.10) at the 2D vertex perspective (position vs time plane) is shown in Figure 4.14. The distance between photon line and primary vertex can be used as a new selection parameter to get rid of fake photons. The distance can be evaluated as follows;

$$\mathrm{d} = \sqrt{(t_v - t_i)^2 \; - \; (Z_v - Z_i)^2} \tag{4.11}$$

where $Z_v$and t_v are position and time of primary vertex, respectively. The Eq. 4.10 can be written instead of Z_i in the equation. If the derivative of the Eq. 4.11 is taken and equals to zero ($d' = 0$), the closest distance is obtained for primary vertex. As seen in Eq. 4.11, the calculated photon distance depends on photon hit position resolution at calorimeter, the time resolution of electromagnetic calorimeter and tracker. The position resolution of the photon hit on the calorimeter bases on the η–φ granularity of the calorimeter which is detailed in the first chapter. In this study, the time resolution of the electromagnetic calorimeter is set to 30 ps, although the time resolution of the electromagnetic calorimeter actually depends on the energy of the photon. The latest paramater, time value of vertex, is directly depends on the tracker time resolution. As discussed, if the time resolution of the inner tracker system is good enough, the time and position of the vertex can be reconstructed perfectly. This leads to obtain small distance results for the photons that come from primary vertex. In Figure 4.15, the logarithm of distance ($log_{10}(d)$) of the prompt, which comes from Higgs, and pile-up photon lines with respect to the primary vertex are shown for 1000 pile-up environment for 4 different inner tracker time resolutions. As seen in the Figure 4.15, the inner tracker resolution affects the $log_{10}(d)$ values due to the relation in Eq. 4.11. While the distribution of prompt and pile-up photons can be distinguishable at the 3 and 30 ps tracker time resolution, the distributions are nearly overlapped for the 3 and 30 ps tracker time resolution. However, it still can be used as a pile-up subtractor parameter to exclude pile-up photons. Firstly, it is needed to plot pile-up photon rejection efficiency versus prompt photon efficiency. Then, the $log_{10}(d)$ value can be obtained easily for the

given prompt photon efficiency. In Figure 4.16 (a), the pile-up photon rejection efficiency versus prompt photon efficiency is reprensented for 4 different innter tracker time resolutions at 1000 pile-up. Also, the prompt photon efficiencies are shown as a function $log_{10}(d)$ value in Figure 4.16 (b).

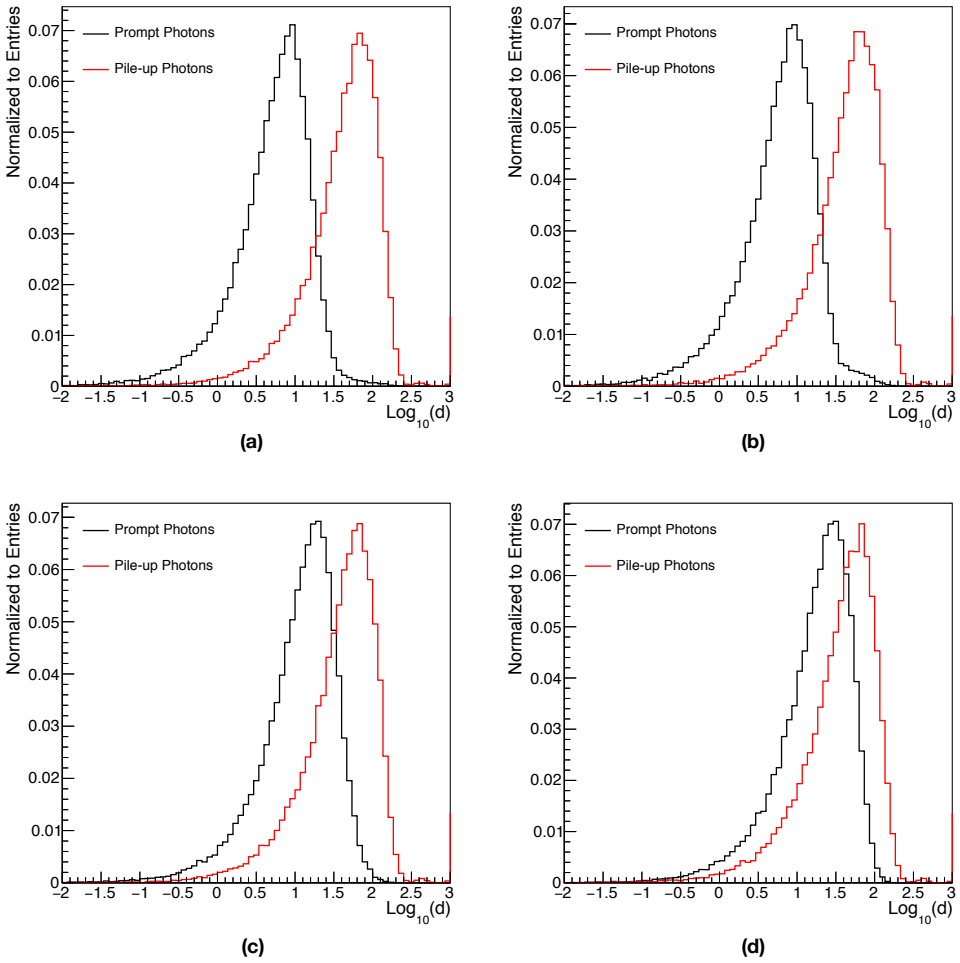

Figure 4.15. The logarithm of distances ($log_{10}(d)$) of the promptand pile-up photon lines with respect to the primary vertex for (a) 3, (b) 30, (c) 100 and (d) 300 ps inner tracker time resolutions at 1000 pile-up environment.

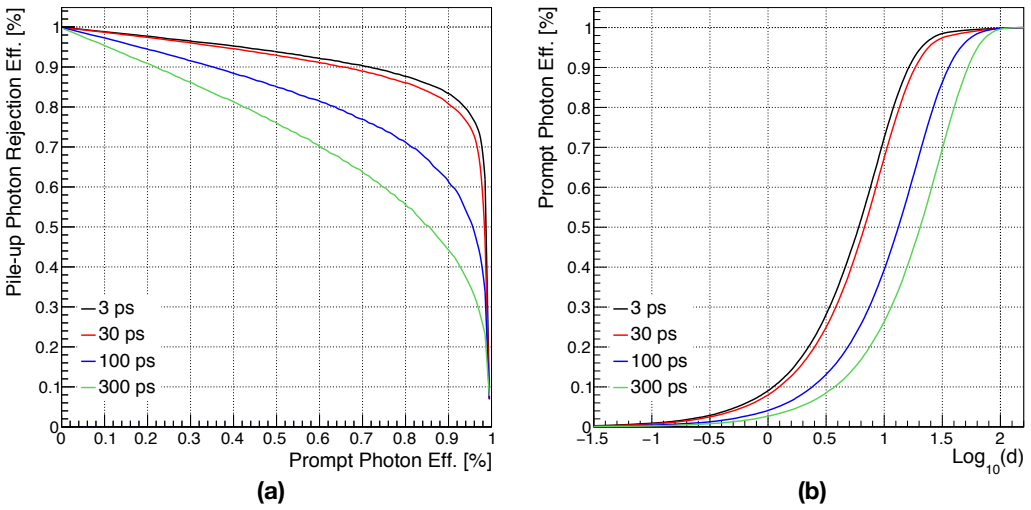

Figure 4.16. (a) The pile-up photon rejection efficiency versus prompt photon efficiency (b) The prompt photon efficiency as a $log_{10}(d)$ are reprensented for 4 different inner tracker time resolutions at 1000 pile-up.

In Figure 4.16, it can be clearly seen that more than 80% of the pile-up photons in the environment can be excluded for 90% prompt photon efficiency at 3 and 30 ps tracker time resolutions. On the other hand, only 45% and 60% of pile-up photons are excluded at 90% prompt photon efficiency at 100 and 300 ps tracker time resolutions, respectively. The $log_{10}\, d$ cut values are determined from the Figure considering the 90% prompt photon efficiency. Therefore, in the reconstruction of the Higgs boson, the $log_{10}(d) < 1.25$ is the selection criteria for photons in the data produced with 3 and 30 ps tracker time resolutions. For the data produced with 100 and 300 ps tracker time resolutions, $log_{10}(d) < 1.6$ is applied (see Figure 4.16(b)) as cut for the photons after the cuts mentioned in the analysis procedure. In this way, it is aimed to reconstruct the Higgs boson from the photons coming from the primary vertex, not the pile-up vertices. The obtained pile-up contamination in the Higgs mass after $log_{10}(d)$ cut is shown as a function of pile-up size in the environement for each inner tracker time resolution. As a result of the $log_{10}(d)$ cut in anaysis, the pile-up contamination for the 3 ps and 30 ps time resolution are decreased from 22% to 7% and 8% at 1000 pile-up event, respectively. In fact, 100 ps and 300 ps time resolution around drops from 22% to 9% and 7% are observed after applying $log_{10}(d)$ cut to analysis. Once again, the importance of the inner tracker time resolution is observed even for the photons

which the tracker does not detect. However, significant results can only be achievable at high time resolutions as seen in Figure 4.17.

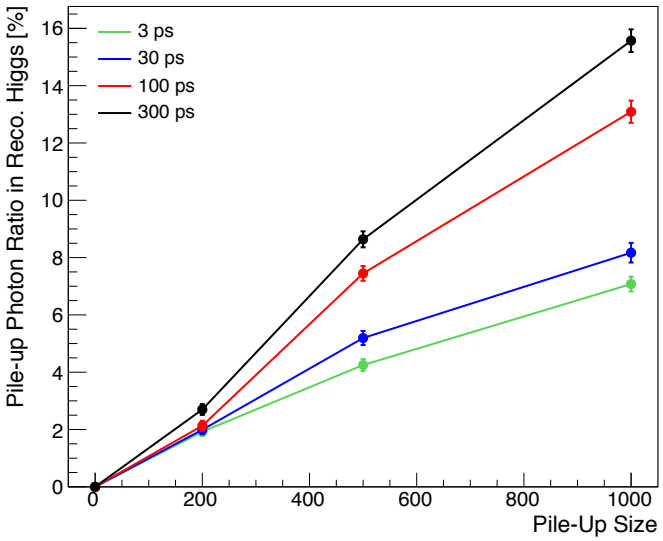

Figure 4.17. The average pile-up photon contamination ratio in the reconstructed Higgs mass after applying $log_{10}(d)$ cut to photons for different inner tracker time resolutions and pile-up events.

In short, the time resolution effects of the inner tracker on the vertex reconstruction and pile-up contamination on mass distributions are obtained for different pile-up scenarios of FCC-hh using $gg \rightarrow HH$ physics process with its $HH \rightarrow b\bar{b}\gamma\gamma$ decay channel. In the benchmark tests of the pile-up environment versus the time resolution of the tracker system, it is found that a time resolution below 30 ps is needed for proper measurements so that proper physics studies can be done with low pile-up contamination. The study also demonstrated the importance of the inner tracker time resolution for removing pile-up photons from the mass reconstruction process using the time-of-flight method.

5. CONCLUSIONS AND RECOMMENDATIONS

Undoubtedly, the FCC-hh will be one of the most interesting and great man-made instruments of our time in the years to come. Such a large instrument will allow observations that contain answers to questions humanity has been asking. Considering the collision energy it has, it is predicted that the SM, which is one of the leading theories that try to explain why matter exists and particles have mass, will be tested more precisely ever than before. In addition, it is obvious that it will be a discovery machine not only for the BSM theories but also dark matter and dark energy, which are important questions for modern physics today. However, some difficulties arise in terms of technology and observation when such large energies are reached. Among them, the radiation levels in the environment, especially around the beam line, is a challenge for today's technologies. The second problem is pile-up events in the environment. This creates the high-resolution requirement for the FCC-hh detector, which is intended to be a discovery machine. Otherwise, it is estimated that the mentioned discoveries will become impossible to observe due to the pile-up vertices in the environment. In the study, the development process of radiation hard MALTA sensors, which are seen as the precursors of pixel sensors to be used in future experiments, was explained in detail. Moreover, using the time resolution of MALTA and ultimate time resolutions, an example physics simulation has been done including realistic detector effects under the pile-up environment of the FCC-hh.

In the first part of the thesis, the development process of MALTA sensor, a monolithic silicon pixel sensor with small collection electrode produced by Tower Semiconductor in 180 nm CMOS imaging technology, has been demonstrated in detail. Thanks to its 36.4 um pitch size, 100 um thin structure and radiation resistance, it is the one of the candidate sensors among the pixel sensors that can be planned to use in future experiments such as FCC-hh. The development process of MALTA sensor still continues with the results obtained from laboratory and test beam measurements. As a result of these measurements, the in-pixel hit efficiency losses caused by the high radiation at the edges of pixels are eliminated successfully with the improvements made in both the pixel structure and the front-end circuit. In addition, the radiation dispersion and RTS noise caused by high radiation has been eliminated with the improvements made in the analog front-end. Also, it is aimed

to increase radiation resistance by preferring Czochralski silicon growth method instead of common Epitaxial methods. After all these modifications, it has been observed by test beam studies that the most recent version, MALTA2, performs 97% in-pixel hit efficiency at 3×10^{15} 1 MeV n_{eq}/cm^2 NIEL dose. The in-time efficiency of the sensor within 25 ns time window is around 92% and the time resolution of the sensor, is 350 ps, were also determined with the combination laboratory and test beam measurements. Since it is developed for the HL-LHC inner tracker upgrade of ATLAS experiment, the obtained results of MALTA sensor show that it is far below the FCC-hh radiation requirements. The in-time efficiency of more than 90% at 25 ns meets with FCC-hh bunch crossing requirements but time resolution of the sensor still large for FCC-hh requirements.

With the TCAD simulations to be made on the pixel structure and the Cz silicon growth method to be used, the radiation resistance of the sensor can be increased to be limits of FCC-hh. This also must be supported by improvements in the front-end circuit. However, 180 nm CMOS imaging technology may be insufficient considering the pitch size of the sensor. In order to reduce the effects of radiation, enlarged transistors is needed to be added to the front-end circuit may create congestion in the design, which increases the need for a smaller CMOS imaging technology such as 65 nm in the digital front-end of the sensor. Another improvement should be done in the time resolution of the sensor. With the high lateral electric field created inside the sensor, the electrons that are collected quickly and the fast-response front-end circuit causes an improvement in the time resolution of the sensor. Thanks to its the improvable structure, just like the MALTA sensor developed with the experience gained from the ALPIDE sensor, the sensor to be developed for the FCC-hh inner tracker will undoubtedly include the experience gained from the MALTA sensor.

In the second part of the thesis, a simulation study was carried out under the FCC-hh's possible pile-up environments for different inner tracker time resolutions including the time resolution of MALTA sensor. In this study, assuming that the MALTA sensor is used in the inner tracker of the FCC-hh detector, the effect of the time resolution of the sensor on the physics process is examined simulating realistic detector effect within DELPHES framework. In the study, the Higgs self-coupling, $gg \rightarrow HH$, for $HH \rightarrow b\bar{b}\gamma\gamma$ decay channel, which is a rare physics process, was chosen to be tested in the FCC-hh detector. By using the time and position

information of the charged particles in the b-jets, vertices were reconstructed for different inner tracker time resolutions under different pile-up scenarios with the Deterministic Annealing method. It has been observed that the time resolution of the MALTA sensor can detect the vertex containing the real physics process with a performance over 80% with 20% pile-up track contamination in the reconstructed vertex under 1000 pile-up events. For the aimed time resolution of FCC-hh which is 30 ps, primary vertex reconstruction efficiency found that more than 92% and pile-up track contamination at the same pile-up environment is around 10%. This shows the importance of the inner tracker time resolution performance. However, the time resolution dependence on the reconstructed mass can be seen slightly in the reconstructed Higgs invariant masses from two b-jets due to the abundance of neutral particles come from pile-up vertices. These results showed that the problem of excess neutral particles in the environment is important enough to affect the physics studies. For this physics process, this increases importance of Higgs reconstructed from photons. Looking at the other Higgs reconstructed from photons, a rather sharp mass distribution is obtained comparing to b-jet part. However, the probability that one of the photons selected to reconstruct the invariant mass in 1000 pile-up is a pile-up photon is around 20% for the given cuts in the analysis. It is demonstrated that the pile-up photon is subtracted from mass reconstruction with the time-of-flight approach using obtained vertex time and positions from DA algorithm. Applying this approach in the analysis, a pile-up photon contamination rate on the reconstructed Higgs decreases from 22% to 8% at 30 ps time resolution under 1000 pile-up environment. On the other hand, compared to the pile-up photon ratio at the 300 ps which decreases from 22% to 15%, it is found that the time resolution of the MALTA sensor may not be enough to obtain precise physics measurements.

In this study, only time resolution importance of the sensor and its effect on vertex reconstruction and mass reconstruction are obtained with an example physics process in the DELPHES simulation for FCC-hh. Therefore, this is a demonstrator benchmark study for the tracker's pile-up environment and time resolutions of the FCC-hh inner tracker system. Since it is done with some assumptions in the study, it still requires full simulation with GEANT4 simulation to see effects on the physics process for a detailed analysis. Also, the inner tracker system of FCC-hh can be tested with recently developed tracker simulation program, ACTS (98), including

material environment of tracker system and track reconstruction algorithms like Kalman Filter. As a result, more accurate results can be found for MALTA sensor and the physics study including realistic detector effects.

6. REFERENCES

In this thesis, Vancouver citation style is used.

1. File:Standard Model of Elementary Particles Anti.svg - Wikimedia Commons [Internet]. [cited 2022 Jun 7]. Available from: https://commons.wikimedia.org/wiki/File:Standard_Model_of_Elementary_Particles_Anti.svg

2. Englert F, Brout R. Broken symmetry and the mass of gauge vector mesons. Physical Review Letters [Internet]. 1964 Aug 31 [cited 2022 May 1];13(9):321–3. Available from: https://journals.aps.org/prl/abstract/10.1103/PhysRevLett.13.321

3. Higgs PW. Broken symmetries and the masses of gauge bosons. Physical Review Letters [Internet]. 1964 Oct 19 [cited 2022 May 1];13(16):508–9. Available from: https://journals.aps.org/prl/abstract/10.1103/PhysRevLett.13.508

4. Mitsou VA. Dark matter searches at LHC. Journal of Physics: Conference Series [Internet]. 2011 Apr 6 [cited 2022 May 1];335(1). Available from: http://arxiv.org/abs/1104.1149

5. Evans L, Bryant P. LHC Machine. Journal of Instrumentation [Internet]. 2008 Aug 14 [cited 2022 May 1];3(08):S08001. Available from: https://iopscience.iop.org/article/10.1088/1748-0221/3/08/S08001

6. Aad G, Abat E, Abdallah J, Abdelalim AA, Abdesselam A, Abdinov O, et al. The ATLAS Experiment at the CERN Large Hadron Collider. Journal of Instrumentation [Internet]. 2008 Aug 14 [cited 2022 May 1];3(08):S08003. Available from: https://iopscience.iop.org/article/10.1088/1748-0221/3/08/S08003

7. Chatrchyan S, Hmayakyan G, Khachatryan V, Sirunyan AM, Adam W, Bauer T, et al. The CMS experiment at the CERN LHC. Journal of Instrumentation [Internet]. 2008 Aug 14 [cited 2022 May 1];3(08):S08004. Available from: https://iopscience.iop.org/article/10.1088/1748-0221/3/08/S08004

8. Aamodt K, Quintana AA, Achenbach R, Acounis S, Adamová D, Adler C, et al. The ALICE experiment at the CERN LHC. Journal of Instrumentation [Internet]. 2008 Aug 14 [cited 2022 May 1];3(08):S08002. Available from: https://iopscience.iop.org/article/10.1088/1748-0221/3/08/S08002

9. Augusto Alves A, Andrade Filho LM, Barbosa AF, Bediaga I, Cernicchiaro G, Guerrer G, et al. The LHCb Detector at the LHC. Journal of Instrumentation [Internet]. 2008 Aug 14 [cited 2022 May 1];3(08):S08005. Available from: https://iopscience.iop.org/article/10.1088/1748-0221/3/08/S08005

10. Chatrchyan S, Khachatryan V, Sirunyan AM, Tumasyan A, Adam W, Aguilo E, et al. Observation of a new boson at a mass of 125 GeV with the CMS experiment at the LHC. Physics Letters B. 2012 Sep 17;716(1):30–61.

11. Aad G, Abajyan T, Abbott B, Abdallah J, Abdel Khalek S, Abdelalim AA, et al. Observation of a new particle in the search for the Standard Model Higgs boson with the ATLAS detector at the LHC. Physics Letters B. 2012 Sep 17;716(1):1–29.

12. Vol. 10 (2020): High-Luminosity Large Hadron Collider (HL-LHC): Technical design report | CERN Yellow Reports: Monographs [Internet]. [cited 2022 May 1]. Available from: https://e-publishing.cern.ch/index.php/CYRM/issue/view/127

13. Schmidt B. The High-Luminosity upgrade of the LHC: Physics and Technology Challenges for the Accelerator and the Experiments. Journal of Physics: Conference Series [Internet]. 2016 Apr 1 [cited 2022 May 1];706(2):022002. Available from: https://iopscience.iop.org/article/10.1088/1742-6596/706/2/022002

14. The European Strategy for Particle Physics Update 2013 - CERN Document Server [Internet]. [cited 2022 May 1]. Available from: https://cds.cern.ch/record/1567258

15. Abada A, Abbrescia M, AbdusSalam SS, Abdyukhanov I, Fernandez JA, Abramov A, et al. FCC Physics Opportunities. The European Physical Journal C 2019 79:6 [Internet]. 2019 Jun 5 [cited 2022 May 1];79(6):1–161. Available from: https://link.springer.com/article/10.1140/epjc/s10052-019-6904-3

16. Abada A, Abbrescia M, AbdusSalam SS, Abdyukhanov I, Abelleira Fernandez J, Abramov A, et al. FCC-ee: The Lepton Collider. The European Physical Journal Special Topics 2019 228:2 [Internet]. 2019 Jun 4 [cited 2022 May 1];228(2):261–623. Available from: https://link.springer.com/article/10.1140/epjst/e2019-900045-4

17. Abada A, Abbrescia M, AbdusSalam SS, Abdyukhanov I, Abelleira Fernandez J, Abramov A, et al. FCC-hh: The Hadron Collider. The European Physical Journal Special Topics 2019 228:4 [Internet]. 2019 Jul 5 [cited 2022 May 1];228(4):755–1107. Available from: https://link.springer.com/article/10.1140/epjst/e2019-900087-0

18. Chancé A, Boutin D, Dalena B, Holzer B, Schulte D. Overview of Arc Optics of FCC-hh. Proc 9th International Particle Accelerator Conference (IPAC'18) [Internet]. 2018 Jun 1 [cited 2022 May 1];141–4. Available from: http://jacow.org/ipac2018/papers/thpmf011.pdf

19. First results for a FCC-hh ring optics design - CERN Document Server [Internet]. [cited 2022 May 1]. Available from: https://cds.cern.ch/record/2009373

20. Sheehy S, Budzik K, Carr E, Kelliher D, Machida S, Martin L, et al. Updates on the Optics of the Future Hadron-Hadron Collider FCC-hh. IPAC 2017: The eighth International Particle Accelerator Conference [Internet]. 2017 May 1 [cited 2022 May 1];(THPVA027):2023–6. Available from: http://accelconf.web.cern.ch/AccelConf/ipac2017/doi/JACoW-IPAC2017-THPVA027.html

21. Lorin C, Segreti M, Durante M. Design of a Nb3Sn 16 T Block Dipole for the Future Circular Collider. IEEE Transactions on Applied Superconductivity. 2018 Apr 1;28(3).

22. Marinozzi V, Bellomo G, Caiffi B, Fabbricatore P, Farinon S, Ricci AM, et al. Conceptual Design of a 16 T cos θ Bending Dipole for the Future Circular Collider. IEEE Transactions on Applied Superconductivity. 2018 Apr 1;28(3).

23. Glover EWN, van der Bij JJ. Higgs boson pair production via gluon fusion. Nuclear Physics B. 1988 Nov 7;309(2):282–94.

24. Barger V, Han T, Phillips RJN. Double Higgs-boson bremsstrahlung from *W* and *Z* bosons at supercolliders. Physical Review D [Internet]. 1988 Nov 1 [cited 2022 May 1];38(9):2766. Available from: https://journals.aps.org/prd/abstract/10.1103/PhysRevD.38.2766

25. Drasal Z, Riegler W. An extension of the Gluckstern formulas for multiple scattering: analytic expressions for track parameter resolution using optimum weights. Nuclear Instruments and Methods in Physics Research, Section A: Accelerators, Spectrometers, Detectors and Associated Equipment [Internet]. 2018 May 30 [cited 2022 May 14];910:127–32. Available from: http://arxiv.org/abs/1805.12014

26. Drasal Z, on behalf of the FCC-hh Detector Working Group. Status & Challenges of Tracker Design for FCC-hh. Proceedings of Science [Internet]. 2018 Dec 5 [cited 2022 May 14];309:030. Available from: https://pos.sissa.it/

27. Aleksa M, Allport P, Bosley R, Faltova J, Gentil J, Goncalo R, et al. Calorimeters for the FCC-hh. 2019 Dec 20 [cited 2022 May 1]; Available from: https://arxiv.org/abs/1912.09962v1

28. Agostinelli S, Allison J, Amako K, Apostolakis J, Araujo H, Arce P, et al. Geant4—a simulation toolkit. Nuclear Instruments and Methods in Physics Research Section A:

Accelerators, Spectrometers, Detectors and Associated Equipment. 2003 Jul 1;506(3):250–303.

29. Bierlich C, Chakraborty S, Desai N, Gellersen L, Helenius I, Ilten P, et al. A comprehensive guide to the physics and usage of PYTHIA 8.3. 2022 Mar 22 [cited 2022 May 1]; Available from: https://arxiv.org/abs/2203.11601v1

30. Technical Design Report for the Phase-II Upgrade of the ATLAS Tile Calorimeter - CERN Document Server [Internet]. 2017 [cited 2022 May 14]. Available from: https://cds.cern.ch/record/2285583

31. Aad G, Abbott B, Abdallah J, Abdinov O, Aben R, Abolins M, et al. Topological cell clustering in the ATLAS calorimeters and its performance in LHC Run 1. European Physical Journal C [Internet]. 2016 Mar 9 [cited 2022 May 14];77(7). Available from: https://arxiv.org/abs/1603.02934v3

32. Cacciari M, Salam GP, Soyez G. The anti-kt jet clustering algorithm. Journal of High Energy Physics [Internet]. 2008 Apr 16 [cited 2022 May 1];2008(04):063. Available from: https://iopscience.iop.org/article/10.1088/1126-6708/2008/04/063

33. Kroha H. Design and construction of integrated small-diameter drift tube and thin-gap resistive plate chambers for the phase-1 upgrade of the ATLAS muon spectrometer. Nuclear Instruments and Methods in Physics Research Section A: Accelerators, Spectrometers, Detectors and Associated Equipment. 2019 Aug 21;936:445–6.

34. Eberwein GH, Kortner O, Kroha H, Rendel M, Rieck P, Soyk D, et al. Commissioning and installation of the new small-Diameter Muon Drift Tube (sMDT) detectors for the Phase-I upgrade of the ATLAS Muon Spectrometer. 2021 Dec 13 [cited 2022 May 1]; Available from: https://arxiv.org/abs/2112.07026v1

35. Voevodina E. Commissioning of the New sMDT Monitored Drift Tube Detectors for the Phase-1 Upgrade of the ATLAS Muon Spectrometer. Physics of Atomic Nuclei. 2021 Jul 1;84(4):562–70.

36. Aad G, Abbott B, Abbott DC, Abud AA, Abeling K, Abhayasinghe DK, et al. Performance of the ATLAS RPC detector and Level-1 muon barrel trigger at √(s)=13 TeV. Journal of Instrumentation [Internet]. 2021 Jul 19 [cited 2022 May 1];16(07):P07029. Available from: https://iopscience.iop.org/article/10.1088/1748-0221/16/07/P07029

37. Kortner O, Kortner S, Kroha H, Podkladkin S, Richter R. Design of the FCC-hh muon detector and trigger system. Nuclear Instruments and Methods in Physics Research Section A: Accelerators, Spectrometers, Detectors and Associated Equipment. 2019 Aug 21;936:447–8.

38. Battistoni G, Boehlen T, Cerutti F, Chin PW, Esposito LS, Fassò A, et al. Overview of the FLUKA code. Annals of Nuclear Energy. 2015 Aug 1;82:10–8.

39. Meroli S, Passeri D, Servoli L. Energy loss measurement for charged particles in very thin silicon layers. Journal of Instrumentation. 2011 Jun;6(6).

40. Sharma A, Allport P, Asensi I, Berdalović I, Bortoletto D, Buttar C, et al. Latest developments and characterisation results of the MALTA sensors in TowerJazz 180nm for High Luminosity LHC. 2022 May 12;398:818.

41. p–n junction - Wikipedia [Internet]. [cited 2022 May 14]. Available from: https://en.wikipedia.org/wiki/P%E2%80%93n_junction

42. Nishizawa JI. Junction Field-Effect Devices. 1982 [cited 2022 May 13];241–72. Available from: https://link.springer.com/chapter/10.1007/978-1-4684-7263-9_11

43. MOSFET Physics [Internet]. [cited 2022 May 14]. Available from: https://www.mksinst.com/n/mosfet-physics

44. MOSFETs [Internet]. [cited 2022 May 14]. Available from: https://courses.engr.illinois.edu/ece110/sp2021/content/courseNotes/files/?MOSFETs

45. Kolanoski H, Wermes N. Particle detectors: Fundamentals and applications. Particle Detectors: Fundamentals and Applications. 2020 Sep 17;1–910.

46. Snoeys W. Monolithic pixel detectors for high energy physics. Nuclear Instruments and Methods in Physics Research Section A: Accelerators, Spectrometers, Detectors and Associated Equipment. 2013 Dec 11;731:125–30.

47. Pater J, on behalf of the ATLAS Collaboration. ATLAS Pixel Detector upgrade at High Luminosity LHC. 2020 Sep 14;373:011.

48. Kim D, Aglieri Rinella G, Cavicchioli C, Chanlek N, Collu A, Degerli Y, et al. Front end optimization for the monolithic active pixel sensor of the ALICE Inner Tracking System upgrade. Journal of Instrumentation [Internet]. 2016 Feb 15 [cited 2022 May 13];11(02):C02042. Available from: https://iopscience.iop.org/article/10.1088/1748-0221/11/02/C02042

49. Aglieri Rinella G. The ALPIDE pixel sensor chip for the upgrade of the ALICE Inner Tracking System,. Nucl Instrum Meth. 2017 Feb 11;845:583.

50. Tower Semiconductor. Tower Semiconductor [Internet]. [cited 2022 May 13]. Available from: https://towersemi.com/

51. Cardella R. CMOS detector and system developments for LHC detector upgrades [Internet] [PhD]. [Oslo]: Oslo U.; 2019 [cited 2022 May 13]. Available from: https://cds.cern.ch/record/2702969

52. van Hoorn JW. Study and Development of a novel Silicon Pixel Detector for the Upgrade of the ALICE Inner Tracking System [Internet] [PhD]. [Vienna]: TU Vienna; 2015 [cited 2022 May 13]. Available from: https://cds.cern.ch/record/2119197

53. Berdalovic I, Argemi LS, Cardella R, Dachs F, Dao V, de Acedo LFS, et al. MALTA: A CMOS pixel sensor with asynchronous readout for the ATLAS High-Luminosity upgrade. 2018 IEEE Nuclear Science Symposium and Medical Imaging Conference, NSS/MIC 2018 - Proceedings. 2018 Nov 1

54. Cardella R, Tortajada IA, Berdalovic I, Bespin C, Dachs F, Dao V, et al. MALTA: an asynchronous readout CMOS monolithic pixel detector for the ATLAS High-Luminosity upgrade. Journal of Instrumentation [Internet]. 2019 Jun 18 [cited 2022 May 13];14(06):C06019. Available from: https://iopscience.iop.org/article/10.1088/1748-0221/14/06/C06019

55. Cardella R, Berdalovic I, Plaja NE, Kugathasan T, Tobon CAM, Pernegger H, et al. LAPA, a 5 Gb/s modular pseudo-LVDS driver in 180 nm CMOS with capacitively coupled pre-emphasis. Proceedings of Science [Internet]. 2018 Mar 20 [cited 2022 May 1];313:038. Available from: https://pos.sissa.it/

56. Larrea CG, Harder K, Newbold D, Sankey D, Rose A, Thea A, et al. IPbus: a flexible Ethernet-based control system for xTCA hardware. Journal of Instrumentation [Internet]. 2015 Feb 11 [cited 2022 May 13];10(02):C02019. Available from: https://iopscience.iop.org/article/10.1088/1748-0221/10/02/C02019

57. Schioppa EJ, Asensi Tortajada I, Berdalovic I, Bortoletto D, Cardella R, Dachs F, et al. Measurement results of the MALTA monolithic pixel detector,. Nucl Instrum Meth. 2019 Apr 1;958.

58. Hiti B. Radiation Hardness of CMOS detector prototypes for ATLAS Phase-II ITk upgrade [Internet] [PhD]. [Ljubljana]: Ljubljana U.; 2020 [cited 2022 May 13]. Available from: https://cds.cern.ch/record/2733027

59. Berdalovic I. Design of radiation-hard CMOS sensors for particle detection applications [Internet] [PhD]. [Zagreb]: Zagreb U.; 2019 [cited 2022 May 13]. Available from: https://cds.cern.ch/record/2702884

60. Sharma A. Characterisation of advanced silicon pixel detector prototypes for the Inner Tracker of the ATLAS experiment for the High Luminosity LHC [Internet] [PhD]. [St Cross College, Oxford]: Oxford U.; 2020 [cited 2022 May 13]. Available from: https://cds.cern.ch/record/2743291

61. Pernegger H, Bates R, Buttar C, Dalla M, Hoorne JWV, Kugathasan T, et al. First tests of a novel radiation hard CMOS sensor process for Depleted Monolithic Active Pixel Sensors. Journal of Instrumentation [Internet]. 2017 Jun 7 [cited 2022 May 13];12(06):P06008. Available from: https://iopscience.iop.org/article/10.1088/1748-0221/12/06/P06008

62. Kugathasan T, Bates R, Buttar C, Berdalovic I, Blochet B, Cardella R, et al. Monolithic Pixel Development in 180 nm CMOS for the Outer Pixel Layers in the ATLAS Experiment. Proceedings of Science. 2018 Mar 20;313:047.

63. Argemi LS, Asensi IA, Berdalovic I, Bortoletto D, Cardella R, Dachs F, et al. The Malta CMOS pixel detector prototype for the ATLAS Pixel ITK. Proceedings of Science. 2019 Sep 6;348:014.

64. al. IAT et. RADIATION HARD MONOLITHIC CMOS SENSORS WITH SMALL ELECTRODE SIZE FOR THE ATLAS EXPERIMENT IN THE HL-LHC. RAP 2019 Conference Proceedings. 2020 Jan;4.

65. Berdalovic I, Bates R, Buttar C, Cardella R, Plaja NE, Hemperek T, et al. Monolithic pixel development in TowerJazz 180 nm CMOS for the outer pixel layers in the ATLAS experiment. Journal of Instrumentation. 2018 Jan 1;13(1).

66. Wang T, Barbero M, Berdalovic I, Bespin C, Bhat S, Breugnon P, et al. Depleted fully monolithic CMOS pixel detectors using a column based readout architecture for the ATLAS Inner Tracker upgrade. Journal of Instrumentation. 2018 Mar 23;13(3).

67. Baudot J, Bertolone G, Brogna A, Claus G, Colledani C, Değerli Y, et al. First test results of MIMOSA-26, a fast CMOS sensor with integrated zero suppression and digitized output. IEEE Nuclear Science Symposium Conference Record. 2009;1169–73.

68. Kiehn M. Proteus beam telescope reconstruction. 2019 Mar 7 [cited 2022 May 13]; Available from: https://zenodo.org/record/2586736

69. Munker M, Benoit M, Dannheim D, Fenigstein A, Kugathasan T, Leitner T, et al. Simulations of CMOS pixel sensors with a small collection electrode, improved for a faster charge collection and increased radiation tolerance. Journal of Instrumentation [Internet]. 2019 May 15 [cited 2022 May 1];14(5). Available from: http://arxiv.org/abs/1903.10190

70. Dyndal M, Dao V, Allport P, Tortajada IA, Barbero M, Bhat S, et al. Mini-MALTA: Radiation hard pixel designs for small-electrode monolithic CMOS sensors for the High Luminosity LHC. Journal of Instrumentation. 2020 Feb 10;15(2).

71. Bisanz T, Jansen H, Arling JH, Bulgheroni A, Dreyling-Eschweiler J, Eichhorn T, et al. EUTelescope: A modular reconstruction framework for beam telescope data. Journal of Instrumentation [Internet]. 2020 Sep 15 [cited 2022 May 13];15(09):P09020. Available from: https://iopscience.iop.org/article/10.1088/1748-0221/15/09/P09020

72. Neria Y, Neugebauer R. Bulk Crystal Growth: Basic Techniques, and Growth Mechanisms and Dynamics. Vol. 121, Public Health. 2007. 572–575 p.

73. Perktold L, Christiansen J. A multichannel time-to-digital converter ASIC with better than 3 ps RMS time resolution. Journal of Instrumentation [Internet]. 2014 Jan 30 [cited 2022 May 13];9(01):C01060. Available from: https://iopscience.iop.org/article/10.1088/1748-0221/9/01/C01060

74. HPTDC High Performance Time to Digital Converter - CERN Document Server [Internet]. [cited 2022 May 13]. Available from: https://cds.cern.ch/record/1067476

75. Sanchez CS, Allport P, Tortajada IA, Bortoletto D, Buttar C, Cardella R, et al. Radiation hard monolithic CMOS sensors with small electrodes for the HL-LHC and beyond. Proceedings of Science. 2021 Apr 15;390:871.

76. Piro F, Allport P, Asensi I, Berdalovic I, Bortoletto D, Buttar C, et al. A 1 μW radiation-hard front-end in a 0.18 μm CMOS process for the MALTA2 monolithic sensor. IEEE Transactions on Nuclear Science [Internet]. 2022 [cited 2022 May 1];1–1. Available from: https://ieeexplore.ieee.org/document/9764367/

77. Pohl DL, Hemperek T, Caicedo I, Gonella L, Hügging F, Janssen J, et al. Radiation hard pixel sensors using high-resistive wafers in a 150 nm CMOS processing line. Journal of Instrumentation [Internet]. 2017 Feb 16 [cited 2022 May 13];12(6). Available from: http://arxiv.org/abs/1702.04953

78. Recent results with radiation-tolerant TowerJazz 180 nm MALTA Sensors. In [cited 2022 May 13]. Available from: https://indico.cern.ch/event/1044975/contributions/4663664/

79. Sadrozinski HFW, Seiden A, Cartiglia N. 4D tracking with ultra-fast silicon detectors. Reports on Progress in Physics [Internet]. 2017 Dec 18 [cited 2022 May 13];81(2):026101. Available from: https://iopscience.iop.org/article/10.1088/1361-6633/aa94d3

80. Selvaggi M. DELPHES 3: A modular framework for fast-simulation of generic collider experiments. Journal of Physics: Conference Series [Internet]. 2014 Jun 6 [cited 2022 Jun 7];523(1):012033. Available from: https://iopscience.iop.org/article/10.1088/1742-6596/523/1/012033

81. Yusuwan NM, Adnan H, Zakiyuddin Z, Rashid A, Mertens A. New features in Delphes 3. Journal of Physics: Conference Series [Internet]. 2015 Apr 1 [cited 2022 Jun 7];608(1):012045. Available from: https://iopscience.iop.org/article/10.1088/1742-6596/608/1/012045

82. de Favereau J, Delaere C, Demin P, Giammanco A, Lemaître V, Mertens A, et al. DELPHES 3: a modular framework for fast simulation of a generic collider experiment. Journal of High Energy Physics 2014 2014:2 [Internet]. 2014 Feb 13 [cited 2022 Jun 7];2014(2):1–26. Available from: https://link.springer.com/article/10.1007/JHEP02(2014)057

83. Sjöstrand T, Mrenna S, Skands P. A brief introduction to PYTHIA 8.1. Computer Physics Communications. 2008 Jun 1;178(11):852–67.

84. Alwall J, Ballestrero A, Bartalini P, Belov S, Boos E, Buckley A, et al. A standard format for Les Houches Event Files. Computer Physics Communications. 2007 Feb 15;176(4):300–4.

85. The HepMC C++ Monte Carlo Event Record for High Energy Physics - CERN Document Server [Internet]. [cited 2022 Jun 7]. Available from: http://cds.cern.ch/record/684090?ln=en

86. Cacciari M, Salam GP, Soyez G. FastJet User Manual. Eur Phys J. 2012 Mar;C 72(3):1896.

87. Brun R, Rademakers F, Canal P, Naumann A, Couet O, Moneta L, et al. root-project/root: v6.18/02. 2019 Aug 23 [cited 2022 Jun 7]; Available from: https://zenodo.org/record/3895860

88. A Delphes parameterisation of the FCC-hh detector - CERN Document Server [Internet]. [cited 2022 Jun 7]. Available from: https://cds.cern.ch/record/2717698

89. Rose K. Deterministic annealing for clustering, compression, classification, regression, and related optimization problems. Proceedings of the IEEE. 1998;86(11):2210–39.

90. Cerri O, Xie S, Pena C, Spiropulu M. Identification of long-lived charged particles using time-of-flight systems at the upgraded LHC detectors. Journal of High Energy Physics 2019 2019:4 [Internet]. 2019 Apr 4 [cited 2022 Jun 7];2019(4):1–21. Available from: https://link.springer.com/article/10.1007/JHEP04(2019)037

91. GitHub - ocerri/Delphes: Fast simulation of HEP particle detector [Internet]. [cited 2022 Jun 7]. Available from: https://github.com/ocerri/Delphes

92. Mangano ML, Ortona G, Selvaggi M. Measuring the Higgs self-coupling via Higgs-pair production at a 100 TeV p–p collider. The European Physical Journal C. 2020 Nov 8;80(11):1030.

93. Micco B di, Gouzevitch M, Mazzitelli J, Vernieri C. Higgs boson potential at colliders: Status and perspectives. Reviews in Physics. 2020 Nov 1;5:100045.

94. Alwall J, Herquet M, Maltoni F, Mattelaerc O, Stelzerd T. MadGraph 5: going beyond. Journal of High Energy Physics 2011 2011:6 [Internet]. 2011 Jun 28 [cited 2022 Jun 7];2011(6):1–40. Available from: https://link.springer.com/article/10.1007/JHEP06(2011)128

95. Cerati G, Tadel M, Wurthwein F, Yagil A, Lantz S, McDermott K, et al. Kalman-Filter-based particle tracking on parallel architectures at Hadron Colliders. 2015 IEEE Nuclear Science Symposium and Medical Imaging Conference, NSS/MIC 2015. 2016 Oct 3;

96. Cacciari M, Salam GP, Soyez G. The Anti-k(t) jet clustering algorithm. JHEP. 2008 Apr 1;04(4):063.

97. Cacciari M, Salam GP. Pileup subtraction using jet areas. Phys Lett. 2008 Jan 17;B 659(1–2):119.

98. Ai X, Allaire C, Calace N, Czirkos A, Ene I, Elsing M, et al. A Common Tracking Software Project. 2021 Jun 25 [cited 2022 May 1]; Available from: https://arxiv.org/abs/2106.13593v1

7. APPENDICES

$< -\frac{dE}{dx} >$	:	Mean rate of energy loss
m_e	:	Electron mass
ϵ_0	:	Vacuum permittivity
r_e	:	Classical electron Radius ($e^2/4\pi\epsilon_0 m_e c^2$)
N_A	:	Avogadro's number
K	:	$4\pi N_A r_e^2 m_e c^2$
c	:	Speed of light
z	:	Charge number of incident particle
Z	:	Atomic number of absorber
A	:	Atomic mass of absorber
β	:	Fraction of the speed of light v/c
γ	:	Lorentz factor $1/\sqrt{1 - \beta^2}$
W_{max}	:	Maximum energy transfer in a single collision
I^2	:	Mean excitation energy
$\delta(\beta\gamma)$	:	Density effect correction for stopping power at high energies
b_{max}	:	Maximum impact parameter
C/Z	:	Shell correction for stopping power at low energies